

¹ Study of the multi-strange resonance $\Xi(1530)^0$ production
² with ALICE at the LHC energies

³ Jihye Song

4 Contents

5	List of Figures	3
6	List of Tables	4
7	1 The physics of relativistic heavy-ion collisions	5
8	1.1 Standard model	5
9	1.2 QCD and Quark-Gluon plasma	6
10	1.3 Heavy Ion Collisions	11
11	2 Theoretical models	13
12	2.1 Thermal statistical model	13
13	2.1.1 Calculations	15
14	2.1.2 Results and comparison with data	15
15	2.2 EPOS, UrQMD	17
16	3 Production of resonance with strangeness	19
17	3.1 Strange quark and hyperons	21
18	3.2 Resonance production	23
19	4 A Large Ion Collider Experiment at the LHC	25
20	4.1 The Large Hadron Collider	25
21	4.2 The ALICE project	28
22	4.2.1 ALICE detector	28
23	4.2.2 Data Acquisition (DAQ) and trigger system	38
24	4.2.3 ALICE offline software frame work	40
25	5 Measurement of $\Xi(1530)^0$ production in p-Pb and Pb-Pb	42
26	5.1 $\Xi(1530)^0$ -reconstruction	42
27	5.1.1 Data sample and event selection	42
28	5.1.2 Track and topological selection	46
29	5.1.3 Particle identification	49
30	5.1.4 Signal extraction	52
31	5.2 Efficiency correction	60
32	5.3 Corrected p_T -spectra	63
33	5.4 Systematic uncertainties	65
34	5.5 $\Xi(1530)^0$ transverse momentum spectra	70
35	6 Further results and discussion	73
36	6.1 Mean transverse momentum	73
37	6.2 Particle yield ratios	77

38	6.2.1 Integrated yield ratios of excited to ground-state hadrons	77
39	6.3 Integrated yield ratios to pion	80
40	References	84

41 **List of Figures**

42 1	Standard Model families of leptons and quarks as the gauge bosons	5
43 2	Summary of measurements of γ s as a function of the respective energy scale Q. The respective degree of QCD perturbation theory used in the extraction of γ s is indicated in brackets (NLO: next-to-leading order; NNLO: next-to-next-to leading order; res. NNLO: NNLO matched with resummed next-to-leading logs; N3LO: next-to-NNLO) [1]	9
44 3	Hydrodynamic evolution of a heavy ion collision with and without the for- 45 mation of a QGP.	12
46 4	Grand canonical thermal fit of 0-10% central Pb-Pb collisions, with 3 models (THERMUS, GSI, SHARE). Excluded volume correction implemented in 47 THERMUS and GSI with $rh = 0.3$ fm μ_B fixed to 0, γ_s fixed to 1, γ_c fixed 48 to 20 (THERMUS and GSI)	13
49 5	Ratio of baryonic and mesonic resonances over their stable partner as a 50 function of temperature.	16
51 6	Ratio of resonances over their stable partner as a function of $\sqrt(s)$	17
52 7	The $J^P = 1/2^+$ ground state baryon octet	20
53 8	The $J^P = 3/2^+$ baryon decuplet	20
54 9	Enhancements in the rapidity range $ y < 0.5$ as a function of the mean 55 number of participants $\langle N_{part} \rangle$, showing LHC (ALICE, full symbols), RHIC 56 and SPS (open symbols) data. Boxes on the dashed line at unity indicate 57 statistical and systematic uncertainties on the pp or p-Be reference. Error 58 bars on the data points represent the corresponding uncertainties for all the 59 heavy-ion measurements and those for p-Pb at the SPS.	22
60 10	Hadronic phase	23
61 11	The CERN accelerator complex [2]	26
62 12	The ALICE detector	30
63 13	Schematic view of the ITS [3]	31
64 14	Track impact parameter resolution in the transverse plane ($r\phi$) vs p_T for 65 charged particle	32
66 15	Schematic view of the TPC	33
67 16	Specific energy loss (dE/dx) in the TPC vs. particle momentum in Pb-Pb 68 collisions at $\sqrt{s_{NN}} = 2.76$ TeV. The lines show the parametrisations of the 69 expected mean energy loss.	34
70 17	Correlation between the sum and difference of signal times in V0A and V0C. 71 Three classes of events collisions at (8.3 ns, 14.3 ns), background from Beam 72 1 at (-14.3 ns, -8.3 ns), and background from Beam 2 at (14.3 ns, 8.3 ns) 73 can be clearly distinguished.	36
74 18	Distribution of the V0 amplitude (sum of V0A and V0C in top, V0A in 75 bottom). The inset shows a magnified version of the most peripheral region.	37

81	19	The overall architecture of the ALICE DAQ and the interface to the HLT system.	38
82	20	Schematic view of the AliRoot framework	41
83	21	Vertex-z coordinate distribution of the accepted events in p–Pb collision(Left) and in Pb–Pb collisions(Right). The red dashed line indicates vertex cut	44
84	22	Multiplicity distribution of accepted events in p–Pb collision in percentile. The each color and labels define the four intervals in which the analysis is performed.	44
85	23	Centrality distribution of three different trigger classes.	45
86	24	Sketch of the decay modes for Ξ^{*0} and depiction of the track and topological selection criteria.	47
87	25	TPC dE/dx as function of transverse momentum for total (top) and selected first emitted π in 3σ (bottom)	49
88	26	TPC dE/dx as function of transverse momentum for total (top) and selected second emitted π in 3σ (bottom)	49
89	27	TPC dE/dx as function of transverse momentum for total (top) and selected last emitted π in 3σ (bottom)	50
90	28	TPC dE/dx as function of transverse momentum for total (top) and selected proton in 3σ (bottom)	50
91	29	TPC dE/dx as function of transverse momentum for total (top) and selected first emitted π in 3σ (bottom)	50
92	30	TPC dE/dx as function of transverse momentum for total (top) and selected second emitted π in 3σ (bottom)	51
93	31	TPC dE/dx as function of transverse momentum for total (top) and selected last emitted π in 3σ (bottom)	51
94	32	TPC dE/dx as function of transverse momentum for total (top) and selected proton in 3σ (bottom)	52
95	33	The $\Xi^\mp\pi^\pm$ invariant mass distribution (Same-event pairs) in $1.8 < p_T < 2.2$ GeV/ c and for the multiplicity class 20-40%. The background shape, using pairs from different events (Mixed-event background), is normalised to the counts in $1.49 < M_{\Xi\pi} < 1.51$ GeV/ c^2 and $1.56 < M_{\Xi\pi} < 1.58$ GeV/ c^2	53
96	34	The $\Xi^\mp\pi^\pm$ invariant mass distribution (Same-event pairs) in $3.0 < p_T < 3.5$ GeV/ c and for the centrality class 0-10%. The background shape, using pairs from different events (Mixed-event background), is normalised to the counts in $1.49 < M_{\Xi\pi} < 1.51$ GeV/ c^2 and $1.56 < M_{\Xi\pi} < 1.58$ GeV/ c^2	54
97	35	The invariant mass distribution after subtraction of the mixed-event background in p–Pb collisions. The solid curve represents the combined fit, while the dashed line describes the residual background.	55
98	36	The invariant mass distribution after subtraction of the mixed-event background in Pb–Pb collisions. The solid curve represents the combined fit, while the dashed line describes the residual background.	56

122	37	σ fit parameters as a function of p_{T} in MB in p–Pb collisions (top) and in Pb–Pb collisions (bottom).	57
123	38	$\Xi(1530)^0$ -mass obtained from fit of the Voigtian peak as a function of p_{T} in each multiplicity classes in p–Pb collisions (top) and the different centrality classes in Pb–Pb (bottom).	58
124	39	$\Xi(1530)^0$ -raw spectra obtained from fit of the Voigtian peak and a polynomial residual background for different multiplicities in p–Pb collisions (top) and Pb–Pb collisions (bottom). Only the statistical error is reported.	59
125	40	$\Xi(1530)^0$ -raw spectra obtained from fit of the Voigtian peak and a polynomial residual background for different multiplicities. Only the statistical error is reported.	60
126	41	Real corrected $\Xi(1530)^0$ spectrum (black) for the minimum bias with Levy fit (black curve). Also shown are the unweighted generated (blue) and reconstructed (red) $\Xi(1530)^0$ spectra.	61
127	42	Efficiency as a function of p_{T} in minimum bias events in p–Pb collisions.	62
128	43	Efficiency as a function of p_{T} in different centrality classes in Pb–Pb collisions	63
129	44	Corrected p_{T} -spectra of $\Xi(1530)^0$ in NSD and different multiplicity classes in p–Pb collisions.	64
130	45	Corrected p_{T} -spectra of $\Xi(1530)^0$ in different centrality classes in Pb–Pb collisions.	64
131	46	Summary of the contributions to the systematic uncertainty in minimum bias events in p–Pb collisions. The dashed black line is the sum in quadrature of all the contributions.	68
132	47	Systematic uncertainties for each multiplicity classes in p–Pb collisions.	68
133	48	Summary of the contributions to the systematic uncertainty in minimum bias events in Pb–Pb collisions. The dashed black line is the sum in quadrature of all the contributions.	69
134	49	Systematic uncertainties for each multiplicity classes.	69
135	50	Corrected yields as function of p_{T} in NSD events and multiplicity dependent event classes in p–Pb collision system. Statistical uncertainties are presented as bar and systematical uncertainties are plotted as boxes.	71
136	51	Corrected yields as function of p_{T} in different centrality classes in Pb–Pb collision system. Statistical uncertainties are presented as bar and systematical uncertainties are plotted as boxes.	72
137	52	Mean transverse momenta $\langle p_{\text{T}} \rangle$ of Λ , Ξ^- , $\Sigma^{*\pm}$, Ξ^{*0} and Ω^- in p–Pb collisions at $\sqrt{s_{\text{NN}}} = 5.02$ TeV as a function of mean charged-particle multiplicity density $\langle dN_{\text{ch}}/d\eta_{\text{lab}} \rangle$, measured in the pseudorapidity range $ \eta_{\text{lab}} < 0.5$. The results for Λ , Ξ^- and Ω^- are taken from [4, 5, 6]. Statistical and systematic uncertainties are represented as bars and boxes, respectively. The Ω^- and Ξ^- points in the 3rd and 4th lowest multiplicity bins are slightly displaced along the abscissa to avoid superposition with the $\Xi(1530)^0$ points.	74

163	53	Mass dependence of the mean transverse momenta of identified particles for the 0 – 20% V0A multiplicity class and with $-0.5 < y_{\text{CMS}} < 0$ in p–Pb collisions at $\sqrt{s_{\text{NN}}} = 5.02$ TeV [4, 6], and in minimum-bias pp collisions at $\sqrt{s} = 7$ TeV [7] with $ y_{\text{CMS}} < 0.5$. Additionally, D^0 and J/ψ results are plotted. The D^0 and J/ψ were measured in different rapidity ranges: $ y_{\text{CMS}} < 0.5$ [8] ($ y_{\text{CMS}} < 0.9$ [9]) for D^0 (J/ψ) in pp and $-0.96 < y_{\text{CMS}} < 0.04$ [8] ($-1.37 < y_{\text{CMS}} < 0.43$ [10]) for D^0 (J/ψ) in p–Pb. Note also that the results for D^0 and J/ψ in p–Pb collisions are for the 0–100% multiplicity class.	75
172	54	Ratio of $\Xi(1530)^0$ to Ξ^- measured in pp [7], p–Pb [4, 6] and Pb–Pb collisions as a function of $\langle dN_{\text{ch}}/d\eta_{\text{lab}} \rangle$ measured at midrapidity. Statistical uncertainties (bars) are shown as well as total systematic uncertainties (hollow boxes) and systematic uncertainties uncorrelated across multiplicity (shaded boxes). A few model predictions are also shown as lines at their appropriate abscissa.	78
178	55	Ratio of $\rho/\pi(\text{Up})$, K^*/K , $\phi/K(\text{Left bottom})$ and Λ^*/Λ with system size measured at mid-rapidity. Statistical uncertainties (bars) are shown as well as total systematic uncertainties (hollow boxes) and systematic uncertainties uncorrelated across multiplicity (shaded boxes). A few model predictions are also shown as lines at their appropriate abscissa.	79
183	56	Ratio of $\Xi(1530)^0$ to π^\pm , measured in pp [11] and p–Pb [7] collisions, as a function of the average charged particle density ($\langle dN_{\text{ch}}/d\eta_{\text{lab}} \rangle$) measured at mid-rapidity. Statistical uncertainties (bars) are shown as well as total systematic uncertainties (hollow boxes) and systematic uncertainties uncorrelated across multiplicity (shaded boxes). A few model predictions are also shown as lines at their appropriate abscissa.	81
189	57	Particle yield ratios to pions of strange and multi-strange hadrons normalized to the values measured in pp collisions, both in pp and in p–Pb collisions. The common systematic uncertainties cancel in the double-ratio. The empty boxes represent the remaining uncorrelated uncertainties. The lines represent a simultaneous fit of the results with the empirical scaling formula in Equation ???.	82
195	58	p_{T} -integrated yield ratios of strange and multi-strange hadrons to $(\pi^+ + \pi^-)$ as a function of $\langle dN_{\text{ch}}/d\eta_{\text{lab}} \rangle$ measured in the rapidity interval $ \eta < 0.5$. The empty and dark-shaded boxes show the total systematic uncertainty and the contribution uncorrelated across multiplicity bins, respectively. The values are compared to calculations from MC models and to results obtained in Pb–Pb and p–Pb collisions at the LHC.	83

201 **List of Tables**

202	1	Parameters used in the thermal-model calculations.	14
203	2	Properties of particles used in the ratio calculations.	15
204	3	Difference of mass (ΔM), baryon number (ΔB), strangeness (ΔS) and charge (ΔQ) of the ratios. The values of the slopes needs to be checked!!!! .	17
205	4	Quantum numbers and masses associated to the three lighter quarks: u, d and s	19
206	5	Lifetime of hadronic resonances	21
207	6	Number of accepted and analyzed events per multiplicity/centrality interval	46
208	7	Track selections common to all decay daughters and primary track selections applied to the charged pions from decays of Ξ^{*0}	46
209	8	Topological and track selection criteria.	47
210	9	Summary of the systematic uncertainties on the differential yield, $d^2N/(dp_T dy)$. Minimum and maximum values in all p_T intervals and multiplicity classes in p–Pb, centrality classes in Pb–Pb are shown for each source.	70
211			
212			
213			
214			
215			

216 1 The physics of relativistic heavy-ion collisions

217 1.1 Standard model

218 . Our current understanding concerning the question what the world is made of is collected
 219 in the Standard Model of particle physics (SM) [12], that describes our universe in terms of
 220 matter and forces. In this picture matter is composed of 12 point-like particles, which have a
 221 spin of 1/2 (fermions) and can be classified according to how they interact or equivalently to
 222 what charges they carry. There are six quarks (up, down, charm, strange, top and bottom)
 223 and six leptons (electron, electron neutrino, muon, muon neutrino, tau, tau neutrino) as
 224 reported in Figure `reffi:sm`. The interactions between elementary particles are described
 225 by the exchange of gauge bosons (usually as virtual particles¹) or equivalently by mean of
 226 a field. Mathematically, the SM is a quantized Yang-Mills theory based on the non-abelian
 227 symmetry group $U(1) \rightarrow SU(2) \rightarrow SU(3)$ and has a total of twelve gauge bosons: the photon,
 228 three weak bosons and eight gluons. The interactions included in such a model are the
 229 electromagnetic force, the weak force and the strong one. Quarks have a property called
 230 color, playing the role of charge in the strong force. Both quarks and leptons are affected
 231 by the weak force and all the charged particles interact electromagnetically. The models
 232 that describe these interactions are listed as follows:

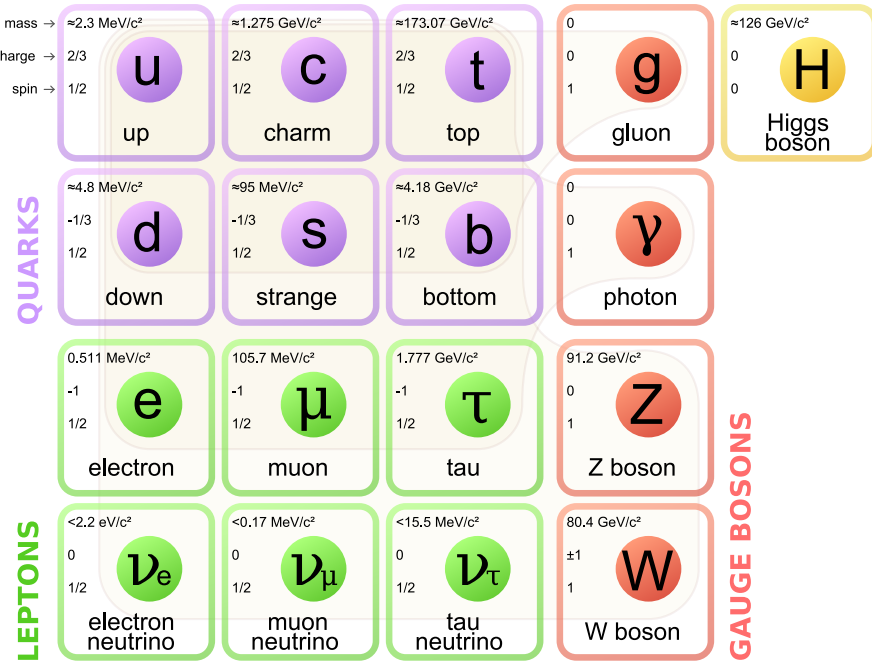


Figure 1: Standard Model families of leptons and quarks as the gauge bosons

233 **Quantum Electro-Dynamics (QED)** describes how light and matter interact. This
234 is the first theory where full agreement between quantum mechanics and special relativity
235 is achieved. It was developed between 1946 and 1950 by Tomonaga Shinichiro, Julian S.
236 Swinger and Richard P. Feynmann. They were awarded the Nobel prize in 1965.

237
238 **Electroweak Theory (EW)** is the unified description of two of the four known funda-
239 mental interactions of nature: electromagnetism and the weak interaction. It first appeared
240 in 1961, driven by Sheldon Lee Glashow, and was completed in 1967 by Abdus Salam and
241 Steven Weinberg. They were awarded the Nobel prize in 1979. The first measurement
242 of the existence of the weak bosons W^+ , W^- and Z^0 was performed in 1983, when they
243 were produced and directly observed in $S\bar{p}\bar{p}S$ collisions at CERN. During the next year the
244 Nobel prize for this experimental result was assigned to Carlo Rubbia and Simon van der
245 Meer. In 1999 Gerardus 't Hooft and Martinus Veltman were awarded the Nobel prize for
246 showing that the electroweak theory is renormalisable.

247
248 **Quantum Chromo-dynamics (QCD)** is the theory of the strong interaction (color
249 force), describing the interactions between quarks and gluons which make up the hadrons.
250 Starting from the classification of the large amount of particles discovered during the fifties,
251 the original idea of the quark model by Gell-Mann (Nobel Prize in 1969) has been developed
252 during the sixties until 1973, when David J. Gross, H. David Politzer and Frank Wilczek
253 discovered the 'asymptotic freedom' property of the strong nuclear interaction (Nobel
254 Prize in 2004).

255 1.2 QCD and Quark-Gluon plasma

256 When, starting in 1950s, the number of known particle species became large, the idea
257 that these could be the elementary constituents of matter was replaced by the notion
258 that these species could in fact be composite objects made up of fewer, more elementary
259 particles, in a similar way to what had already happened to the elements of Mendeleev's
260 Periodic Table. The original idea by Gell-Mann (1964) was that the hadrons could be
261 obtained as combination of the fundamental representation of an $SU_f(3)$ group, where
262 three different flavors of quark ($q = u, d, s$) combine to build mesons ($q\bar{q}$) and hadrons
263 (qqq). However, when cataloging hadrons using the $SU_f(3)$ group, there are anomalous
264 states, such as the $\Omega^-(sss)$ and the $\Delta^{++}(uuu)$, that are combinations of three quarks of
265 the same flavor, in clear contrast with the Pauli exclusion principle for fermions. A solution
266 was proposed in 1965 by Moo-Young Han with Yoichiro Nambu and Oscar W. Greenberg,
267 who independently solved the problem by proposing that quarks possess an additional
268 $SU(3)$ gauge quantum number, later called color charge. This new quantum number may
269 assume three states, represented by the three primary colors: red, green and blue (denoted
270 symbolically by R, G and B, respectively). The introduction of this new quantum number
271 also provides an explanation to other empirical evidence, such as the fact that no qq , $\bar{q}q$

272 or the single quark have never been observed directly. On the other hand, the existence of
 273 color charge gives rise to the possible existence of differently colored states for each particle;
 274 thus, we could have many states for the proton, such as $u_R u_G d_B$, $u_R u_G d_G$, $u_B u_R d_R$, and
 275 so on. The fundamental rule that solves such contradictions is that all the particle states
 276 observed in nature are "colorless" or "white" (or, to be more precise, unchanged under
 277 $SU_c(3)$ rotations). The dynamics of the quarks and gluons are controlled by the gauge
 278 invariant QCD Lagrangian:

$$\mathcal{L}_{QCD} = \underbrace{i\delta_{ij}\bar{\Psi}_q^i\gamma^\mu\partial_\mu\Psi_q^j}_{\mathcal{L}_1} + \underbrace{g_s\bar{\Psi}_q^i\gamma^\mu t_{ij}^a A_\mu^a\Psi_q^j}_{\mathcal{L}_2} + \underbrace{m_q\bar{\Psi}_q^i\Psi_q^j}_{\mathcal{L}_3} + \underbrace{\frac{1}{4}F_{\mu\nu}^a F^{a\mu\nu}}_{\mathcal{L}_4} \quad (1)$$

279 where the coloured gluon field tensor, $F_{\mu\nu}^a$ (with color index a) and the squared gauge
 280 coupling parameter, g_s^2 (associated to the strong coupling constant α_s) are defined as:

$$F_{\mu\nu}^a = \partial_{mu}A_\nu^a - \partial_\nu A_\mu^a + g_s f^{abc} A_\mu^b A_\nu^c \quad (2)$$

281 and

$$g_s^2 = 4\pi\alpha_s \quad (3)$$

282 where:

- 283 • Ψ_q^i : the quark field with flavor q and color index $i \in [1;3]$, such as $\Psi_q = (\Psi_{qR}, \Psi_{qG},$
 284 $\Psi_{qB})^T$ and A_μ^a is the gluon field with color index a (adjoint representation)
- 285 • γ^μ : Dirac matrices that express the vector nature of the strong interaction, with μ
 286 being the Lorentz vector associated index
- 287 • m_q : quark mass, a priori not equal to zero (resulting from the Higgs mechanism or
 288 equivalent)
- 289 • t_{ij}^a : generator matrices of the group $SU_c(3)$, proportional to the Gell-Mann matrices,
 290 that perform revolutions in color space, representing interaction of quarks and gluons
- 291 • f^{abc} : structure constant of QCD

292 Each of the four terms of the QCD Lagrangian expresses and aspect of the interaction,
 293 specifically:

- 294 • \mathcal{L}_1 : gives the kinetic energy of the quark field Ψ_q^i
- 295 • \mathcal{L}_2 : gives the interaction between quarks (fermions) and gluons (the bosons of the
 296 interaction)
- 297 • \mathcal{L}_3 : gives the mass of the quarks

- 298 • \mathcal{L}_4 : gives the kinetic energy of the gluons

299 The terms of this equation, together with the fundamental parameters α_s and m_q ,
300 summarize in just one expression all the features of the strong interaction. The first three
301 terms describe the free propagation of quarks and gluons and the quark-gluon interaction.
302 The remaining two terms show the presence of three and four gluon vertices in QCD and
303 reflect the fact that gluons themselves carry color charge. This is a consequence of the non-
304 abelian4 character of the gauge group. This peculiarity of the QCD interaction imposes the
305 evolution of the strong coupling constant, α_s . The corresponding trend has been measured
306 experimentally, and compared in Figure 2 with predictions. A practical consequence of
307 this behavior is that the corresponding potential has a completely different shape than the
308 other fundamental interactions and can be expressed by the following equation:

$$V(r) = -4 \frac{\alpha_s}{3r} + kr \quad (4)$$

309 where r is the separation distance between the two quarks and k is a constant that is
310 approximately 1 GeV/fm.

311 Three are main properties of the QCD interaction:

312 **Confinement** At large distances between quarks and gluons (i.e. small values of trans-
313 ferred momentum Q in Figure 2) the coupling constant is large and the associated force
314 is strong enough to keep these elementary con- stituents (usually called partons) confined
315 in bounded states. As expressed in the Equation 4, the attractive potential increases with
316 the increasing of the relative distance between the two partons preventing the separation
317 of an individual quark or gluon. This explains the meaning of the term "confinement"
318 adopted to describe this energy regime. From the theoretical point of view, the large value
319 of α_s make impossible any perturbative approach in the solution of the Hamilton equation
320 of the system. A successful solution is to perform the study of the system on a discrete
321 space. Such techniques are known as lattice QCD and are based on numerical Monte Carlo
322 simulations. The challenge for the calculations is to reduce the lattice spacing in order to
323 approach the continuum.

325 **Asymptotic freedom** Reducing the distance between quarks and gluons (i.e. increas-
326 ing Q in Figure 2) the coupling constant α_s becomes smaller. As anticipated, this is a
327 unique feature among the forces and comes from the non-abelian nature of the QCD gauge
328 symmetry. Such a phenomenon is also depicted by the weakening of the anti-screening
329 effect of the surround- ing virtual gluons with decreasing distance. In this way two quarks
330 closer and closer in space show each other a smaller and smaller color charge. **Chiral**
331 **symmetry** One further property of interest is connected to the chirality of the quark. It
332 can be verified that the QCD lagrangian for massless quarks is invariant under a chiral
333 rotation $(SU_L(N_f) \times SU_R(N_f))$, while the operator $\bar{q}q = \bar{q}_L q_R + \bar{q}_R q_L$ is not invariant (in

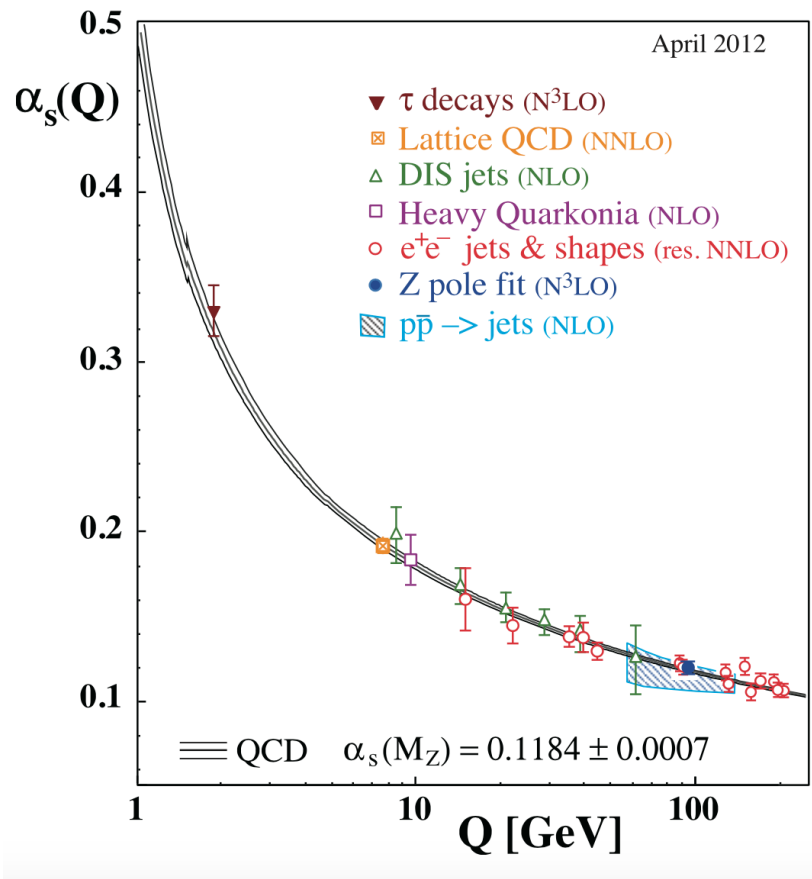


Figure 2: Summary of measurements of α_s as a function of the respective energy scale Q . The respective degree of QCD perturbation theory used in the extraction of α_s is indicated in brackets (NLO: next-to-leading order; NNLO: next-to-next-to leading order; res. NNLO: NNLO matched with resummed next-to-leading logs; N3LO: next-to-NNLO) [1]

335 the axial part), meaning that the mesons (state $\bar{q}q$) should have the same mass. Experi-
336 mentally this is clearly not true, and it could be shown that the axial current is conserved
337 (PCAC and the Goldberger-Treiman relation). The solution to this puzzle is that the chi-
338 ral (axial-vector) symmetry is spontaneously broken; this means that the symmetry of the
339 Hamiltonian is not a symmetry of the corresponding ground state. It has also been shown,
340 by G. 'tHooft, that the confinement implies a dynamical breaking of the chiral symmetry
341 [7]; this means that the breaking comes from the interaction between the objects in the
342 system. From this follows that the masses of the quarks are strongly increased because of
343 the interaction with the constituents of the system. This mechanism, known as dynamical
344 chiral symmetry breaking justifies the mass of the hadrons, reducing the role of the Higgs
345 mechanism in the mass explanation at least for the light hadrons.

346 **1.3 Heavy Ion Collisions**

347 In the case a QGP is formed, it will eventually expand because of its internal pressure.
348 As the system expands it also cools. The space-time evolution of the expansion can be
349 seen in Figure 3 (right side). A and B represent the two incoming ion beams. After a pre-
350 equilibrium phase a QGP is formed. As it expands, the system will eventually reach what
351 is known as the critical temperature (T_c). At this point partons begin to hadronize and this
352 will continue until the chemical freeze-out (T_{ch}) takes place, when inelastic collisions cease.
353 At this stage the distribution of hadrons is frozen. As cooling and expansion continue the
354 hadrons reach what is called thermal freeze out (T_{fo}). Here the elastic collisions stop and
355 the hadrons carry fixed momenta. The QGP state can not be directly observed, because of
356 its short lifetime. Instead, through experiment we measure the final state hadrons, which
357 have a fixed momentum after T_{fo} . The observables of interest should tell us about the
358 de-confinement and the thermodynamic properties of the matter. Moreover, experimental
359 measurements include yields and p_T spectra of various particle species, azimuthal studies
360 of high p_T particles, phase space distributions, and particle correlations.

361 A practical way to reach a critical condition in which a nuclear system should undergo
362 a phase transition to the QGP, at high temperature and/or matter density, is to collide
363 two nuclei at sufficiently high energy. Therefore, relativistic and ultra-relativistic heavy-ion
364 collisions are a unique tool to study nuclear matter under extreme conditions.

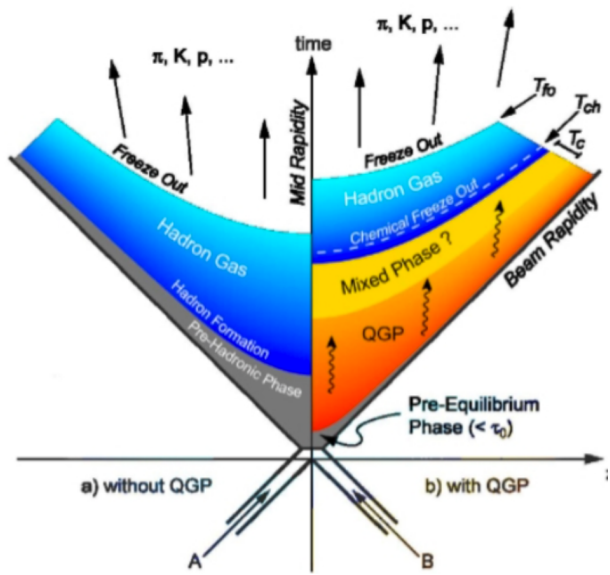


Figure 3: Hydrodynamic evolution of a heavy ion collision with and without the formation of a QGP.

365 **2 Theoretical models**

366 **2.1 Thermal statistical model**

367 The statistical-thermal model has proved extremely successful in applications to relativistic
 368 collisions of both heavy ions and elementary particles. In light of this success, THERMUS,
 369 a thermal model analysis package, has been developed for incorporation into the object-
 370 oriented ROOT framework [13].

371

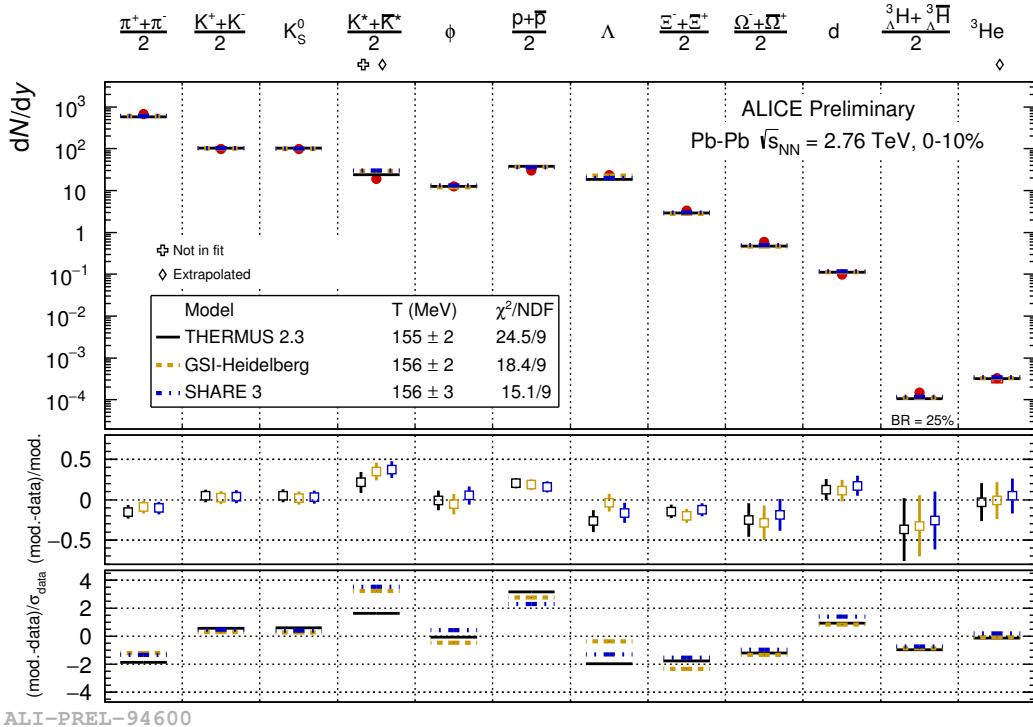


Figure 4: Grand canonical thermal fit of 0-10% central Pb-Pb collisions, with 3 models (THERMUS, GSI, SHARE). Excluded volume correction implemented in THERMUS and GSI with $rh = 0.3$ fm μ_B fixed to 0, γ_s fixed to 1, γ_c fixed to 20 (THERMUS and GSI)

372 There are three types of statistical-thermal models in explaining data in high energy
 373 nuclear physics and THERMUS treats the system quantum numbers B (baryon number),
 374 S (strangeness) and Q (charge) within three distinct formalisms:

375 **1. Grand-Canonical Ensemble:** Because the hot dense matter produced in nucleus-
 376 nucleus collisions is large enough, this ensemble is the most widely used in applications

377 to heavy-ion collisions, in which the quantum numbers are conserved on average.

- 378 2. **Fully-Canonical Ensemble:** In which B, S and Q are each exactly conserved and
379 this ensemble used in high-energy elementary collisions such as pp, p \bar{p} and e $^-$ e $^+$
380 collisions.
- 381 3. **Strangeness-Canonical Ensemble:** In small systems or at low temperatures, a
382 canonical treatment leads to a suppression of hadrons carrying non-zero quantum
383 numbers, since these particles have to be created in pairs and the resulting low
384 production of strange particles requires a canonical treatment of strangeness.

385 In order to calculate the thermal properties of a system, one starts with an evaluation
386 of its partition function. The form of the partition function obviously depends on the
387 choice of ensemble. In the present analysis the strangeness-canonical ensemble used and
388 the statistical-thermal model requires six parameters as input: the chemical freeze-out
389 temperature T , baryon and charge chemical potentials μ_B and μ_Q respectively, canonical
390 or correlation radius, R_C ; the radius inside which strangeness is exactly conserved and the
391 fireball radius R . An additional strangeness saturation factor γ_S has been used as indicator
392 of a possible departure from equilibrium and $\gamma_S = 1.0$ corresponds to complete strangeness
393 equilibration.

394 The volume dependence cancels out when studying the particle ratios as well as strangeness
395 canonical equivalent to grand canonical formalism if $\Delta S = 0$ in the ratios and γ_S also can-
396 cels out. Parameters used in the analysis listed in Table 1. The μ_B parameter taken from
397 the Ref. [14].

Table 1: Parameters used in the thermal-model calculations.

Parameter	Value
T (MeV)	varied (see text)
μ_B (MeV)	9.2×10^{-2} ????
μ_Q (MeV)	0.0
γ_S	1.0

398

399 **2.1.1 Calculations**

400 *Concept:*

401 In order to calculate the particle ratios within strangeness canonical formalism of THER-
 402 MUS, temperature varied between 60 MeV to 180 MeV and particle yields extracted for
 403 each temperature value and then primary particle ratios calculated for each case.

404

405 *Feed-Down Correction:*

406 Since the particle yields measured by the detectors in collision experiments include feed-
 407 down from heavier hadrons and hadronic resonances, the primordial hadrons are allowed to
 408 decay to particles considered stable by the experiment before model predictions are com-
 409 compared with experimental data. In the analysis only Λ particles counted as stable (do not
 410 allowed to decay) so there is no feed-down contribution from these particles to the other
 411 ratios.

412

413

414 Properties of studied particles and their particle ratios listed in Table 2 and Table 3,
 415 respectively.

Table 2: Properties of particles used in the ratio calculations.

Particle	Δ^{++}	p	K^{*0}	K^0	K^+	Λ^*	Λ	Σ^{*+}	Σ^+	Σ^0
Mass (MeV/c^2)	1232	938.27	895.92	497.61	493.67	1519.5	1115.68	1382.8	1189.37	1192.6
Width (MeV/c^2)	120	–	50.7	–	–	15.6	–	37.6	–	–
$c\tau$ (fm)	1.6	–	3.9	–	–	12.6	–	5.51	–	–
Ang. Momentum (J)	3/2	1/2	1	1	0	3/2	1/2	3/2	1/2	1/2
Isospin (I)	3/2	1/2	1/2	1/2	1/2	0	0	1	1	1
Parity (P)	+1	+1	-1	-1	0	-1	+1	+1	+1	+1
Strangeness (S)	0	0	1	1	1	-1	-1	-1	-1	-1
Baryon Number (B)	1	1	0	0	0	1	1	1	1	1
Decay Channel	$p\pi^+$	–	π^-	–	$\mu^+\nu_\mu$	pK^-	$p\pi^-$	$\Lambda\pi^+$	$p\pi^0$	$\Lambda\gamma$
Branching Ratio (%)	~ 100	–	~ 66.7	–	~ 63.54	~ 45	~ 63.9	~ 87	~ 51.6	~ 100
Q-Value(MeV/c^2)	154.16	–	262.68	–	–	87.55	37.84	127.55	111.53	76.96

416

417

418 **2.1.2 Results and comparison with data**

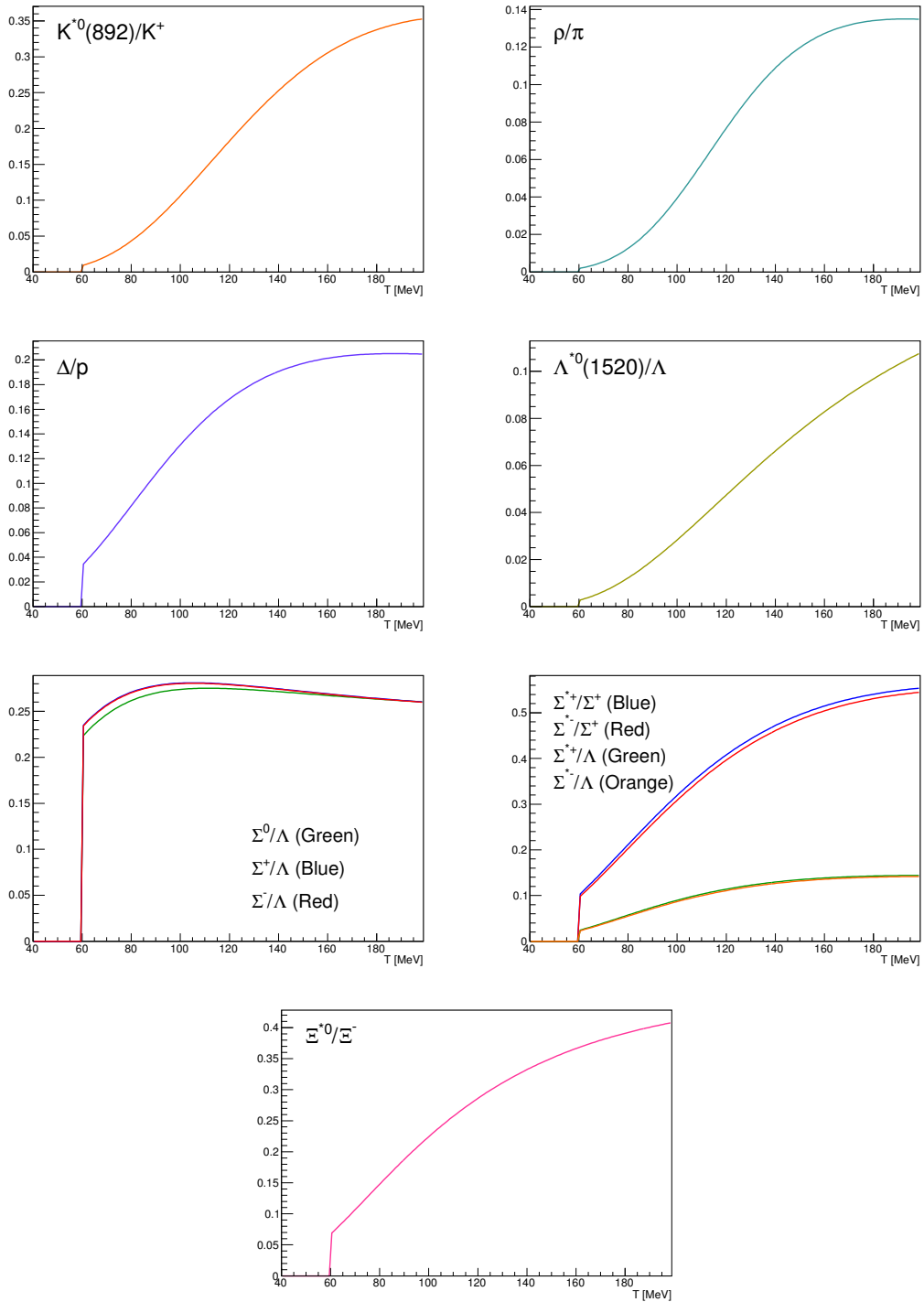


Figure 5: Ratio of baryonic and mesonic resonances over their stable partner as a function of temperature.

Table 3: Difference of mass (ΔM), baryon number (ΔB), strangeness (ΔS) and charge (ΔQ) of the ratios. The values of the slopes needs to be checked!!!!

Particle	Δ^{++}/p	K^*/K^+	Λ^*/Λ	Σ^{*+}/Λ	Σ^{*+}/Σ^0	Σ^0/Λ	Σ^{*+}/Σ^+	Ξ^{*0}/Ξ^-
ΔM (MeV/ c^2)	293.8	402.25	403.82	267.12	190.16	76.96	193.43	210.49
ΔB	0	0	0	0	0	0	0	0
ΔS	0	0	0	0	0	0	0	0
ΔQ	+1	-1	0	+1	0	+1	0	-1
Slope (%) per MeV ????????	0.19	0.76	0.98	0.25	-	-0.08	0.37	0.42

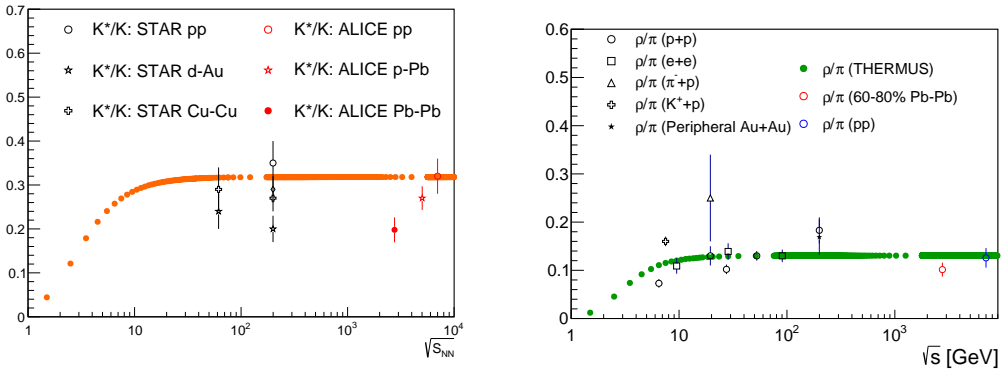


Figure 6: Ratio of resonances over their stable partner as a function of $\sqrt(s)$.

419 2.2 EPOS, UrQMD

420 The EPOS3 model [15, 16, 17] describes the full evolution of a heavy-ion collision. The
421 initial stage is treated via a multiple-scattering approach based on Pomerons and strings.
422 The reaction volume is divided into a core and a corona part [18]. The core is taken as
423 the initial condition for the QGP evolution, for which one employ viscous hydrodynamics.
424 The corona part is simply composed of hadrons from string decays. After hadronisation of
425 the fluid (core part), these hadrons and as well the corona hadrons are fed into UrQMD
426 [19, 20], which describes hadronic interactions in a microscopic approach. The chemical
427 and kinetic freeze-outs occur within this phase. The chemical freeze-out is expected to
428 occur shortly after the phase transition from partonic to hadronic matter and is followed
429 by the kinetic freeze-out.

430 As explained in [15, 16, 17, 18], EPOS3 is an event generator based on 3+1D viscous
431 hydrodynamical evolution starting from flux tube initial conditions, which are generated
432 in the Gribov-Regge multiple scattering framework. An individual scattering is referred

433 to as a Pomeron, identified with a parton ladder, eventually showing up as flux tubes (or
434 strings). Each parton ladder is composed of a pQCD hard process, plus initial and final
435 state linear parton emission. Nonlinear effects are considered by using saturation scales
436 Q_s , depending on the energy and the number of participants connected to the Pomeron in
437 question.

438 The final state partonic system (corresponding to a Pomeron) amounts to (usually two)
439 color flux tubes, being mainly longitudinal, with transversely moving pieces carrying the
440 p_T of the partons from hard scatterings. One has two flux tubes based on the cylindrical
441 topology of the Pomerons. Each quark- antiquark pair in the parton ladder will cut a string
442 into two; in this sense one may have more than two flux tubes. In any case, these flux
443 tubes eventually constitute both bulk matter, also referred to as ?core? (which thermalizes,
444 flows, and finally hadronizes) and jets (also referred to as ?corona?), according to some
445 criteria based on the energy of the string segments and the local string density. For the
446 core, we use a 3+1D viscous hydrodynamic approach, employing a realistic equation of
447 state, compatible with lQCD results. We employ for all calculations in this paper a value
448 of $\eta/s = 0.08$. Whenever a hadronisation temperature of T_H is reached, we apply the
449 usual Cooper-Frye freeze-out procedure, to convert the fluid into particles. We use $T_H =$
450 166MeV . From this point on, we apply the hadronic cascade UrQMD [19, 20], about which
451 more details are given later. All hadrons participate in the cascade, including those from
452 the core (after freeze- out) and the corona. The corona particles, from string decay, are only
453 ?visible? after a certain formation time (some constant of order one fm/c), multiplied by
454 the corresponding gamma factor), so very high p_T particles have a good chance to escape.

455 The UrQMD model is a non-equilibrium transport approach. The interactions of
456 hadrons in the current version include binary elastic and $2 \rightarrow n$ inelastic scatterings, res-
457 onance creations and decays, string excitations, particle + antiparticle annihilations as
458 well as strangeness exchange reactions. The cross sections and branching ratios for the
459 corresponding interactions are taken from experimental measurements (where available),
460 detailed balance relations and the additive quark model. The model describes the full
461 phase-space evolution of all hadrons, including resonances, in a heavy- ion collision based
462 on their hadronic interactions and their decay products. Due to the short lifetime of res-
463 onances, their decay products may interact in the hadronic phase. This is not the case
464 for weak decays, where the system has already decoupled at the time of the decay. As
465 discussed previously, the experimental reconstruction of resonances will be influenced by
466 the final state interactions of the decay products. Resonance signals have been previously
467 studied using the UrQMD model.

468 3 Production of resonance with strangeness

469 The Quark Model, proposed independently by Murray Gell-Mann and Yuval Ne?eman in
 470 1964 [21], enables the classification of hadrons in terms of their constituent quarks. In
 471 this model, the lighter mesons and baryons are representations of an $SU_f(3)$ group, whose
 472 fundamental representation is the three dimensional vector (u, d, s). These are the three
 473 lighter quarks whose characteristics are reported in Table reftable:quark.

Light flavor	d	u	s
Baryon number (B)	+1/3	+1/3	+1/3
Electric charge (Q)	-1/3	+2/3	-1/3
Isospin (I)	-1/2	+1/2	0
Strangeness (S)	0	0	-1
mass (MeV/c^2)	$2.3^{+0.7}_{-0.5}$	$4.8^{+0.5}_{-0.3}$	95 ± 5

Table 4: Quantum numbers and masses associated to the three lighter quarks: u, d and s

474 The hadronic state are obtained from the decomposition of the following scalar prod-
 475 ucts of the fundamental representations of the group:

476

477 Meson ($q\bar{q}$) $3 \otimes \bar{3} = 1 \oplus 8$

478

479 Baryon (qqq) $3 \otimes 3 \otimes 3 = 10_S \oplus 8_M \oplus 8_M \oplus 1_A$

480

481 For the baryons without *c* or *b* quark, flavor and spin may be combined in an approxi-
 482 mate flavor-spin $SU(6)$, in which the six basic states are $d \uparrow, d \downarrow, \dots, s \downarrow$ (\uparrow, \downarrow = spin up,
 483 down). Then the baryons belong to the multiplets on the right side of

484

485 $6 \otimes 6 \otimes 6 = 56_S \oplus 70_M \oplus 70_M \oplus 20_A$

486

487 Here, the 56 representation can be decompose in an octet ($J^P = 1/2^+$) and a decuplet
 488 ($J^P = 3/2^+$), as can be seen in Figure 7 and Figure 8.

489 Among the hadrons, the special family of particles that contain at least one strange
 490 quark but not heavier quarks (like charm or bottom), are called hyperons. These are:
 491 the Λ (uds), the triplet $\Sigma^+(uus)$, $\Sigma^0(uds)$, $\Sigma^-(dds)$, the doublet $\Xi^-(dss)$, $\Xi^0(uss)$ and the
 492 $\Omega(sss)$ and the corresponding antiparticles. Ξ and Ω are the only hyperons containing more
 493 than one strange quark, hence they are called multi-strange baryons. Resonances shown in
 494 Figure reffig:decuplet having * with its name (e.g. $X^{*\pm}$) are particles with higher mass than
 495 the corresponding ground state particle with the same quark content. Different resonances
 496 with different lifetimes can probe different stages of the fireball expansion. The lifetime
 497 of some short-lived resonances is reported in Table 5. The ratios between resonances and

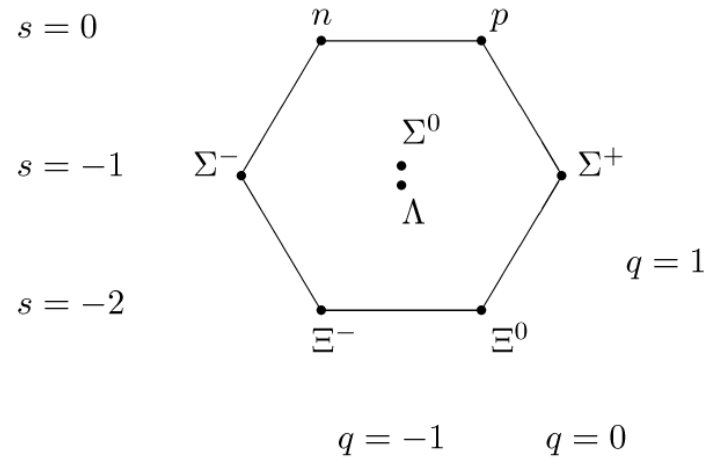


Figure 7: The $J^P = 1/2^+$ ground state baryon octet

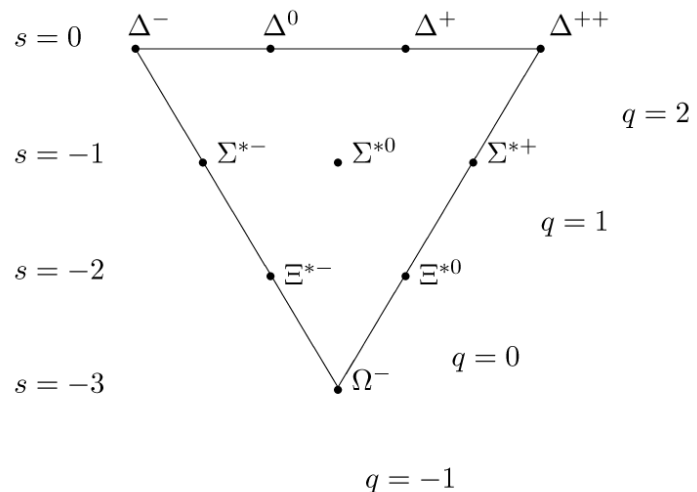


Figure 8: The $J^P = 3/2^+$ baryon decuplet

498 stable hadrons can be compared for resonances with different lifetimes and provide insights
 499 on the role of the re-scattering effect between the two freeze-out phases.

Particle	$\rho(770)$	$\Delta(1232)$	$K^*(892)$	$\Sigma(1385)$	$\Lambda(1520)$	$\Xi(1530)$	$\Phi(1020)$
Lifetime[c τ]	1.3 fm	1.7 fm	4.0 fm	5.5 fm	10.3 fm	22 fm	46 fm

Table 5: Lifetime of hadronic resonances

500 In the following, a general overview of the role of the strange quark within the QGP
 501 studies with heavy-ion collisions is given. And importance of the measurement of resonance
 502 is explained as probe of properties in hadronic phase between the chemical(T_{ch}) and the
 503 kinetic freeze-out(T_{kin}).

504 **3.1 Strange quark and hyperons**

505 The original interest in the strangeness in the context of the QGP comes from an idea by
 506 Johann Rafelski and Berndt Müller. In 1982, they suggested a possible signature for the
 507 formation of a QGP in a heavy-ion collision [22]. The key argument, at a fixed collision
 508 energy, rests on the different production mechanism of the s quark within two different
 509 systems:

- 510 **1. Hadron Gas (HG)** , where the degrees of freedom are the hadronic ones, as quark
 511 and gluons are confined
- 512 **2. QGP** , where the degrees of freedom are partonic ones, with quarks and gluons free
 513 with respect to each other

514 The mass of the hadrons is only partly due to the mass of the constituent valence
 515 quarks.

516 Naively speaking, the quarks ?dress up? due to the strong interaction that keeps them
 517 confined. Once they are free, as in a QGP, the quarks recover their bare masses. It was
 518 predicted that, if the QGP is formed, an enhancement of the strange quarks should occur,
 519 because the production of $s\bar{s}$ pairs becomes easier due to the lower energy needed. When
 520 the QGP cools down, these strange quarks eventually recombine into hadrons favoring also
 521 an enhancement of the number of strange hadrons. This effect is larger for hadrons with
 522 higher strangeness, with the following scaling for the number type:

523 $N_\Omega > N_\Xi > N_\Lambda$
 524 where N_Ω , N_Ξ , N_Λ are the number of produced Ω , Ξ and Λ . A certain enhancement of
 525 strange hadrons can occur also in a hadron gas system, but the processes of hadronisation
 526 in this case are relatively easy for K and Λ . and progressively harder for hadrons with
 527 higher strangeness, hence the relation would be:
 528

530 $N_\Omega < N_\Xi < N_\Lambda$.

531 The production of multi-strange hadrons with respect to pp - like collisions is considered
 532 to be a signature of the formation of the QGP and it was observed at SPS, RHIC and LHC.
 533 [23]

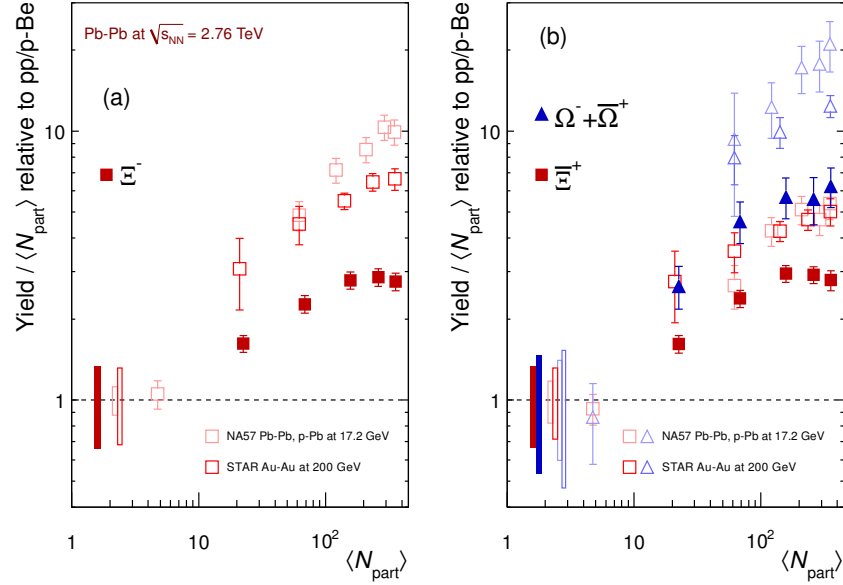


Figure 9: Enhancements in the rapidity range $|y| < 0.5$ as a function of the mean number of participants $\langle N_{part} \rangle$, showing LHC (ALICE, full symbols), RHIC and SPS (open symbols) data. Boxes on the dashed line at unity indicate statistical and systematic uncertainties on the pp or p-Be reference. Error bars on the data points represent the corresponding uncertainties for all the heavy-ion measurements and those for p-Pb at the SPS.

534 The measured enhancement factors of baryons with increasing strangeness content are
 535 reported in Figure 9 as a function of the number of participant nucleons, $\langle N_{part} \rangle$, in com-
 536 parison with similar measurements at SPS and RHIC. For p-Pb collisions there is no
 537 evidence of enhancement. For Pb-Pb collisions the enhancement increases with centrality
 538 and the effect is larger for particles with higher strangeness content, up to a factor ≈ 20 for
 539 Ξ s. No hadronic model has reproduced these observations and they can be interpreted as
 540 clear signal of QGP state formation. The comparison with results from the previous ex-
 541 periments shows that the relative enhancements decrease with increasing collision energy.
 542 An explanation of this behavior is given in terms of a statistical model, with canonical
 543 strangeness conservation. In a small system, with small particles multiplicities, quantum
 544 numbers conservation laws (such as strangeness) must be applied locally, event-by-event,

545 whereas in a large system, with many degrees of freedom, they can be applied in average,
 546 by means of the corresponding chemical potential. The conservation of quantum numbers
 547 is known to reduce the phase space available for particle production. This canonical sup-
 548 pression factor decreases with lower energy in the centre of mass of the collisions and could
 549 explain the larger enhancement for lower energy systems.

550 **3.2 Resonance production**

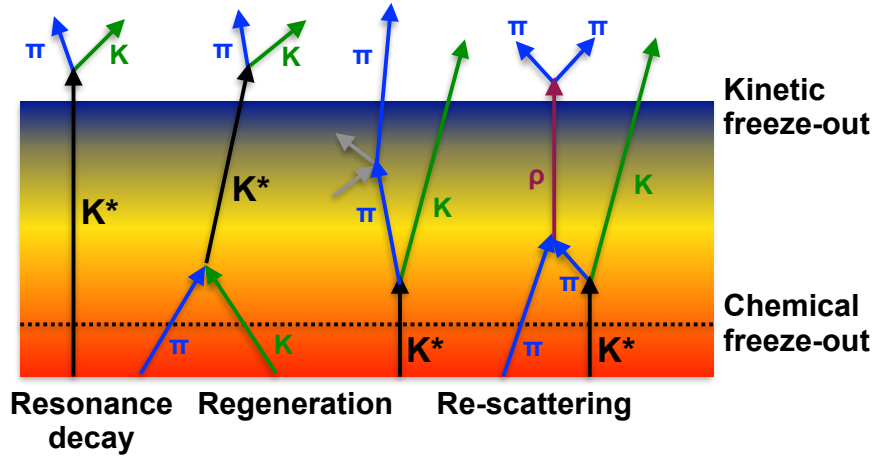


Figure 10: Hadronic phase

551 Resonances are particles with higher mass than the corresponding ground state particle
 552 with the same quark content. Hadronic resonances decay strongly, thus with a short
 553 lifetime, $\tau \sim$ few tenths of fm/c. The resonance natural width is given by $\Gamma = \bar{h}/\tau$, that
 554 is inversely proportional to the lifetime. Broad states with finite Γ decay very shortly
 555 after being produced and can be measured only by reconstruction of their decay products
 556 (or "daughters") in a detector. In heavy-ion collisions, hadronic resonances are produced
 557 within the bulk of the expanding medium, where they can decay while still traversing its
 558 volume. Decay products may interact with the other particles of the medium (mostly pions
 559 at the LHC), resulting in the impossibility of reconstructing the resonance, because the
 560 invariant mass of the daughters does not match that of the parent particle. Conversely,
 561 resonances may be regenerated as a consequence of pseudo-elastic collisions in the time
 562 lapse between the chemical (T_{ch}) and the kinetic freeze-out (T_{kin}). Re-scattering and
 563 regeneration depend on the individual cross section, hence lifetime, of the resonances and
 564 affect the measurement of their yield and momentum spectrum. The yield is decreased if the
 565 re-scattering dominates, vice versa the regeneration feeds the system with more particles.

566 The two effects may even compensate. Different resonances with different lifetimes can
567 probe different stages of the fireball expansion. The ratios between resonances and stable
568 hadrons can be compared for resonances with different lifetimes and provide insights on
569 the role of the re-scattering effect between the two freeze-out phases.

570 **4 A Large Ion Collider Experiment at the LHC**

571 ALICE (A Large Ion Collider Experiment) has been collecting data during the whole first
572 phase of the Large Hadron Collider operations, from its startup on the 23 November 2009
573 to the beginning of the first long technical shutdown in February 2013. During the first
574 three years of operations LHC provided pp collisions at 0.9, 2.76, 7 and 8 TeV, Pb–Pb colli-
575 sions at 2.76A TeV and finally p–Pb collisions at 5.02 TeV. The first section of this chapter
576 focuses on the LHC performance during this phase and includes details on the accelerator
577 parameters that allow the LHC to perform as a lead ion collider. A detailed description
578 of the ALICE detector follows in the section 4.2.1. ALICE has been designed and op-
579 timized to study the high particle-multiplicity environment of ultra-relativistic heavy-ion
580 collisions and its tracking and particle identification performance in Pb–Pb collisions are
581 discussed. The attention is drawn in particular on the central barrel detectors. Section
582 4.2.2 describes the ALICE Data Acquisition (DAQ) system, that also embeds tools for the
583 online Data Quality Monitoring (DQM). The final part of the chapter is dedicated to the
584 offline computing and reconstruction system based on the GRID framework.

585 **4.1 The Large Hadron Collider**

586 The Large Hadron Collider (LHC) [24] at CERN is the biggest particle accelerator world-
587 wide. The LHC project was approved in 1994 and construction works in the existing
588 underground tunnel started in 2001 after the dismantling of the LEP collider, which had
589 previously been built in the tunnel which is located under the Swiss-French border area
590 close to Geneva at a depth of 50 to 175 m. The LHC has a circumference of 26.7 km. By
591 design, its maximum achievable energies are 7 TeV for beam of protons and 2.76 TeV per
592 nucleon for beam of lead ions, thus providing collisions at $\sqrt{s} = 14$ TeV and $\sqrt{s_{NN}} = 5.5$
593 TeV, respectively. These would be the largest energies ever achieved in particle collision
594 experiments. The LHC is a synchrotron that accelerates two counter-rotating beams in
595 separate parallel beam pipes. In each of them bunches of particles travel many times
596 around the accelerator ring before the collision energy is reached. The accelerator has to
597 bend the beams around the ring, keep the bunches focused and accelerate them to their
598 collision energy. Finally, the spatial dimension of the bunches has to be minimized in order
599 to attain high luminosity, which ensure a high number of collisions per time interval at
600 the collision points, i.e. a high luminosity. A combination of magnetic and electric field
601 components performs the mentioned tasks. Despite the high luminosity reached, only a
602 very small fraction of the particles of two bunches collides in a single bunch crossing. The
603 others leave the interaction region essentially uninfluenced, are defocused, and continue to
604 circulate in the accelerator.

605 Injection of bunches into the LHC (Figure 11) is preceded by acceleration in the
606 LINAC2, PS booster, PS, and SPS accelerators. The acceleration sequence is slightly
607 different for heavy-ions, in which case bunches pass the LINAC3, LEIR, PS, and SPS

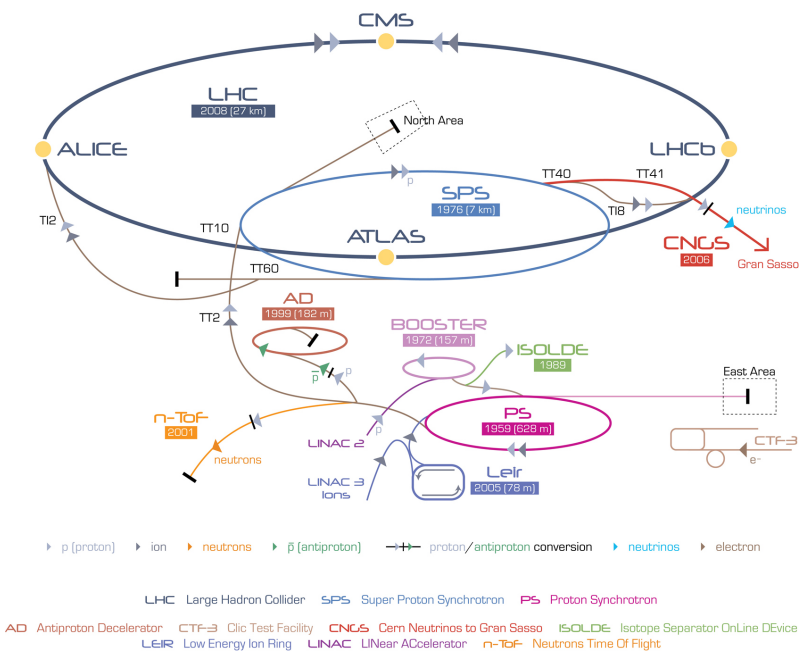


Figure 11: The CERN accelerator complex [2]

608 accelerators (more information can be found in [90]). Several injections to the LHC are
609 needed until all bunches of both beams are filled. The first pp collisions at 900 GeV centre-
610 of-mass energy were delivered by the LHC on September 10th 2008. Nine days later, the
611 operations were interrupted due to a failure in an electrical connection between two mag-
612 nets. The machine operators spent over a year repairing and consolidating the accelerator.
613 On November 20th 2009 low energy proton beams circulated again, and a few days later,
614 by achieving the energy of 1.18 TeV per proton beam, LHC became the most powerful
615 accelerator in the world. The first pp collisions at centre-of-mass energy of 7 TeV were
616 delivered in March 2010, and the first Pb?Pb collisions at centre-of-mass energy of 2.76
617 TeV per nucleon pair in November 2010. In 2010 the integrated luminosity delivered by
618 the LHC was $\sim 48 \text{ pb}^{-1}$ for pp collisions at $\sqrt{s} = 7 \text{ TeV}$ ($\sim 0.5 \text{ pb}^{-1}$ in ALICE) and \sim
619 $10 \mu\text{b}^{-1}$ for Pb?Pb at $\sqrt{s_{\text{NN}}} = 2.76 \text{ TeV}$ ($\sim 10 \mu\text{b}^{-1}$ in ALICE). In 2011 the beam energy
620 was the same as in 2010 both for pp and Pb-Pb. The performance of the LHC improved
621 in terms of luminosity with $\sim 5.61 \text{ fb}^{-1}$ for pp ($\sim 2 \text{ pb}^{-1}$ in ALICE) and $\sim 166 \mu\text{b}^{-1}$
622 for Pb-Pb collisions ($\sim 143.62 \mu\text{b}^{-1}$ in ALICE). In 2012, the centre-of-mass energy for pp
623 collisions was brought to 8 TeV and the integrated luminosity (up to December 2012, end
624 of the pp program) was $\sim 23.3 \text{ fb}^{-1}$ ($\sim 10 \text{ pb}^{-1}$ in ALICE). A pilot p-Pb run operated
625 at $\sqrt{s_{\text{NN}}} = 5.02 \text{ TeV}$ on September 2012, followed by a long p-Pb run on February 2013
626 with a delivered luminosity of 31.2 nb^{-1} . A very short pp run at $\sqrt{s} = 2.76 \text{ TeV}$ ended the
627 Run1 of the LHC program, marking the start of the first long shutdown (LS1) until the
628 end of 2014. Despite its excellent performance, the LHC has not yet achieved the nominal
629 parameters (\sqrt{s} , L), that is the main goal for the next ignition of the machine in 2015.
630 The LHC produces collisions in four so called Interaction Points (IPs) in correspondence
631 of which are located six detectors of different dimensions and with different goals, all able
632 to study the products of the interactions. These are:

633

634 **ALICE (A Large Ion Collider Experiment-IP₂)** [25] is a dedicated heavy-ion ex-
635 periment designed to study strongly-interacting matter at very high energy density. It
636 explores the phase transition to the QGP, its phase diagram, and its properties. Further-
637 more, ALICE will also study collisions of protons, on one hand as a baseline for heavy-ion
638 measurements and on the other hand it contributes to measurements of identified particles
639 by making use of its excellent particle identification capability and its acceptance at very
640 low transverse momenta.

641

642 **ATLAS (A Toroidal LHC ApparatuS-IP₁) and CMS (Compact Muon Solenoid**
643 **- IP₅)** [26][27] are general-purpose detectors for pp collisions that are built to cover the
644 widest possible range of physics at the LHC. Specific topics are the search for the Higgs
645 boson and physics beyond the Standard Model, e.g. new heavy particles postulated by
646 supersymmetric extensions (SUSY) of the Standard Model and evidence of extra dimensions.

647

648 **LHCb (The Large Hadron Collider beauty experiment-IP₈)** [28] is a dedicated

649 experiment for the study of heavy flavor physics at the LHC. In particular, the experiment
650 focuses on the study of CP violation and rare decays of beauty and charm particles, to
651 test the Standard Model and to search for evidence of New Physics. The LHCb physics
652 program is complementary to the flavor physics studies conducted at the B-factories and
653 to the direct searches for new particles performed at ATLAS and CMS.

654

655 **LHCf (Large Hadron Collider forward experiment-IP₁)** [29] measures forward
656 particles created during LHC collisions to provide further understanding of high energy
657 cosmic rays. The detector is placed close to the ATLAS experiment.

658

659 **TOTEM (TOTal Elastic and diffractive cross-section Measurement-IP₅)** [30]
660 measures the total cross-section, elastic scattering, and diffractive processes. The detector
661 is located close to the CMS experiment.

662

663 4.2 The ALICE project

664 The ALICE experiment at the LHC [31] has as main goal the study of nuclear matter
665 under extreme conditions of temperature and energy density such as those reached in ultra-
666 relativistic heavy-ion collisions. The aim is to verify the QCD prediction of the existence of
667 a phase transition from the common hadronic matter to the Quark-Gluon Plasma. Since
668 ALICE is the only LHC experiment specifically designed for Pb–Pb collisions, it has to
669 be able to cope with the large multiplicities associated with these collision systems and at
670 the same time has to cover as many QGP-related observables as possible. ALICE is also
671 interested in the study of pp interactions, as these are crucial for a comparison with Pb–Pb
672 collisions, to tune Monte Carlo models and per se, like the other LHC experiments. With
673 respect to these experiments, ALICE is endowed with an excellent Particle IDentification
674 (PID) performance, obtained combining different PID techniques from different detectors
675 that are optimized in different momentum (p) regions.

676 4.2.1 ALICE detector

677 ALICE is a complex of 14 detector subsystems (Figure 12) that can be classified in three
678 groups:

679

680 **Central detectors** are housed in a solenoid magnet which provides the experiment
681 with a 0.5 T magnetic field and covers the pseudo-rapidity interval $-0.9 < \eta < 0.9$ (corre-
682 sponding to a polar acceptance $\pi/4 < \theta < 3\pi/4$). The azimuthal acceptance is 2π . They
683 are mainly dedicated to vertex reconstruction, tracking, particle identification and momen-
684 tum measurement. Starting from the interaction region and going outward, we find the
685 following detectors:

- 686 • Inner Tracking System (ITS)
- 687 • Time Projection Chamber (TPC)
- 688 • Transition Radiation Detector (TRD)
- 689 • Time Of Flight (TOF)

690 In the mid-rapidity region there are also three detectors with limited azimuthal accep-
691 tance:

- 692 • High Momentum Particle Identification Detector (HMPID)
- 693 • PHOton Spectrometer (POHS)
- 694 • ElectroMagnetic CALorimeter (EMCAL)

695 **Muon spectrometer** is placed in the forward pseudo-rapidity region ($-4.0 < \eta < -2.5$) and consists of a dipole magnet and tracking and trigger chambers. It is optimized to
696 reconstruct heavy quark resonances (such as J/Ψ through their $\mu^+\mu^-$ decay channel) and
697 single muons.

698 **Forward detectors** are placed in the high pseudo-rapidity region (small angles with
699 respect to the beam pipe). They are small and specialized detector systems used for
700 triggering or to measure global event characteristics. They are:

- 701 • Time Zero (T0) to measure the event time with precision of the order of tens of
702 picoseconds, as needed by TOF
- 703 • VZERO (V0) to reject the beam-gas background and to trigger minimum bias events
- 704 • Forward Multiplicity Detector (FMD) to provide multiplicity information over a large
705 fraction of the solid angle ($-3.4 < \eta < -1.7$ and $1.7 < \eta < 5$)
- 706 • Photon Multiplicity Detector (PMD) to measure the multiplicity and the spatial
707 distribution of photons on an event-by-event basis in the $2.3 < \eta < 3.7$ region
- 708 • Zero Degree Calorimeter (ZDC) to measure and trigger on the impact parameter. The
709 ZDC consists of two calorimeters, one for neutrons (ZDC:ZN) and one for protons
710 (ZDC:ZP), and includes also an electromagnetic calorimeter (ZEM)

711 The ALICE global coordinate system [32] is a right-handed orthogonal Cartesian system
712 with the origin X, Y, Z = 0 at the centre of the detector. The three Cartesian axes are
713 defined as follows: the X axis pointing towards the centre of the LHC, the Y axis pointing
714 upward and the Z axis parallel to the local mean beam line pointing in the direction opposite

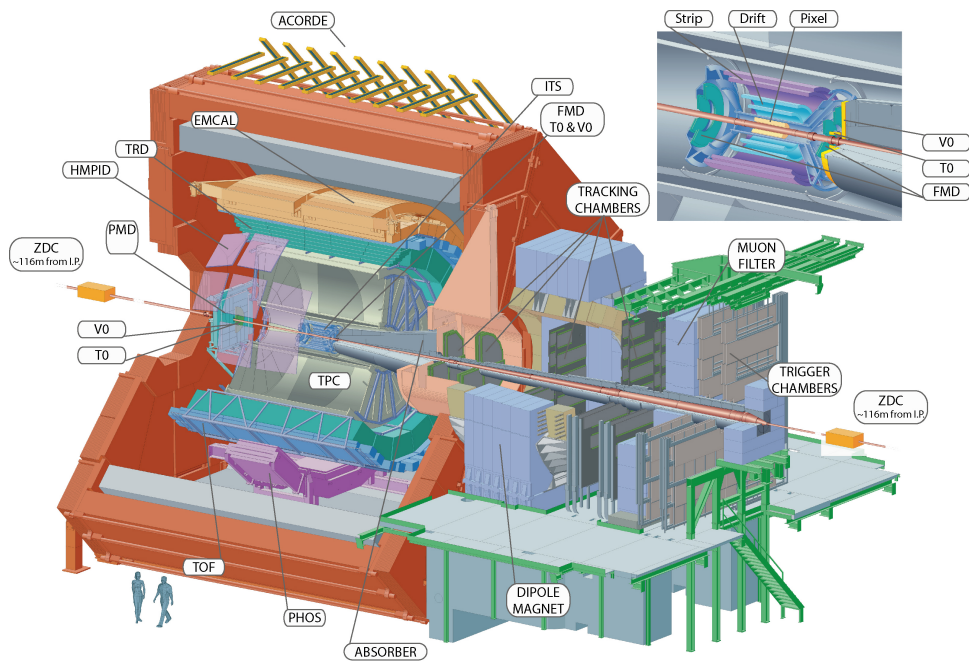


Figure 12: The ALICE detector

717 to the muon spectrometer. The azimuthal angle increases counter-clockwise from the
718 positive X axis ($\Phi = 0$) to the positive Y axis ($\Phi = \pi/2$) with the observer standing at
719 positive Z and looking at negative Z; the polar angle increases from the positive Z axis (θ
720 = 0) to the X-Y plane ($\theta = \pi/2$) and to the negative Z axis ($\theta = \pi$).

721 In the following Sections more specific descriptions of the detectors used in the identifi-
722 cation of the $\Xi(1530)^0$ baryons and in the determination of the characteristics of typical
723 collisions will be given.

724

725 ITS

726 The ITS [31] (Figure 13) is the barrel detector closest to the beam pipe. Its main goals
727 are:

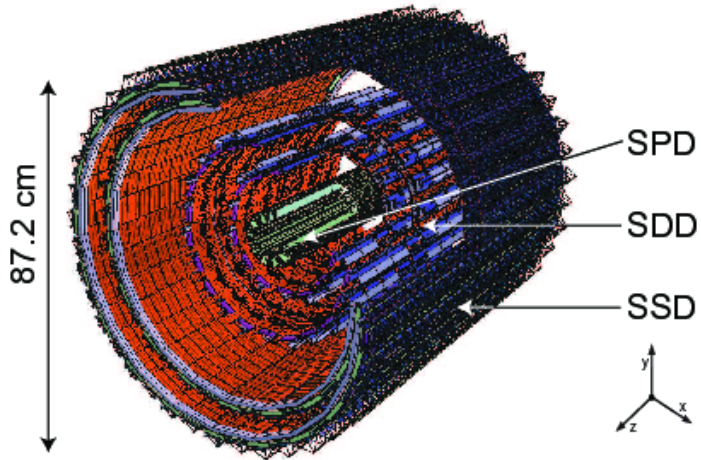


Figure 13: Schematic view of the ITS [3]

727

- 728 • to contribute with the TPC to the global tracking of ALICE by improving the angle
729 and momentum resolution
- 730 • to reconstruct the position of the primary interaction vertex
- 731 • to reconstruct secondary vertices from decays of heavy-flavor and strange particle
732 decays;
- 733 • to track and identify particles with momentum below $100 \text{ MeV}/c^2$
- 734 • to improve the momentum, impact parameter and angle resolution for the measure-
735 ment of high p_T particles performed with the TPC

- 736 • to reconstruct particles traversing dead regions of the TPC

737 The ITS surrounds the beam pipe (which is a 800 μm thick cylinder with an outer
 738 diameter of 2.9 cm) and consists of six cylindrical layers of silicon detectors located at radii
 739 between 4 cm and 43 cm. Due to the high track density, the two innermost layers are
 740 Silicon Pixel Detectors (SPD) which guarantee a high granularity. They are followed by
 741 two layers of Silicon Drift Detectors (SDD), while the two outmost layers are double-sided
 742 Silicon micro-Strip Detectors (SSD).

743 Since the momentum and impact parameter resolutions for low momentum particles
 744 are dominated by multiple scattering effects, the amount of material in the active volume
 745 has been minimized as much as possible. The granularity of the detector was optimized to
 746 keep the occupancy low in all the layers. With the technology chosen, the ITS detectors
 747 reach a spatial resolution of the order of a few tens of m resulting in a resolution on the
 748 impact-parameter⁵ better than 70 m in the r plane for $p_T > 1 \text{ GeV}/c$ and thus well suited
 749 for the reconstruction of heavy-flavor decays (see Figure 14).

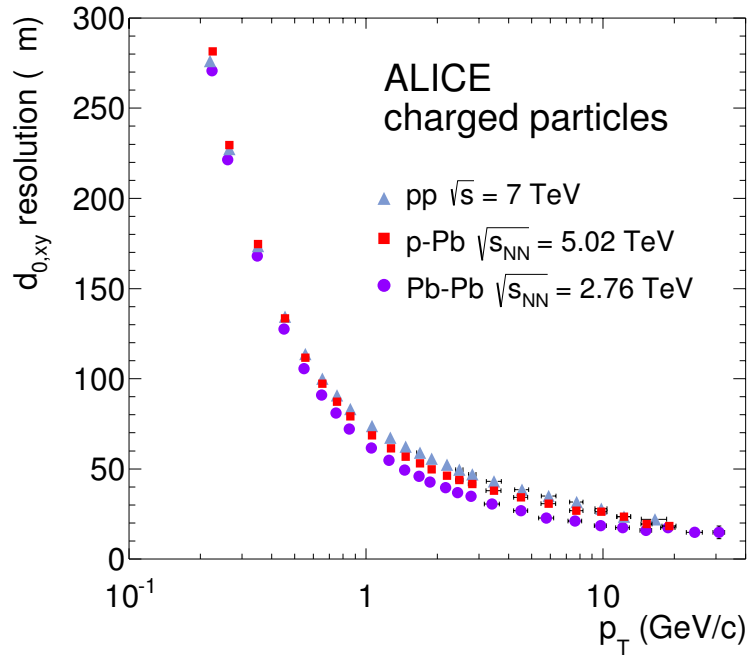


Figure 14: Track impact parameter resolution in the transverse plane ($r\phi$) vs p_T for charged particle

750 **TPC**

751 The TPC [33] (Figure 15) is the main tracking detector of the central barrel, optimized

752 to provide, together with the other central barrel detectors, charged- particle momentum
 753 measurements with good two-track separation, particle identification and vertex determina-
 754 tion. The TPC was designed for an excellent tracking performance in the high multiplicity
 755 environment of Pb–Pb collisions. For this reason, it was chosen to be a drift chamber,
 756 cylindrical in shape, 5 m long, with the inner radius ($r_{in} \sim 85$ cm) determined by the
 757 maximum acceptable track density, and the external one ($r_{ext} \sim 250$ cm) by the minimum
 758 track length for which dE/dx resolution is $< 10\%$. The TPC volume is filled with 90 m^3 of
 759 Ne/CO₂/N₂ (90/10/5). The readout planes are divided in 18 sectors in which multi-wire
 760 proportional chambers (with cathode pad readout) are housed. Because of its good dE/dx
 761 resolution, the TPC can identify particles with $p_T < 1\text{ GeV}/c$ on a track-by-track basis.

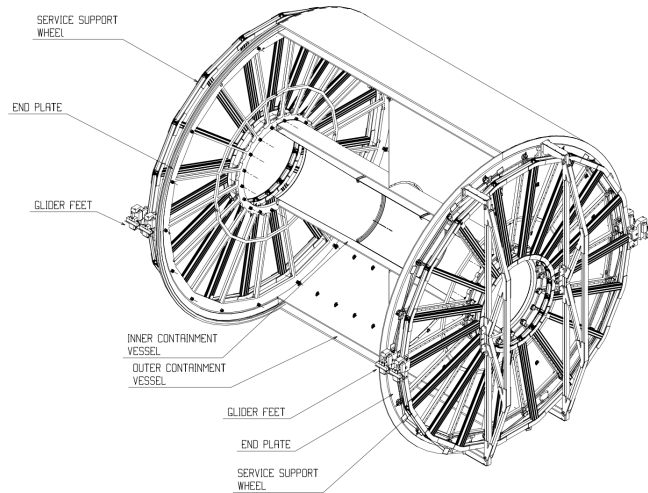


Figure 15: Schematic view of the TPC

762 Charged particles traveling through the TPC ionize the detector's gas; the measure-
 763 ment of this loss of energy is what we need to identify a particle. The physics observable
 764 in this case is the energy loss per unit length, within the matter crossed by the charged
 765 particle, which we call specific energy loss, also denoted by dE/dx . This is described by
 766 the Bethe–Bloch equation, 5, that highlights the key of the identification technique: this
 767 observable depends only on the charge and on velocity (β) of the particle, which, in turn,
 768 depends only on the momentum and the mass of the ionizing particle. Since momentum is
 769 already known due to track curvature and charge is unitary for most measured tracks, mea-
 770 suring the dE/dx allows us to indirectly determine mass and thus determine the particle
 771 species. The Bethe-Bloch equation gives the mean specific energy loss:

$$-\langle \frac{dE}{dx} \rangle = k_1 \cdot z^2 \frac{Z}{A} \cdot \frac{1}{\beta^2} \left[\frac{1}{2} \ln(k_2 \cdot m_e c^2 \cdot \beta^2 \gamma^2) - \beta^2 + k_3 \right] \quad (5)$$

772 where $\beta\gamma = p/Mc$ and: Z: atomic number of the ionized gas (in this case Ne/CO₂/N₂)
 773 A: mass number of the ionized gas (g/mol)
 774 m_e : electron mass
 775 z: electric charge of the ionizing particle in unit of electron charge e
 776 M: ionizing particle mass
 777 p: ionizing particle momentum
 778 β : ionizing particle velocity normalized to the light velocity c
 779 $\gamma = 1/\sqrt{1 - \beta^2}$, Lorentz factor
 780 k_1, k_2, k_3 : constants depending on the ionized medium
 781

782 For a given ionizing particle mass hypothesis, a given momentum and a given length
 783 of the trajectory in the ionizing medium, the total charge deposited along the trajectory
 784 is subject to statistical fluctuations. This random variable follows a Landau distribution,
 785 that give us the opportunity to measure the mean value hdE/dx . The long tail of the
 786 Landau distribution is usually truncated at 50%-70% of the collected signal.

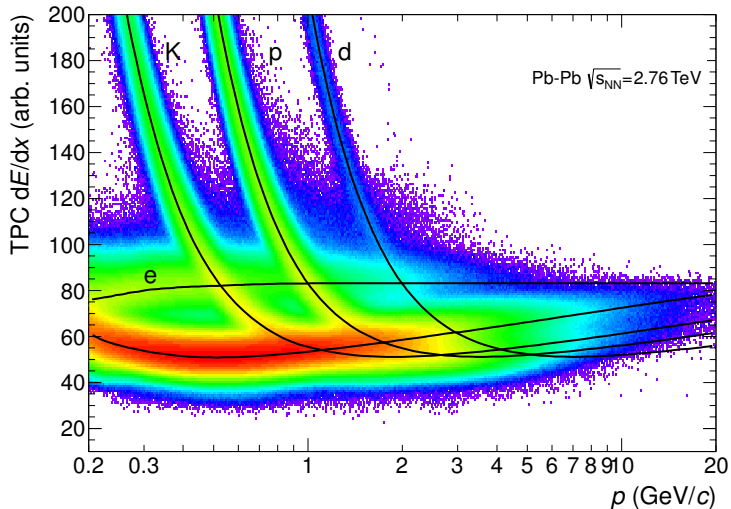


Figure 16: Specific energy loss (dE/dx) in the TPC vs. particle momentum in Pb–Pb collisions at $\sqrt{s_{NN}} = 2.76$ TeV. The lines show the parametrisations of the expected mean energy loss.

787 The specific energy loss in the TPC as a function of momentum is shown in Figure
 788 16. The different bands characteristic for $e^\pm, \pi^\pm, K^\pm, p^\pm$ are clearly visible. These
 789 are the evidence of the statistical distribution of the measured energy loss around the
 790 expected mean value. The expected value correspond to the prediction by a Bethe–Bloch
 791 experimental parametrization (superimposed as black lines in the Figure). For a track

792 within the TPC the relevant quantity to be considered for PID is the difference between
 793 the measured specific energy loss and the corresponding predicted value, by the Bethe-
 794 Bloch parametrization for a given measured momentum. If normalized to the resolution
 795 of the dE/dx measurement in the TPC, this difference could be expressed in number of
 796 σ (see Equation 6). In this way it is possible to estimate more quantitatively the goodness
 797 of a mass hypothesis. This also gives us the possibility to choose the strictness we want to
 798 adopt in the identification of a particle (n_σ , $n = 2, 3, 4$):

$$n_\sigma = \frac{(dE/dx)_{measured} - (dE/dx)_{Bethe-Bloch}}{\sigma_{TPC}} \quad (6)$$

V0

800 The VZERO detector [34] consists of two segmented arrays of plastic scintillator counters,
 801 called VZERO-A and VZERO-C, placed around the beam-pipe on either side of the IP:
 802 one at $Z = 340$ cm, covering the pseudo-rapidity range [2.8; 5.1], and the other at $Z = -90$
 803 cm (in front of the absorber), covering the pseudo-rapidity range [-3.7; -1.7]. They consist
 804 of 32 counters distributed in four rings, each divided in eight 45 sectors. Each counter
 805 is made of scintillator material embedded with WaveLength Shifting fibers. Clear fibers
 806 collect and transport the signal to photomultipliers 3 - 5 m far from the detector, inside
 807 the L3 magnet. The counters have a time resolution better than 1 ns. Their response is
 808 recorded in a time window of 25 ns around the nominal beam crossing time. The VZERO
 809 has an important role in rejecting background from beam-gas collisions (see, Figure 17)
 810 exploiting the relative time-of-flight measurement between the two arrays: when the beam-
 811 gas collision takes place outside the region between the two arrays, particles arrive 6 ns
 812 before or after the time of a beam-beam collision.

813 The VZERO is a trigger detector that will provide a minimum-bias trigger for all
 814 colliding systems to the central barrel detectors and three centrality triggers in p-Pb and
 815 Pb-Pb collisions (multiplicity, central and semi-central).

816 The first parameter to be determined in A-A (p-A) collisions is the centrality (multiplicity).
 817 This is defined according to the value of the impact parameter, b , and provides a geomet-
 818 rical scale of the overlapping region between the colliding nuclei: a collision will be defined
 819 from central to peripheral, as the impact parameter increases. The centrality of a collision
 820 is not directly available and must be deduced from a combination of experimentally mea-
 821 sured quantities and Monte Carlo simulations. There are a number of observables that can
 822 be measured and used as centrality estimators. The charged-particle multiplicity N_{ch} and
 823 the transverse energy E_T measured around mid-rapidity are measurable quantities related
 824 to the energy deposited in the interaction region (these are therefore related to N_{part}).
 825 These variables increase significantly increasing the centrality of the collisions. Another
 826 measurable quantity to estimate the centrality is the zero-degree energy EZDC, namely
 827 the energy carried by spectator nucleons $N_{spec} = 2A - N_{part} = E_{ZDC}/E_A$, where E_A is
 828 the beam energy per nucleon. Typically a measured distribution of one of the previous
 829 observables is mapped to the corresponding distribution obtained from phenomenological

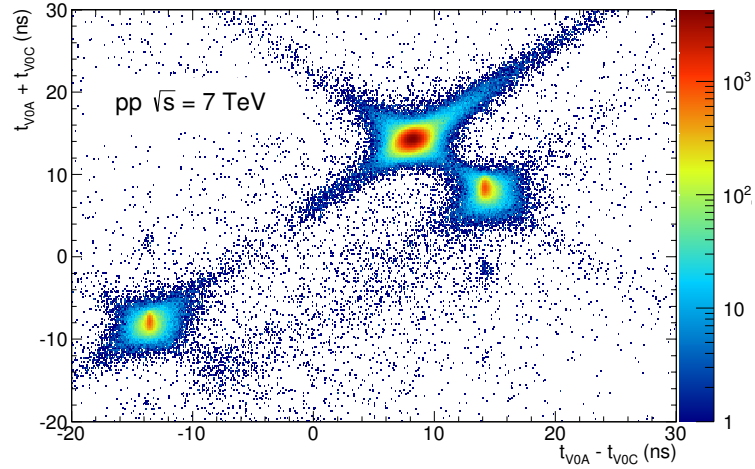


Figure 17: Correlation between the sum and difference of signal times in V0A and V0C. Three classes of events collisions at (8.3 ns, 14.3 ns), background from Beam 1 at (-14.3 ns, -8.3 ns), and background from Beam 2 at (14.3 ns, 8.3 ns) can be clearly distinguished.

830 Glauber calculations. The Glauber model [35, 36] uses a semi-classical approach: the A?A
 831 collision is assumed to be an incoherent superposition of N elementary nucleon- nucleon
 832 collisions. The main parameters of the model are the inelastic nucleon- nucleon collision
 833 cross-section σ_n and the nuclear density distribution $\rho(r)$. In practice, the simulated dis-
 834 tribution well reproduce the measured distribution or the latter is fitted with an analytical
 835 function. The experimental distribution can then be divided in classes with sharp cuts on
 836 the measured observable (E_{ZDC} , E_T or N_{ch}). These "centrality" classes will correspond to
 837 well defined percentage of the integral of the distribution. A given centrality class in the
 838 measured distribution, corresponds to the same class in the simulated distribution, where
 839 the main geometrical variables (N_{part} , N_{coll} and T_{AA}) can be determined. The number of
 840 classes that can be defined depends on the resolution achievable on the selection variable.
 841 In the analysis described in this thesis the centrality(multiplicity) estimation is based on
 842 the measurement of the multiplicities from the VZERO scintillators [37][38]. This is the
 843 method that achieve the best centrality resolution: it ranges from 0.5% in central to 2%
 844 in peripheral collisions. Other methods, as the ones based on the E_{ZDC} measurement or
 845 based on the estimate of the number of tracks in the SPD or TPC, are used to asses a
 846 systematic uncertainty on the centrality determination. The distribution of the VZERO
 847 amplitudes is shown in Figure 18 where the centrality(multiplicity) percentiles are also
 848 indicated.

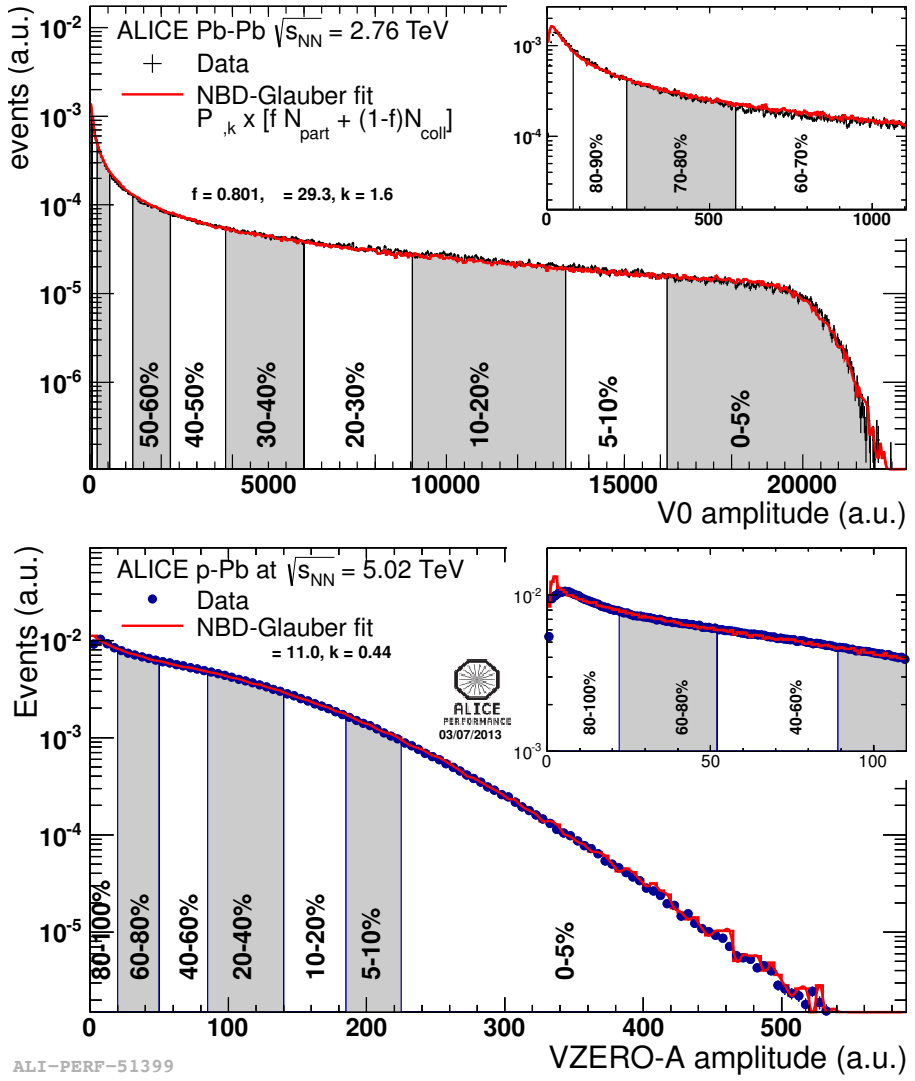


Figure 18: Distribution of the V0 amplitude (sum of V0A and V0C in top, V0A in bottom). The inset shows a magnified version of the most peripheral region.

849 **4.2.2 Data Acquisition (DAQ) and trigger system**

850 The architecture of data acquisition is shown in Figure 19. The tasks of the ALICE DAQ
 851 system are the assembly of event informations from individual detectors into complete
 852 events (event building) as well as buffering and export of assembled events to permanent
 853 storage. The DAQ is designed to process a data rate up to 1.25 GB/s in heavy-ion runs.
 854 Event building is done in two steps. Data from the detectors is received by Detector Data
 855 Links (DDLs) on Local Data Concentrators (LDCs). The LDCs assemble the data into
 856 sub-events that are then shipped to Global Data Collectors (GDCs). A GDC re- ceives all
 857 sub-events from a given event and assembles them into a complete event. These events are
 858 subsequently stored on a system called Transient Data Storage (TDS).

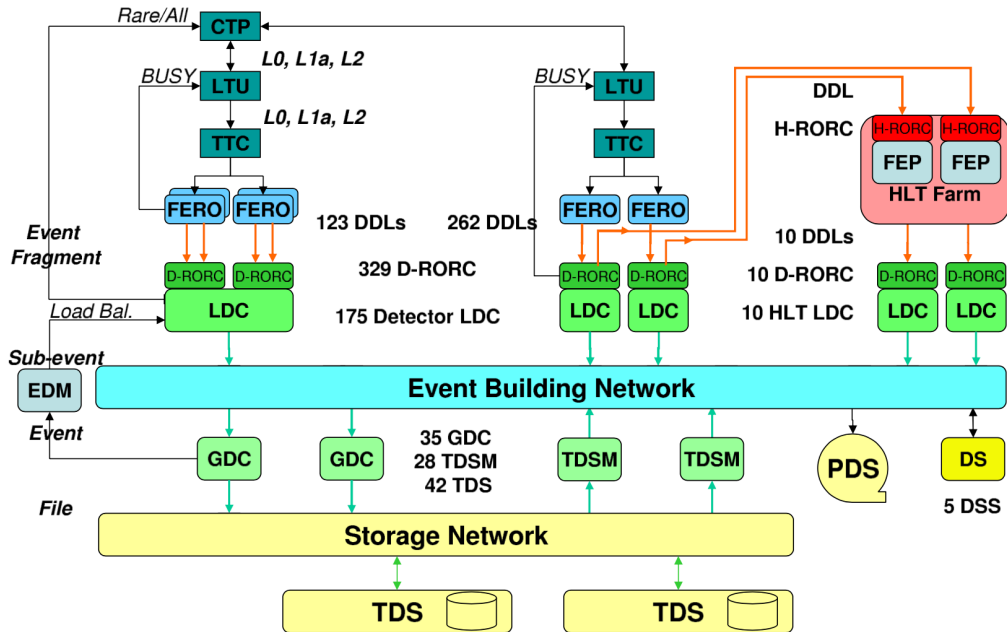


Figure 19: The overall architecture of the ALICE DAQ and the interface to the HLT system.

859 ALICE can simultaneously take data in several partitions, where a set of detec-
 860 tors can store their outputs. Since a partition is a group of commonly controlled detectors, a
 861 given detector can only be active in one partition at a time. The ac-
 862 tive detectors in a given partition may be assigned to data taking groups called clusters, for which triggers

863 can be defined. Therefore, upon a trigger only a sub-set of the whole partition may
864 be read out. Furthermore, a triggering detector does not have to be necessarily part of
865 the partition. ALICE has a two-layer trigger architecture [39]. The low-level trigger is a
866 hardware trigger called Central Trigger Processor (CTP). The High-Level Trigger (HLT)
867 is implemented as a pure software trigger. The CTP combines inputs from different trigger
868 sources, namely the various detectors. These inputs are single signals, like a hit in the
869 detector, or, can be the result of fast calculation performed directly in the detectors. The
870 HLT allows the implementation of sophisticated logic for the triggering. In contrast to the
871 CTP which governs the readout of the detectors, the HLT receives a copy of the data read
872 out from the detectors and processes them. The hardware trigger combines the trigger
873 signals of the various detectors to decide if an event is accepted, that means it is read out
874 and written to disk. Several trigger levels reduce the event rate depending on the input
875 signals. The first level, called L0, is delivered after 1.2 ?s, while the second, called L1,
876 after 6.5 ?s. The final trigger, L2, is delivered after 100 ?s, upon completion of the drift
877 time in the TPC. Only after an L2 trigger the event is finally stored. The rates of different
878 trigger classes are very different. By definition minimum-bias triggers have the highest
879 rate; other triggers that look for rare signals are characterized by much lower rates. In
880 order to cope with different scenarios, downscaling factors can be applied to the trigger
881 classes individually, i.e. only every nth event fulfilling the trigger condition is read out. The
882 total recording rate is limited by the maximum bandwidth of data that can be recorded
883 to disk and tape. The ALICE software trigger, called HLT, is a farm of multiprocessor
884 computers. The aim is to have about 1000 PCs processing the data in parallel allowing
885 an online analysis of the events. A trigger decision comes from the analysis of a more
886 comprehensive set of information than what happens for the hardware trigger, giving the
887 possibility to apply more sophisticated triggers. Examples include triggers on high energy
888 jets or on muon pairs. Furthermore, the HLT can significantly reduce the event size by
889 selecting regions of interest (partial readout of detectors) and by further compression of the
890 data. The HLT receives a copy of the raw data and performs per detector reconstruction,
891 partly aided by hardware coprocessors. Subsequently, the trigger decision is based on the
892 global reconstructed event. In the same step a region of interest can be selected. In the
893 last optional step, if the trigger decision is positive, the data are compressed. The trigger
894 decision, partial readout information, compressed data, and the re- construction output
895 is sent to LDCs and subsequently processed by the DAQ. In terms of the overall DAQ
896 architecture, data sent by HLT is treated like stemming from a detector.

897 **4.2.3 ALICE offline software frame work**

898 The required computing resources for the reconstruction and analysis of the raw data as
899 well as the production of simulated events needed for the understanding of the data exceed
900 the computing power of single institutes and even centers like CERN. Therefore, institutes
901 that are part of the Collaboration also provide storage and computing resources. Distribu-
902 tion of the data for reconstruction and analysis cannot be performed manually and this
903 led to the need for an automated system. The concept of a decentralized computing model
904 called Grid [40] was identified as a solution.

905

906 *The AliEn Framework*

907 The Grid paradigm implies the unification of resources of distributed computing center,
908 in particular computing power and storage, to provide them to users all over the World.
909 It allows computing center to offer their resources to a wider community and the local re-
910 sources to be shared by an entire collaboration. Software that implements the Grid concept
911 is called Grid middleware. ALICE has developed a Grid middleware called AliEn [41] since
912 2001. An ALICE user employs AliEn to connect to the ALICE Grid which is composed
913 of a combination of general services that are provided by many Grid middleware solutions
914 and ALICE-specific services provided by AliEn. Parts of the ALICE Grid are: i) a global
915 file catalog that is a directory of files in storage elements distributed over the Globe, ii)
916 the automatic matching of jobs for execution to a suitable location in one of the connected
917 sites, iii) a shell-like user interface and iv) API9 services for the ROOT framework [42].

918

919 *AliRoot Framework*

920 AliRoot [31] is the offline framework for simulation, alignment, calibration, reconstruction,
921 visualization, quality assurance, and analysis of experimental and simulated data. It is
922 based on the ROOT framework. Most of the code is written in C++ with some parts in
923 Fortran that are wrapped inside C++ code. Re-usability and modularity are the basic
924 features of the AliRoot framework. Modularity allows parts of the code to be replaced,
925 with minimum or no impact on the rest (for example changing the event generator, the
926 transport Monte Carlo or the reconstruction algorithms). This is achieved implementing
927 abstract interfaces. In addition codes for each detector subsystem are independent modules
928 with their specific code for simulation and reconstruction and the code can be developed
929 concurrently with minimum interference. Re-usability is meant to maintain a maximum
930 amount of backward compatibility as the system evolves.

931 The central module of the AliRoot framework is STEER (Figure 20) which provides
932 several common functions such as: steering of program execution for simulation, reconstruc-
933 tion and analysis; general run management, creation and destruction of data structures,
934 initialization and termination of program phases; base classes for simulation, event genera-
935 tion, reconstruction, detectors elements. For event simulation the framework provides the
936 following functionality:

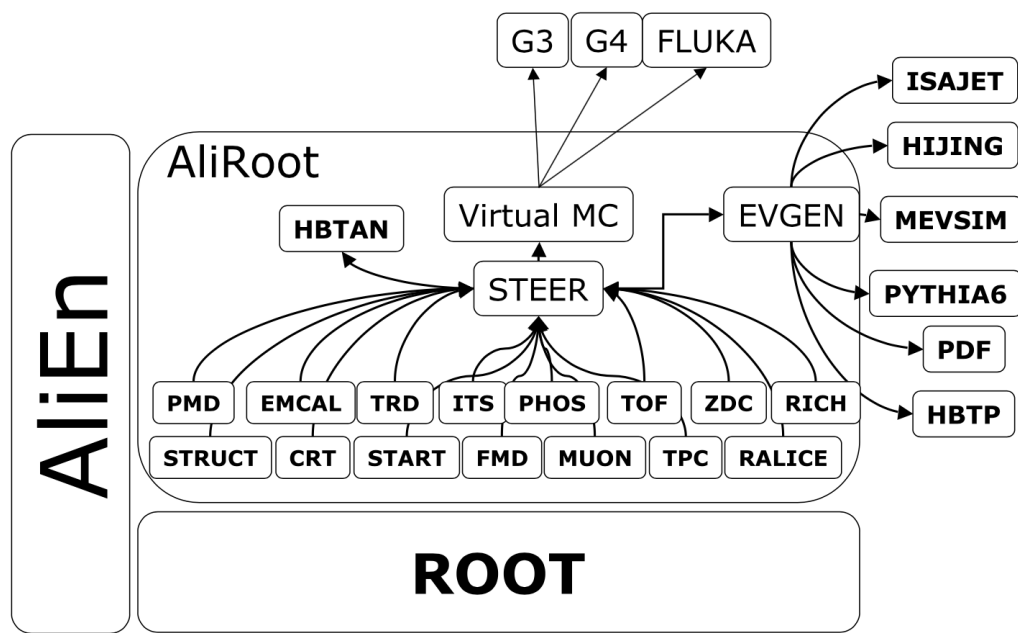


Figure 20: Schematic view of the AliRoot framework

937 **5 Measurement of $\Xi(1530)^0$ production in p–Pb and Pb–Pb**

938 The measurement of resonance production in p–Pb collisions helps to disentangle cold
939 nuclear matter effects from genuine hot medium effects and contribute to the study of
940 the system size dependence of re-scattering in the hadronic phase. And the measurement
941 in ultra-relativistic heavy-ion collisions such as Pb–Pb collisions, provide information on
942 the properties of hadronic medium and different stage of its evolution. In order to study
943 the particle production mechanism in the hadronic phase between the chemical and ki-
944 netic freeze-out, the $\Xi(1530)^0$ resonance production at mid-rapidity ($-0.5 < y_{\text{CMS}} < 0$) is
945 measured in p–Pb collisions $\sqrt{s_{\text{NN}}} = 5.02$ TeV and in Pb–Pb collisions with $|y| < 0.5$ at
946 $\sqrt{s_{\text{NN}}} = 2.76$ TeV with the ALICE experiment, via the reconstruction of its hadronic decay
947 into $\Xi\pi$.

948 **5.1 $\Xi(1530)^0$ -reconstruction**

949 The Ξ^{*0} production in p–Pb and Pb–Pb collisions at mid-rapidity has been studied in dif-
950 ferent multiplicity classes, from very central to peripheral collisions. The analysis strategy
951 is based on the invariant mass study of the reconstructed pairs (referred to as the candi-
952 dates) whose provenance could be the decay of a Ξ^{*0} baryon into charged particles. The
953 decay products (also called daughters in the text) are identified as oppositely charged Ξ and
954 π among the tracks reconstructed in the central barrel. The event selection, track selec-
955 tion and the particle identification strategy is described. The raw signal yield is extracted
956 by fitting the background-subtracted invariant mass distribution in several transverse mo-
957 mentum intervals. In order to extract the p_{T} -dependent cross section, these yields are
958 corrected for efficiency. The p_{T} -dependent correction due to the detector acceptance and
959 reconstruction efficiency, $(\text{Acc} \times \epsilon_{\text{rec}})(\text{pt})$, is computed from a Monte Carlo simulation.
960 The absolute normalisation is then performed, by dividing for the number of the events in
961 each multiplicity and centrality classes.

962 **5.1.1 Data sample and event selection**

963 A description of the ALICE detector and of its performance during the LHC Run 1 (2010–
964 2013) can be found in [31, 43]. The data sample in the analysis from Pb–Pb collisions with
965 energy of $\sqrt{s_{\text{NN}}} = 2.76$ obtained during 2011 and the sample of p–Pb run at $\sqrt{s_{\text{NN}}} = 5.02$
966 TeV was recorded in 2013.

967 Due to the asymmetric energies of the proton (4 TeV) and lead ion (1.57 A TeV) beams,
968 the centre-of-mass system in the nucleon-nucleon frame is shifted in rapidity by $\Delta y_{\text{NN}} =$
969 0.465 towards the direction of the proton beam with respect to the laboratory frame of
970 the ALICE detector [5]. For the analysed p–Pb data set, the direction of the proton beam
971 was towards the ALICE muon spectrometer, the so-called “C” side, standing for negative
972 rapidities; conversely, the Pb beam circulated towards positive rapidities, labelled as “A”

973 side in the following. The analysis in this paper was carried out at midrapidity, in the
974 rapidity window $-0.5 < y_{\text{CMS}} < 0$.

975 The minimum-bias trigger during the p–Pb run was configured to select events by
976 requiring a logical OR of signals in V0A and V0C [43], two arrays of 32 scintillator detectors
977 covering the full azimuthal angle in the pseudo-rapidity regions $2.8 < \eta_{\text{lab}} < 5.1$ and
978 $-3.7 < \eta_{\text{lab}} < -1.7$, respectively [44]. In the data analysis it was required to have a
979 coincidence of signals in both V0A and V0C in order to reduce the contamination from
980 single-diffractive and electromagnetic interactions. Out of this sample in p–Pb collision
981 events about 109.3 million events, 93.9 million events satisfy the following selection criteria
982 and have been actually used for the analysis.

983 The Pb–Pb collisions data sample was selected by online centrality trigger requiring a
984 signal in the forward V0 detectors[38] to record enhanced data in central collision. The
985 data consists of 24.8 million events in most central collisions (0-10%), 21.8 million events in
986 semi-central collisions (10-50%) and 3.5 million events with minimum-bas trigger (0-90%).
987 Among 49.6 million events in total, 43.0 million events have been analyzed as passed the
988 criteria below.

- 989 • Events with z-coordinate of primary vertex (V_z) falling within ± 10 cm from the
990 interaction point
- 991 • Rejection of pile-up event
- 992 • Requiring primary tracks to have at least one hit in one of the two innermost layers
993 of the ITS (silicon pixel detector, SPD)
- 994 • p–Pb: multiplicity ranges in percentile (V0A): 0-20%, 20-40%, 40-60%, 60-100% and
995 MB(0-100%)
- 996 • Pb–Pb: centrality classes (V0A and V0C): 0-10%, 10-40%, 40-80% and MB (0-80%)

997 The distribution of the vertex z position of the accepted events in p–Pb collision is
998 reported on left panel in Figure 21 and corresponding figure but obtained from Pb–Pb
999 collisions is shown on right panel in Figure. 21. Events with $|V_z| < 10$ cm have been used
1000 to ensure a uniform acceptance in the central pseudo-rapidity region, $|\eta| < 0.8$, where the
1001 analysis is performed. This cut reduces the total number of events to 97.5 million events,
1002 that is the $\sim 89.2\%$ of the initial sample in p–Pb collisions and 43.04 million events which
1003 is $\sim 86.8\%$ of the initial sample in Pb–Pb collisions are survived.

1004 Fig. 22 shows the multiplicity distribution of the accepted events in p–Pb collision
1005 divided in bins of percentile. The each color on the histogram indicate the multiplicity
1006 ranges used in this analysis. Corresponding events for each multiplicity range are in Table
1007 6.

1008 The distribution of centrality in each trigger used to select the events in Pb–Pb collision
1009 is shown in Fig. 23 and the reason why the centrality has step structure is that there are

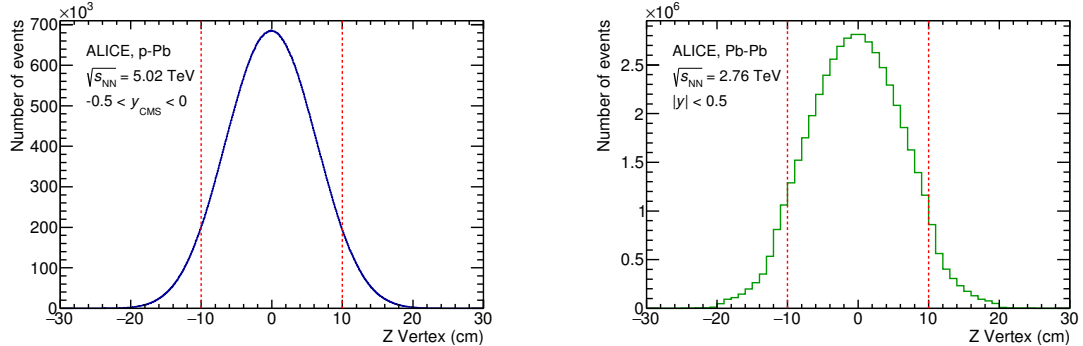


Figure 21: Vertex-z coordinate distribution of the accepted events in p–Pb collision(Left) and in Pb–Pb collisions(Right). The red dashed line indicates vertex cut

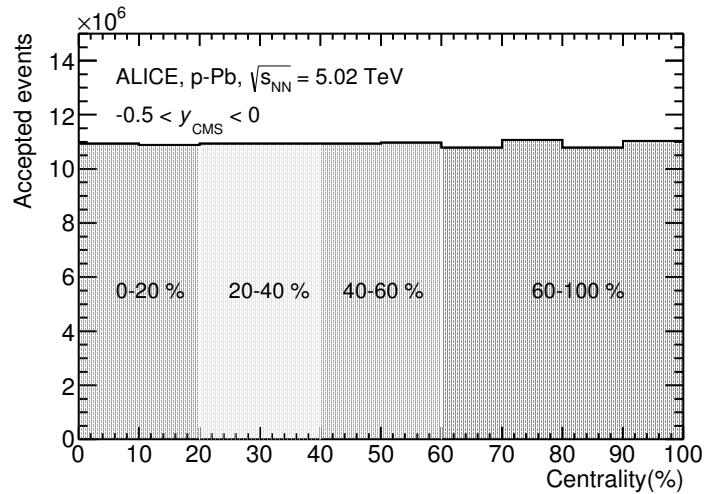


Figure 22: Multiplicity distribution of accepted events in p–Pb collision in percentile. The each color and labels define the four intervals in which the analysis is performed.

1010 three different trigger classes classified by the amplitude threshold on VZERO detector.
 1011 Because the distribution of events as function of centrality is not a flat, this may lead to
 1012 additional bias, in particular when one needs to combine the results from different triggers.
 1013 For example, events from 40-80% centrality bin have bias with high statistics in 40-60%. In
 1014 order to avoid this effect, we have applied a flattening procedure to have flat distribution
 1015 of events as function of centrality. A brief explanation of the method is below :

- 1016 1. Histograms are obtained for the effective mass distribution in 1% centrality bins and
 1017 for the centrality distribution
- 1018 2. The effective mass distributions are scaled in each 1% centrality bin by a factor:
 1019 Factor = $N_{\text{event}} \text{ in 20-40\%} / 20 / N_{\text{event}} \text{ in current 1\% bin}$
- 1020 3. Each bin in the centrality distribution is scaled using the factor described above
- 1021 4. Histograms are added for centrality bins of interest: 0-10%, 10-40%, 40-80%, 0-80%

1022 The resulting number of events in each centrality classes is summarized in Table 6.

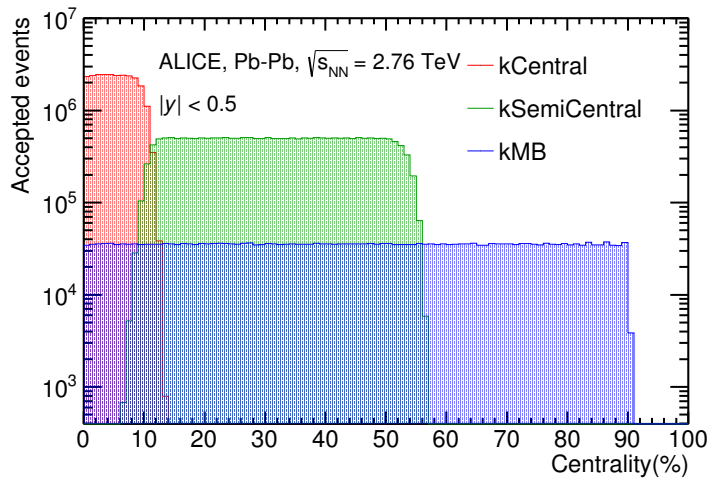


Figure 23: Centrality distribution of three different trigger classes.

p-Pb	0-20%	21.82×10^6
	20-40%	21.86×10^6
	40-60%	21.91×10^6
	60-100%	43.68×10^6
Pb-Pb	0-10%	5.58×10^6
	10-40%	16.73×10^6
	40-80%	22.31×10^6

Table 6: Number of accepted and analyzed events per multiplicity/centrality interval

5.1.2 Track and topological selection

In comparison with the Ξ^{*0} analysis carried out in pp collisions at $\sqrt{s} = 7$ TeV [7], track and topological selections were revised and adapted to the p-Pb dataset. Pions from strong decays of Ξ^{*0} were selected according to the criteria for primary tracks. As summarized in Table 7, all charged tracks were selected with $p_T > 0.15$ GeV/c and $|\eta_{\text{lab}}| < 0.8$, as described in Ref. [43]. The primary tracks were chosen with the Distance of Closest Approach (DCA) to PV of less than 2 cm along the longitudinal direction (DCA_z) and lower than $7\sigma_r$ in the transverse plane (DCA_r), where σ_r is the resolution of DCA_r . The σ_r is strongly p_T -dependent and lower than 100 μm for $p_T > 0.5$ GeV/c [43]. To ensure a good track reconstruction quality, candidate tracks were required to have at least one hit in one of the two innermost layers (SPD) of the ITS and to have at least 70 reconstructed points in the Time Projection Chamber (TPC), out of a maximum of 159. The Particle IDentification (PID) criteria for all decay daughters are based on the requirement that the specific energy loss (dE/dx) is measured in the TPC within three standard deviations (σ_{TPC}) from the expected value (dE/dx_{exp}), computed using a Bethe-Bloch parametrization [43].

Common track selections	$ \eta_{\text{lab}} $	< 0.8
	p_T	> 0.15 GeV/c
	PID $ (dE/dx) - (dE/dx)_{\text{exp}} $	$< 3 \sigma_{\text{TPC}}$
Primary track selections	DCA_z to PV	< 2 cm
	DCA_r to PV	$< 7\sigma_r$ - $10\sigma_r$ (p_T)
	number of SPD points	≥ 1
	number of TPC points	> 70
	χ^2 per cluster	< 4

Table 7: Track selections common to all decay daughters and primary track selections applied to the charged pions from decays of Ξ^{*0} .

Since pions and protons from weak decay of Λ ($c\tau = 7.89$ cm [1]) and pions from weak decay of Ξ^- ($c\tau = 4.91$ cm [1]) are produced away from the PV, specific topological and

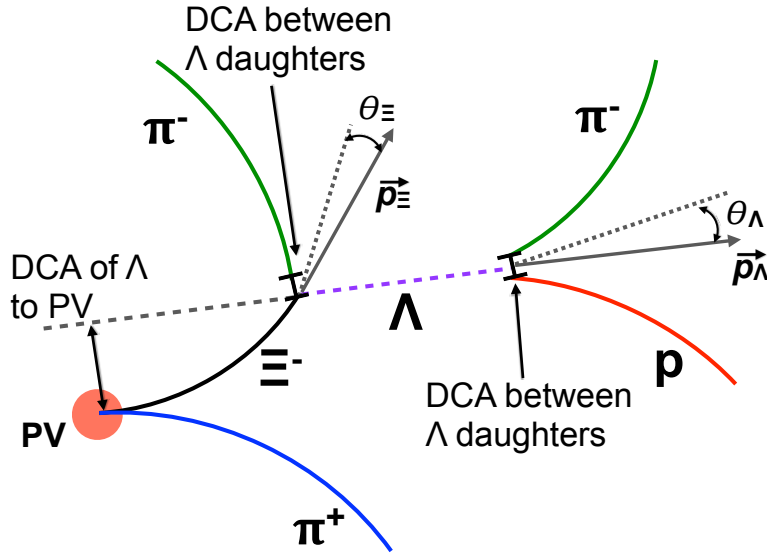


Figure 24: Sketch of the decay modes for Ξ^{*0} and depiction of the track and topological selection criteria.

1040 track selection criteria, as summarized in Table 8, were applied [6, 7, 45].

Topological cuts	p-Pb	Pb-Pb
DCA _r of Λ decay products to PV	> 0.06 cm	> 0.11 cm
DCA between Λ decay products	< 1.4 cm	< 0.95 cm
DCA of Λ to PV	> 0.015 cm	> 0.06
$\cos\theta_\Lambda$	> 0.875	> 0.998
$r(\Lambda)$	$0.2 < r(\Lambda) < 100$ cm	$0.2 < r(\Lambda) < 100$ cm
$ M_{p\pi} - m_\Lambda $	< 7 MeV/ c^2	< 7 MeV/ c^2
DCA _r of pion (from Ξ^-) to PV	> 0.015 cm	> 0.035 cm
DCA between Ξ^- decay products	< 1.9 cm	< 0.275
$\cos\theta_\Xi$	> 0.981	> 0.9992
$r(\Xi^-)$	$0.2 < r(\Xi^-) < 100$ cm	$0.2 < r(\Xi^-) < 100$ cm
$ M_{\Lambda\pi} - m_\Xi $	< 7 MeV/ c^2	< 7 MeV/ c^2

Table 8: Topological and track selection criteria.

1041 In the analysis of Ξ^{*0} , Λ and π from Ξ^- were selected with a DCA of less than 1.9 cm
 1042 and with a DCA_r to the PV greater than 0.015 cm. The Λ daughter particles (π and p)

¹⁰⁴³ were required to have a DCA_r to the PV greater than 0.06 cm, while the DCA between the
¹⁰⁴⁴ two particles was required to be less than 1.4 cm. Cuts on the invariant mass, the cosine
¹⁰⁴⁵ of the pointing angle ($\theta_\Lambda, \theta_\Xi$) and the radius of the fiducial volume ($r(\Lambda), r(\Xi)$) in Table 8
¹⁰⁴⁶ were applied to optimize the balance of purity and efficiency of each particle sample.

1047 **5.1.3 Particle identification**

1048 PID selection criteria are applied for

- 1049 1. π^\pm (last emitted π) and proton from Λ
1050 2. π^\pm (second emitted π) from Ξ^\pm
1051 3. π^\pm (first emitted π) from $\Xi(1530)^0$

1052 by using TPC. On TPC dE/dx versus momentum distribution, 3σ cuts are applied to TPC
1053 for selecting each of the particles. The TPC dE/dx selection allows to have better signal
1054 with $\sim 20\%$ increase of significance.

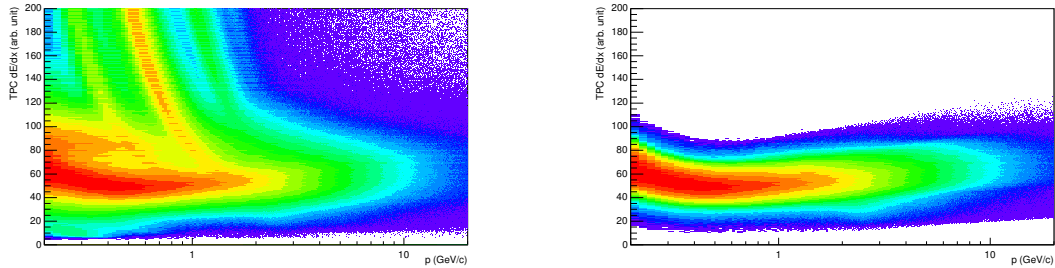


Figure 25: TPC dE/dx as function of transverse momentum for total (top) and selected first emitted π in 3σ (bottom)

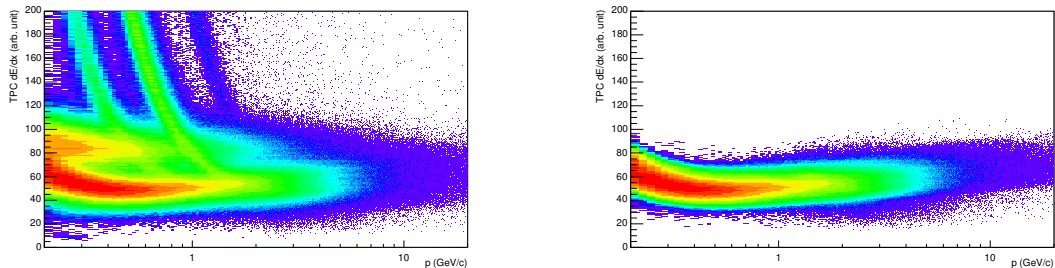


Figure 26: TPC dE/dx as function of transverse momentum for total (top) and selected second emitted π in 3σ (bottom)

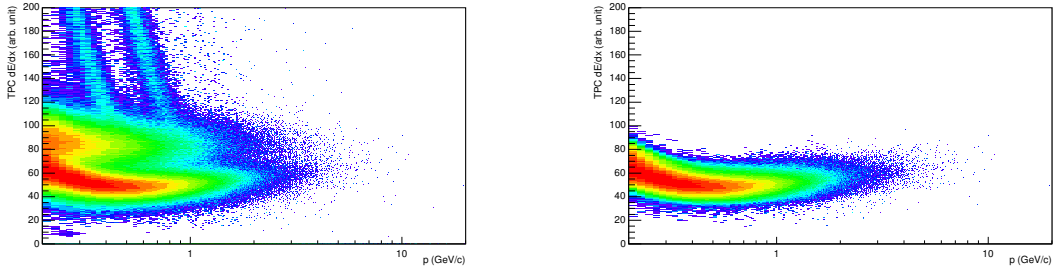


Figure 27: TPC dE/dx as function of transverse momentum for total (top) and selected last emitted π in 3σ (bottom)

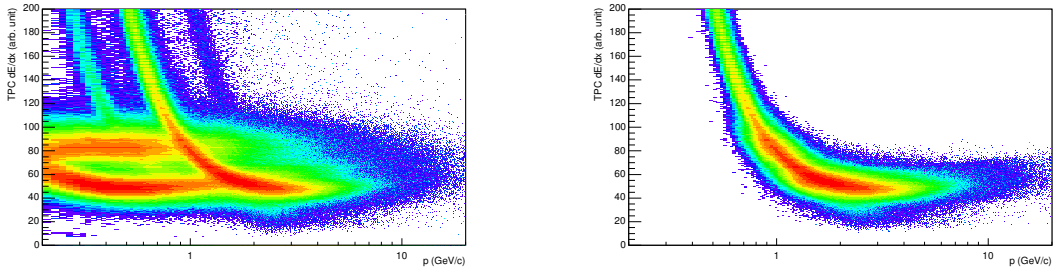


Figure 28: TPC dE/dx as function of transverse momentum for total (top) and selected proton in 3σ (bottom)

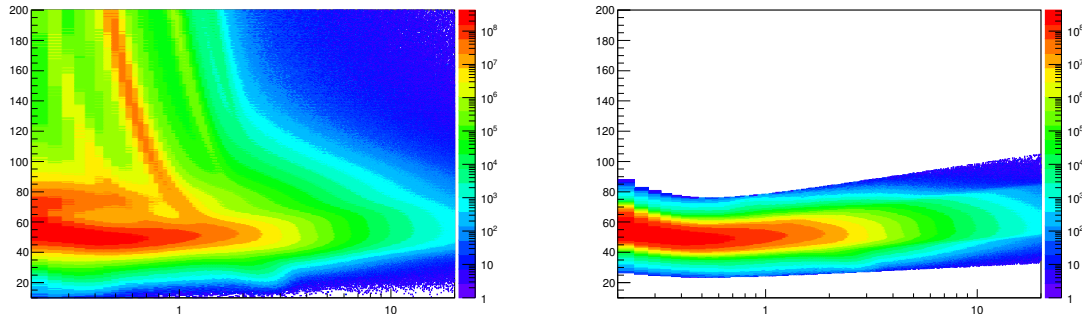


Figure 29: TPC dE/dx as function of transverse momentum for total (top) and selected first emitted π in 3σ (bottom)

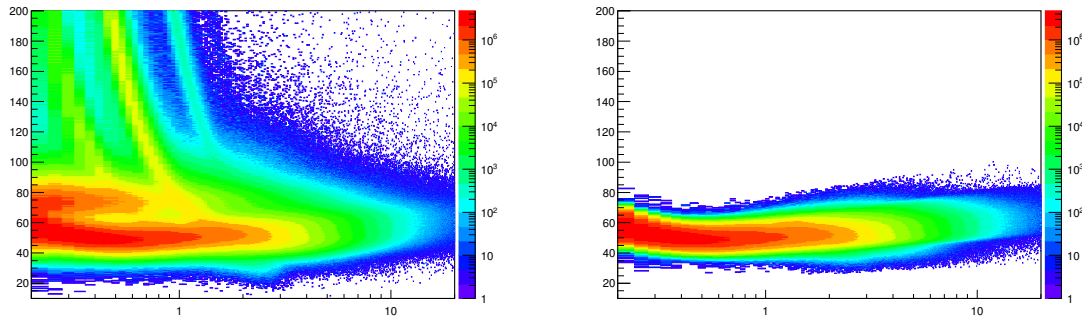


Figure 30: TPC dE/dx as function of transverse momentum for total (top) and selected second emitted π in 3σ (bottom)

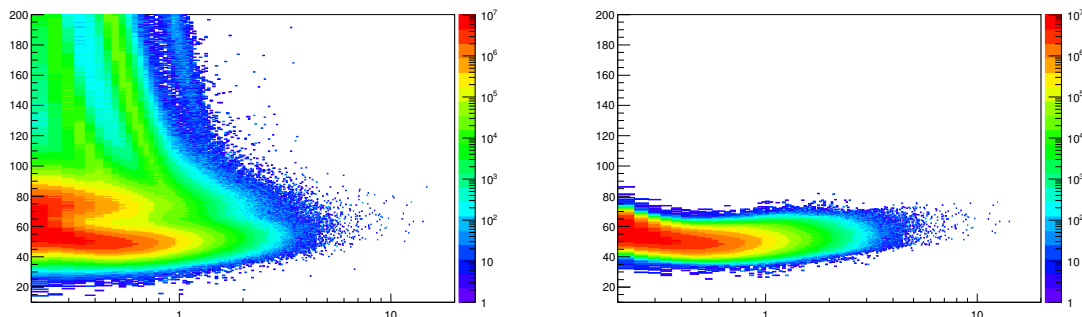


Figure 31: TPC dE/dx as function of transverse momentum for total (top) and selected last emitted π in 3σ (bottom)

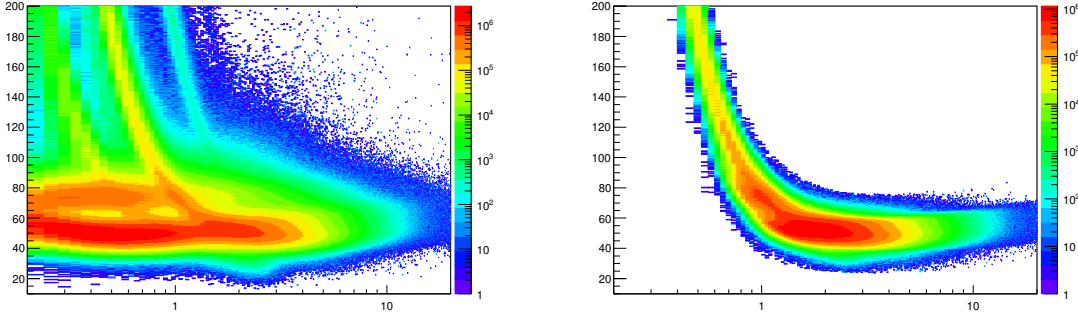


Figure 32: TPC dE/dx as function of transverse momentum for total (top) and selected proton in 3σ (bottom)

1055 **5.1.4 Signal extraction**

1056 The Ξ^{*0} signals were reconstructed by invariant-mass analysis of candidates for the decay
 1057 products in each transverse momentum interval of the resonance particle, and for each
 1058 multiplicity class. The $\Xi^-\pi^+(\Xi^+\pi^-)$ invariant mass distribution is reported in Figure 5.1.4
 1059 for semi-central events (20-40%) in p-Pb collisions and Figure 5.1.4 for central events(0-
 1060 10%) in Pb-Pb collisions.

1061 Since the resonance decay products originate from a position which is indistinguishable
 1062 from the PV, a significant combinatorial background is present. In order to extract
 1063 $\Xi(1530)^0$ signal it is necessary to remove or, at least reduce, the combinatorial background.
 1064 For this analysis, this has been done with the event mixing (EM) technique, by combining
 1065 uncorrelated decay products 20 different events in p-Pb (5 different events in Pb-Pb). The
 1066 events for the mixing have been selected by applying the similarity criteria to minimise
 1067 distortions due to different acceptances and to ensure a similar event structure, only tracks
 1068 from events with similar vertex positions z ($|\Delta z| < 1$ cm) and track multiplicities n ($|\Delta n| <$
 1069 10) were taken.

1070 The mixed-event background distributions were normalised to two fixed regions,
 1071 $1.49 < M_{\Xi\pi} < 1.51$ GeV/c^2 and $1.56 < M_{\Xi\pi} < 1.58$ GeV/c^2 , around the Ξ^{*0} mass
 1072 peak (Figure 5.1.4 and 5.1.4). These regions were used for all p_T intervals and multiplicity
 1073 classes, because the background shape is reasonably well reproduced in these regions and
 1074 the invariant-mass resolution of the reconstructed peaks appears stable, independently of
 1075 p_T . The uncertainty on the normalisation was estimated by varying the normalisation
 1076 regions and is included in the quoted systematic uncertainty for the signal extraction (Section 5.4).

1077 After the background subtraction, the resulting distribution is shown in Figure 5.1.4
 1078 and 5.1.4. In order to obtain raw yields, a combined fit of a first-order polynomial for

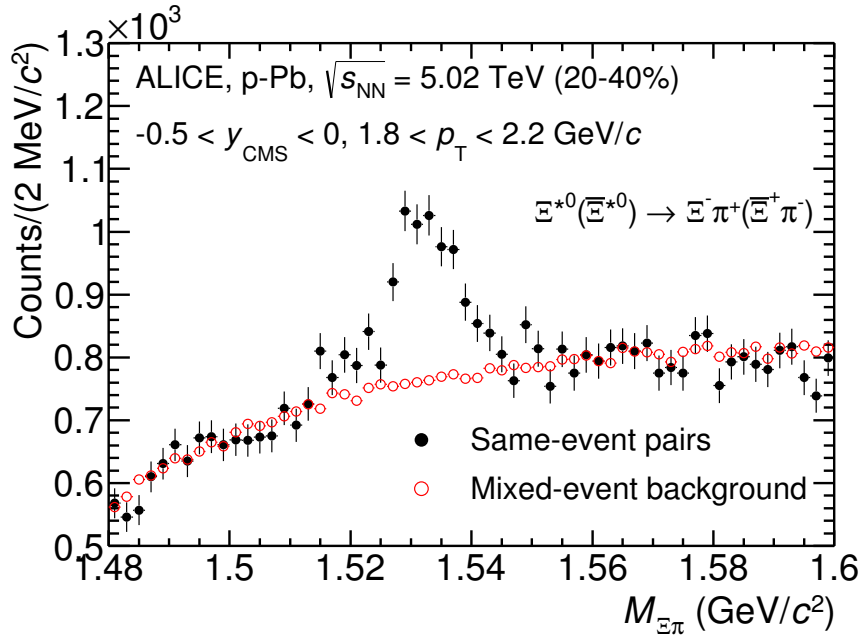
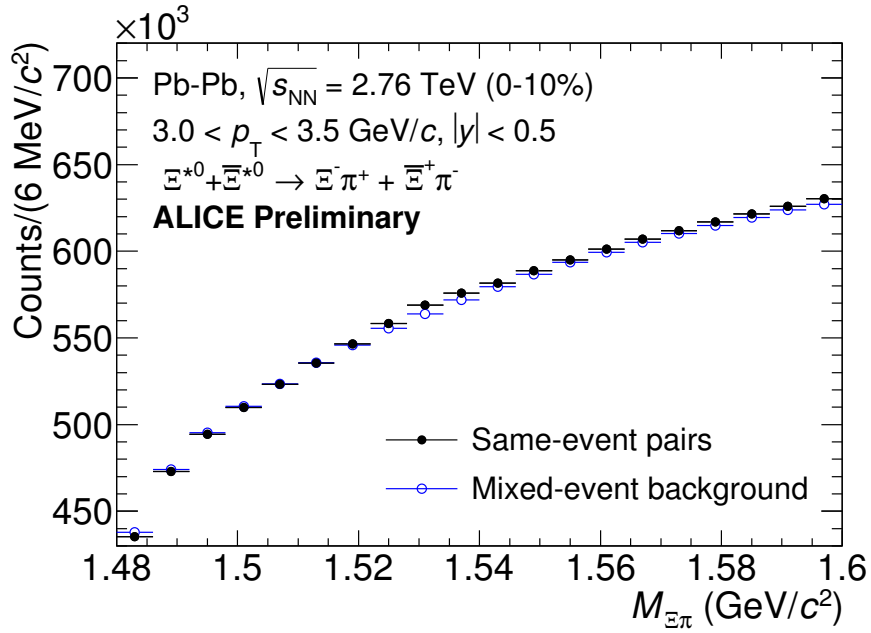


Figure 33: The $\Xi^\pm\pi^\pm$ invariant mass distribution (Same-event pairs) in $1.8 < p_T < 2.2$ GeV/c and for the multiplicity class 20-40%. The background shape, using pairs from different events (Mixed-event background), is normalised to the counts in $1.49 < M_{\Xi\pi} < 1.51$ GeV/c 2 and $1.56 < M_{\Xi\pi} < 1.58$ GeV/c 2 .



1080 the residual background and a Voigtian function (a convolution of a Breit-Wigner and a
 1081 Gaussian function accounting for the detector resolution) for the signal was used. The
 1082 mathematical form of fit function used in analysis is:

$$f(M_{\Xi\pi}) = \frac{Y}{2\pi} \frac{\Gamma_0}{(M_{\Xi\pi} - M_0)^2 + \frac{\Gamma_0^2}{4}} \frac{e^{-(M_{\Xi\pi} - M_0)/2\sigma^2}}{\sigma\sqrt{2\pi}} + bg(M_{\Xi\pi}) \quad (7)$$

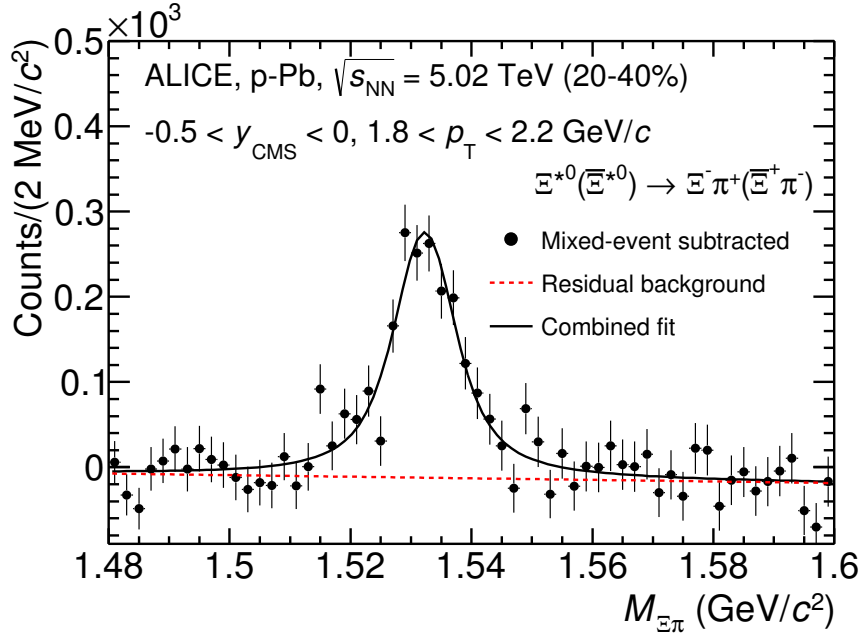


Figure 35: The invariant mass distribution after subtraction of the mixed-event background in p–Pb collisions. The solid curve represents the combined fit, while the dashed line describes the residual background.

1083 The mass parameter of the Voigtian fit (M_0) is left free within the fit range ($1.48 \text{ GeV}/c^2$
 1084 and $1.59 \text{ GeV}/c^2$). The overall invariant mass width of the Voigtian function is governed
 1085 by 2 parameters: σ and Γ_0 . The σ describes the broadening of the peak due to finite
 1086 detector resolution while Γ describes the intrinsic width of the resonance itself. The Γ_0 is
 1087 fixed to the PDG value of $9.1 \text{ MeV}/c$ for the $\Xi(1530)^0$. Because of lack of statistics, the
 1088 σ can be overestimated. Therefore the σ parameter is fixed to value derived from σ in
 1089 MB events which has largest statistics. The σ as function of p_T distribution in MB events
 1090 is shown in Figure. 37 and we also report invariant mass of $\Xi(1530)^0$ as function of p_T in
 1091 Figure. 38. The $\Xi(1530)^0$ raw yields have been extracted from the fit for the 4 multiplicity

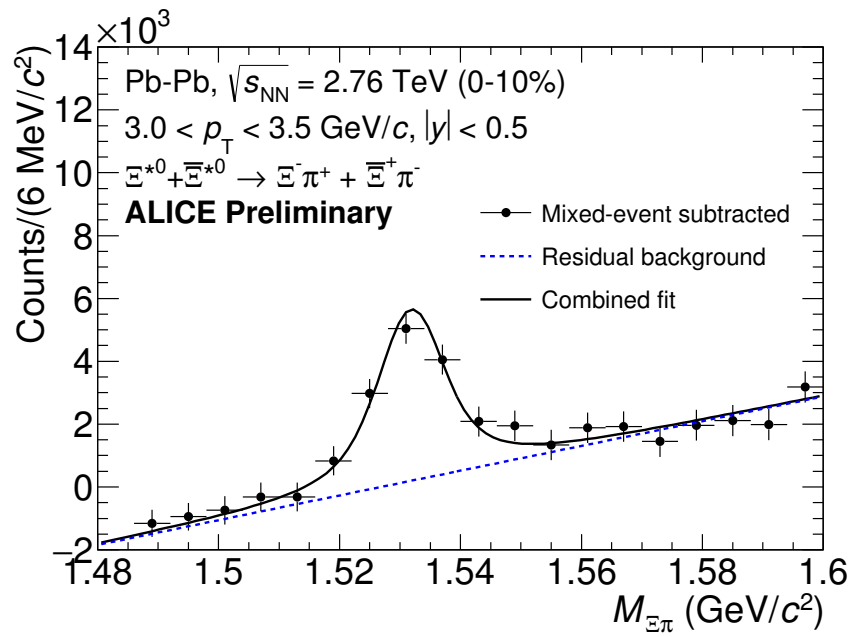


Figure 36: The invariant mass distribution after subtraction of the mixed-event background in Pb–Pb collisions. The solid curve represents the combined fit, while the dashed line describes the residual background.

¹⁰⁹² bins (+ NSD events) in p–Pb and 4 centrality bins in Pb–Pb collisions and the yields as
¹⁰⁹³ function of p_T are shown in Figure 39.

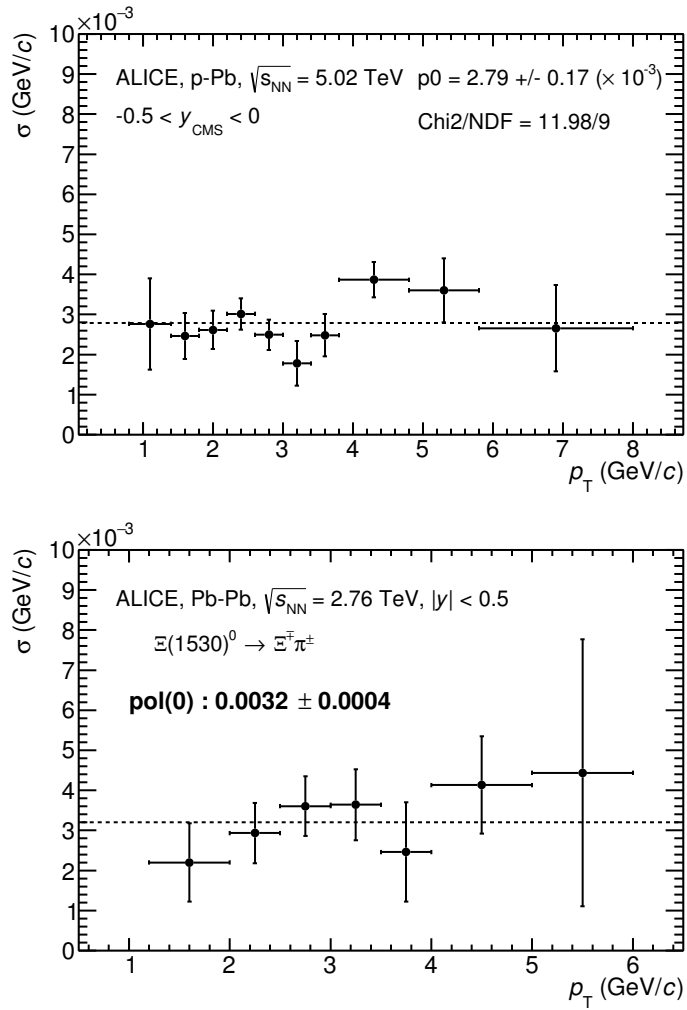


Figure 37: σ fit parameters as a function of p_T in MB in p-Pb collisions (top) and in Pb-Pb collisions (bottom).

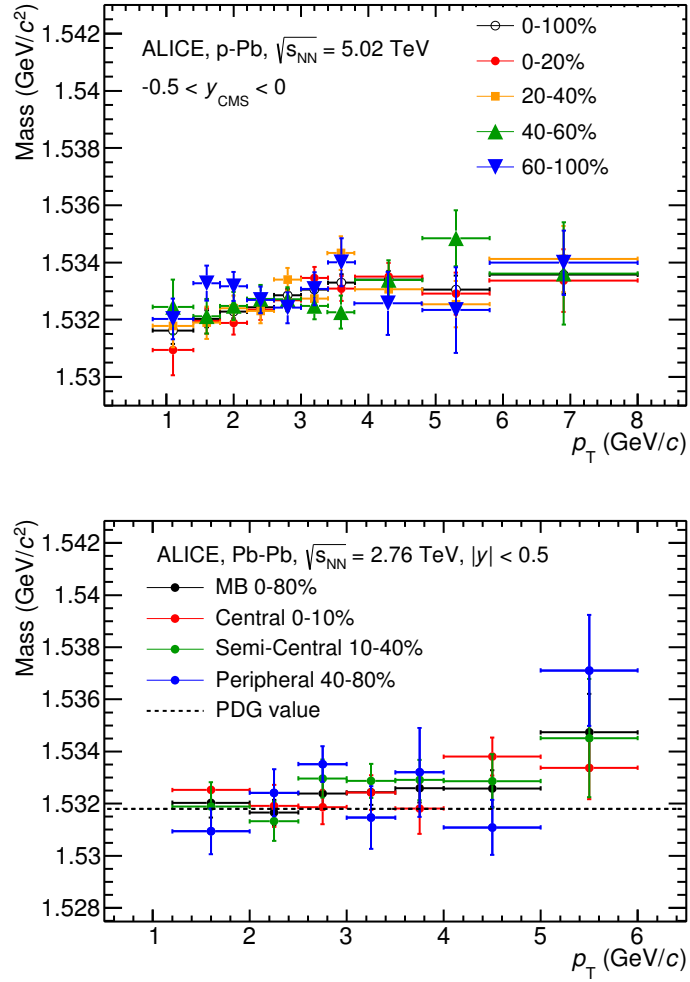


Figure 38: $\Xi(1530)^0$ -mass obtained from fit of the Voigtian peak as a function of p_T in each multiplicity classes in p-Pb collisions (top) and the different centrality classes in Pb-Pb (bottom).

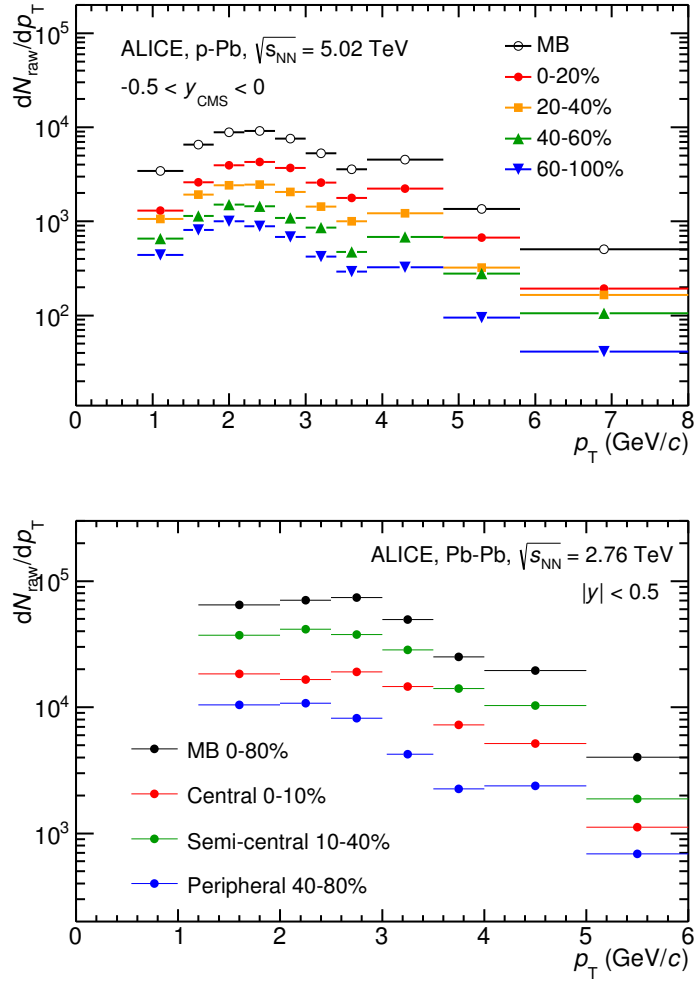


Figure 39: $\Xi(1530)^0$ -raw spectra obtained from fit of the Voigtian peak and a polynomial residual background for different multiplicities in p-Pb collisions (top) and Pb-Pb collisions (bottom). Only the statistical error is reported.

1094 **5.2 Efficiency correction**

1095 The raw yields were corrected for the geometrical acceptance and the reconstruction effi-
 1096 ciency ($A \times \epsilon$) of the detector (Figure. 40). By using the DPMJET 3.05 event generator [46]
 1097 and the GEANT 3.21 package [47], a sample of about 100 million p–Pb events was sim-
 1098 ulated and reconstructed in order to compute the corrections. The distributions of $A \times \epsilon$
 1099 were obtained from the ratio between the number of reconstructed Ξ^{*0} and the number of
 1100 generated particle in the same p_T and rapidity interval. Since the correction factors for
 1101 different multiplicity classes are in agreement with those from MB events within statistical
 1102 uncertainty, the latter were used for all multiplicity classes.

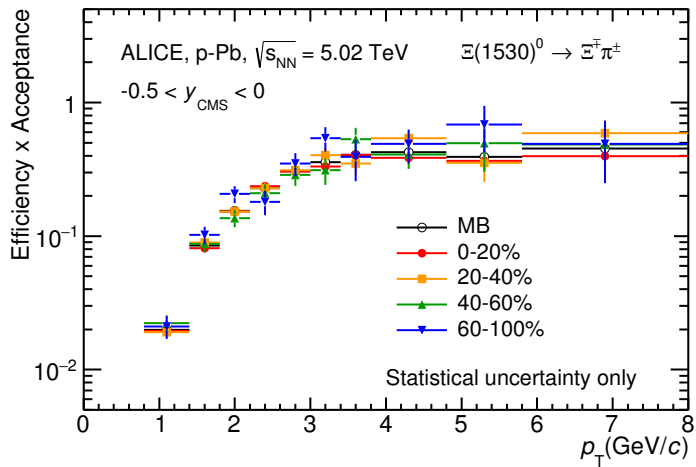


Figure 40: $\Xi(1530)^0$ -raw spectra obtained from fit of the Voigtian peak and a polynomial residual background for different multiplicities. Only the statistical error is reported.

1103 Because the generated $\Xi(1530)^0$ spectra have different shapes than the measured $\Xi(1530)^0$
 1104 spectra, it is necessary to weight the generated and reconstructed $\Xi(1530)^0$ spectra in these
 1105 simulations. Fig. 41 shows the generated and reconstructed $\Xi(1530)^0$ spectra plotted with
 1106 the (corrected) measured $\Xi(1530)^0$ spectrum for MB events and the Levy fit of that mea-
 1107 sured spectrum. The generated and measured $\Xi(1530)^0$ spectra have different behaviours
 1108 for the range $0.5 < p_T < 1$ GeV/c. The generated $\Xi(1530)^0$ spectrum decreases with
 1109 increasing p_T over this range, while the fit of the measured $\Xi(1530)^0$ spectrum reaches a
 1110 local maximum in this range. The correction ϵ is observed to change rapidly over this
 1111 p_T range. It is therefore necessary to weight the generated spectrum so that it has the
 1112 shape of the measured $\Xi(1530)^0$ spectrum (and to apply corresponding weights to the re-
 1113 constructed $\Xi(1530)^0$ spectrum). An iterative procedure is performed to determine the
 1114 correct weighting (and therefore the correct ϵ).

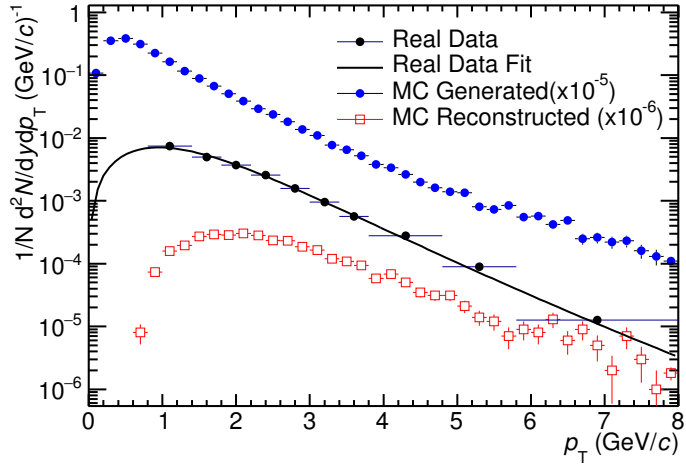


Figure 41: Real corrected $\Xi(1530)^0$ spectrum (black) for the minimum bias with Levy fit (black curve). Also shown are the unweighted generated (blue) and reconstructed (red) $\Xi(1530)^0$ spectra.

- 1115 1. The unweighted ϵ is calculated.
- 1116 2. This ϵ is used to correct the measured xis spectrum.
- 1117 3. The corrected $\Xi(1530)^0$ spectrum is fit.
- 1118 4. This fit is used to weight the simulated xis spectra. A p_T dependent weight is applied
1119 to the generated xis spectrum so that it follows the fit. The same weight is applied
1120 to the reconstructed xis spectrum.
- 1121 5. The (weighted) ϵ is calculated.
- 1122 6. Steps 2-5 are repeated (with the weighted ϵ from step 5 used as the input for step 2)
1123 until the ϵ values are observed to change by $< 0.1\%$ (relative) between iterations. It
1124 is observed that four iterations are sufficient for this procedure to converge.

1125 Finally, the re-weighted efficiency is obtained and the distribution as function of p_T is
1126 shown in Figure 42.

1127 In order to obtain the correction factor dedicated in Pb-Pb collisions, MC events are
1128 generated using Heavy Ion Jet Interaction Generator (HIJING). The generated events are
1129 passed through a GEANT3 model of the ALICE experiment with a realistic description of
1130 the detector response. Because we have observed centrality dependent efficiency, the cen-
trality dependent efficiencies have been applied to get corrected raw yield. The reweighting

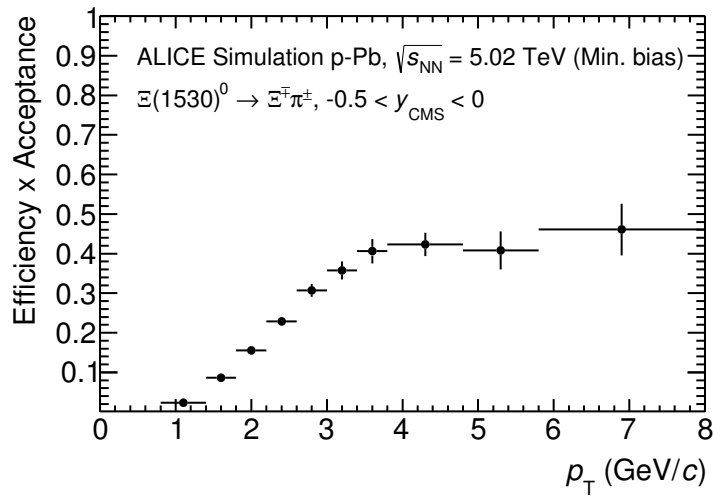


Figure 42: Efficiency as a function of p_T in minimum bias events in p-Pb collisions.

1132 approach which was used to correct the efficiency in p-Pb is also applied to the efficiency
 1133 obtained in Pb-Pb.

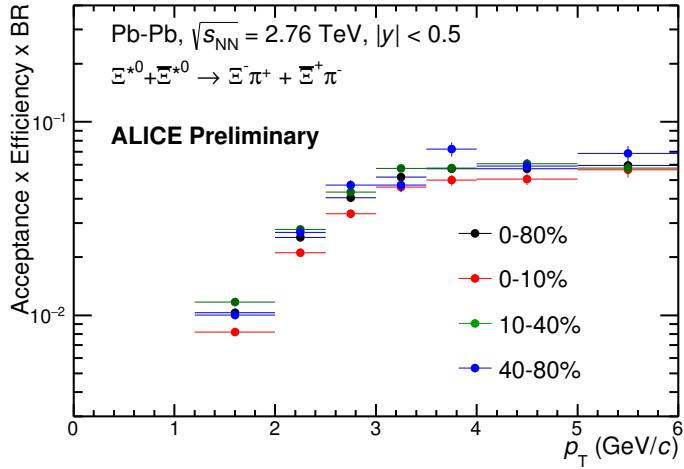


Figure 43: Efficiency as a function of p_T in different centrality classes in Pb–Pb collisions

1134 **5.3 Corrected p_T -spectra**

1135 The p_T spectrum is by the number of produced particles of a given type in the desired
 1136 interval of phase-space divided by the number of inelastic collisions. The spectrum is
 1137 calculated as:

$$\frac{1}{N} \times \frac{d^2N}{dydp_T} = \frac{1}{N_{E,PhysSel}} \times \frac{N_{raw}}{dp_T dy} \frac{1}{\epsilon} \frac{N_{total}^{MC}}{N_{post-PVcut}^{MC}}, \quad (8)$$

1138 where N_E represent the number inelastic collisions, the $\frac{dN}{dydp_T}$ is the yield per range of
 1139 rapidity y , per range in p_T . On the right hand side $N_{E,PhysSel}$ is the number of events
 1140 counted by the physics selection trigger. N_{raw} is the raw extracted number of particle in the
 1141 rapidity and p_T bin of width $\Delta y = 0.5$ in p–Pb ($\Delta y = 1.0$ in Pb–Pb) and Δp_T , respectively.
 1142 ϵ is the reconstruction efficiency estimated from Monte Carlo simulations. $\frac{N_{total}^{MC}}{N_{post-PVcut}^{MC}}$ is the
 1143 ratio of the total number of particle from MC divided by the number of particle from MC
 1144 after the Primary-Vertex cut is imposed. It takes into account the fraction of particle lost
 1145 after imposing the PV cut. We notice that for minimum-bias results in p–Pb, we adopted
 1146 a normalisation such that to provide result from non-single diffractive(NSD) cross-section.
 1147 The normalisation factor is 0.964 [5]. The obtained spectrum at MB and the spectrums
 1148 from different multiplicity classes in p–Pb are shown in Figure 44 and different centrality
 1149 classes in Pb–Pb are shown in Figure 45.

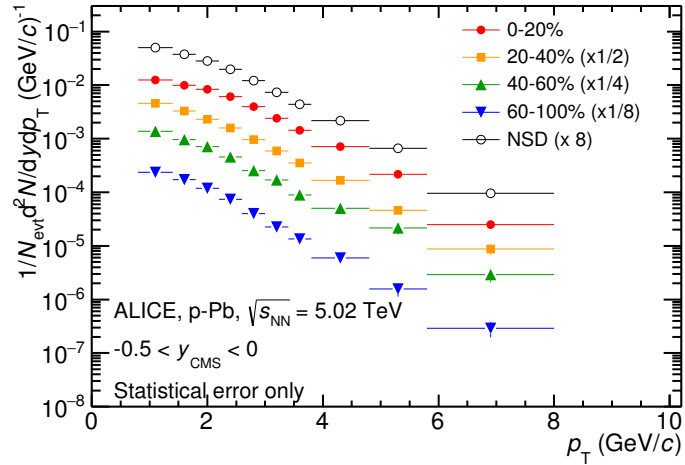


Figure 44: Corrected p_T -spectra of $\Xi(1530)^0$ in NSD and different multiplicity classes in p-Pb collisions.

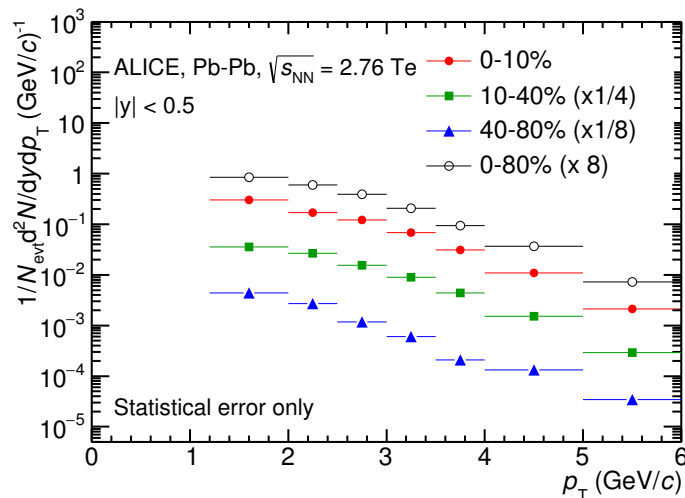


Figure 45: Corrected p_T -spectra of $\Xi(1530)^0$ in different centrality classes in Pb-Pb collisions.

1150 **5.4 Systematic uncertainties**

1151 The systematic uncertainties are calculated in seven principle groups. The procedure to ob-
1152 tain the systematic uncertainties is performed many times by varying the possible permuta-
1153 tion of the analysis parameter. The general strategy for evaluating systematic uncertainties
1154 is described as following:

- 1155 1. Choose one set of parameters for the analysis as default
- 1156 2. Observe the deviation of yield when one parameter is changed
- 1157 3. The systematic uncertainty is calculated for a given source as the RMS deviation of
1158 the available sources.
- 1159 4. The total systematic uncertainty, taking into account all the different sources, is the
1160 sum in quadrature of each source.

1161 To study the systematic effect we repeat the measurement by varying one parameter at
1162 a time. A Barlow [48] check has been performed for each measurement to verify whether it
1163 is due to a systematic effect or a statistical fluctuation. Let each measurement be indicated
1164 by $(y_i \pm \sigma_i)$ and the central value (default measurement) by $(y_c \pm \sigma_c)$, one can define $\Delta\sigma_i$
1165 (Eq. 9).

$$\Delta\sigma_i = \sqrt{(\sigma_i^2 - \sigma_c^2)} \quad (9)$$

1166 Then we calculate $n_i = \Delta y_i / \Delta\sigma_i$, where $\Delta y_i = |y_c - y_i|$. If $n_i \leq 1.0$ then the effects
1167 are due to the statistical fluctuation and if $n_i > 1.0$ we apply consistency check. Since
1168 the alternate and default measurements are not statistically independent, an alternate
1169 measurement which is statistically consistent with the default measurement should not be
1170 used in calculating a systematic uncertainty. The difference between the two measurements
1171 is $\Delta = y_c - y_i$. The difference in quadrature of the uncertainties is calculated by Eq. 9. It
1172 could be possible to check if $\Delta < \sigma$ and exclude such cases from the systematic uncertainties.
1173 However, there can be statistical fluctuations for which $\Delta > \sigma$. If the variations between the
1174 default and alternate measurements are purely statistical, the distribution of Δ/σ should
1175 be a Gaussian with a mean value that is consistent with zero and a deviation σ consistent
1176 with unity. In this analysis, if the mean value is less than 0.1 and σ is less than 1, the
1177 variation passes the consistency check.

1178 Only the measurements which passed the Barlow check ($n_i > 1$) are used to determine
1179 the systematic uncertainty. For measurements $N > 2$, the systematic uncertainty has been
1180 determined as the RMS (eqn. 10) of the available measurements. If $N=2$, the absolute
1181 difference is assigned as systematic uncertainty.

$$\delta y_{syst.} = \sqrt{\frac{1}{N} \sum_i (y_i - \bar{y})^2} \quad (10)$$

1182 Here N is the total number of available measurements including y_c and \bar{y} is the average
1183 of value of the measurements. The measurement did not pass Barlow check, zero systematic
1184 uncertainty has been assigned to the value.

1185 By suing the way as explained above, all the main contributions to the systematic un-
1186 certainty of particle spectra have been studied. In particular those that comes from signal
1187 extraction, topological and kinematical selection cuts, track quality selection and $n\sigma$ TPC
1188 PID variation. the meaning of each source of systematic uncertainty studied is described
1189 in the following:

1190

1191 **Signal extraction**

1192 We have extracted the signal with varying the yield calculating method which contains
1193 the method of signal extraction by integrating the Voigtian fit function and bin counting.
1194 We also have varied the normalisation range which is related to the invariant mass region
1195 where the mixed events distribution is scaled to subtract the combinatorial background
1196 and different background estimator such as Like-Sign distribution and polynomial fit was
1197 taken account into the systematic source of signal extraction. The systematic uncertainty
1198 from signal extraction is sum in quadrature of three sources.

1199

1200 **Topological selection**

1201 To evaluate the stability of the chosen set of values for the topological cuts, loose and tight
1202 cuts have beed defined in order to vary by $\pm 10\%$ respectively. The parameters are changed
1203 once at a time. Total systematic uncertainty from topological selection is calculated by
1204 summation in quadrature of nine sources.

1205

1206 **TPC $N_{cluster}$ selection**

1207 The selection performed for the daughter tracks of the cascade is that $N_{cluster}$ is larger
1208 than 70 and the value has been varied to 60 and 80 in order to estimate the systematic
1209 uncertainty due to this selection.

1210

1211 **TPC dE/dx selection**

1212 In order to evaluate any potential effect due to the TPC dE/dx selection (U_{PID}), the N_σ
1213 selection was varied with $N = 2.5$ and 3.5 .

1214

1215 **p_T shape correction**

1216 As described in Section 5.2, due to the different shape of the measured and generated
1217 $\Xi(1530)^0$ spectra, we have applied reweighing procedure to the generated spectra to have
1218 same shape and this correction is added into contributor of systematic uncertainty as
1219 p_T shape correction.

1220

1221 **Mass window range selection**

1222 In order to select Ξ^\pm which is daughter particle of $\Xi(1530)^0$, we apply the mass window

1223 ± 7 MeV/ c^2 around $\Xi(1530)^0$ mass on $\Lambda\pi$ invariant mass distribution. The boundaries
1224 has been varied to ± 6 MeV/ c^2 and ± 8 MeV/ c^2 to estimate systematic uncertainty.

1225

1226 **Vertex range selection**

1227 The distribution of vertex-z is shown in Fig.21. The cut on $|Vz|$ was varied from the nominal
1228 ± 10 cm to ± 9 cm, ± 11 cm.

1229

1230 **Material Budget and hadronic cross section**

1231 A possible source of uncertainty comes from the description of the material, active (detecting area)
1232 or dead (structure and cable), that the particles cross during their travel in
1233 the MC with respect to the real material present in the detector. Such description could
1234 affect the reconstruction efficiency in different aspects (e.g. multiple scattering, energy
1235 loss). The value estimated by Ξ analysis [23] has been used in this study which gives 4%
1236 systematic uncertainty. In case of systematic uncertainty from hadronic cross section, we
1237 have inherited the value studied in previous measurement[49] which amount is 1%.

1238

1239 **Tracking efficiency**

1240 Systematic uncertainties from tracking efficiency from ITS + TPC combined track were
1241 assigned as 3% in p–Pb and 4% in Pb–Pb collision system.[49]
1242 (<https://twiki.cern.ch/twiki/bin/view/ALICE/TrackingEfficiencyCharged>)

1243

1244 Finally, total systematic uncertainty is sum in quadrature of sources listed above. Figure
1245 46 and Figure 47 show the total systematic uncertainty in minimum bias event and
1246 different multiplicity classes in p–Pb collisions, respectively. Again, Figure 48 and Figure
1247 49 present the total systematic uncertainty in minimum bias event and different centrality
1248 classes in Pb–Pb collisions.

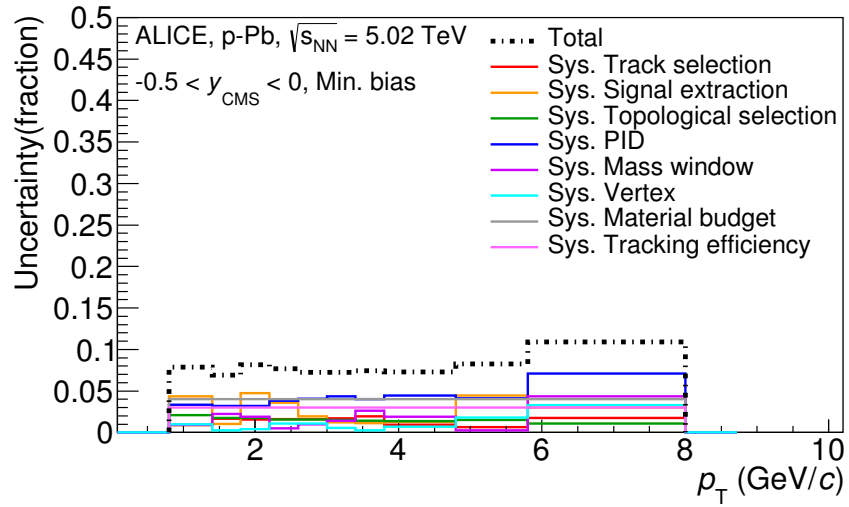


Figure 46: Summary of the contributions to the systematic uncertainty in minimum bias events in p–Pb collisions. The dashed black line is the sum in quadrature of all the contributions.

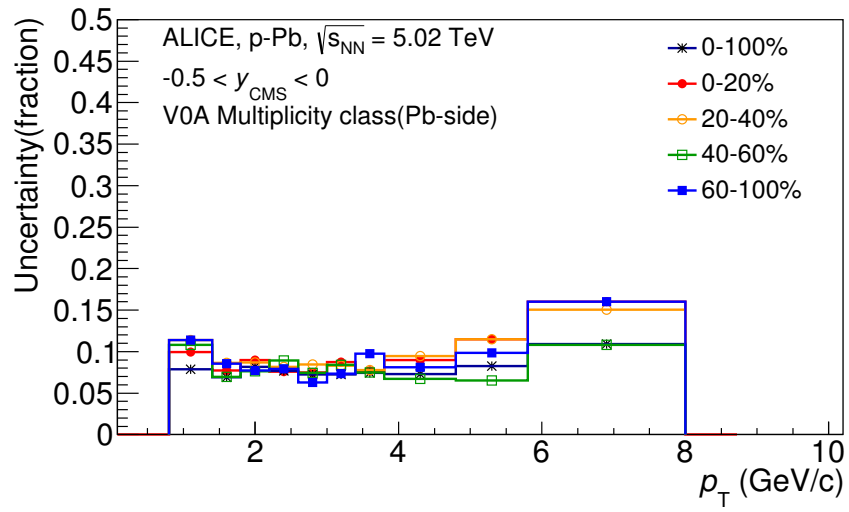


Figure 47: Systematic uncertainties for each multiplicity classes in p–Pb collisions.

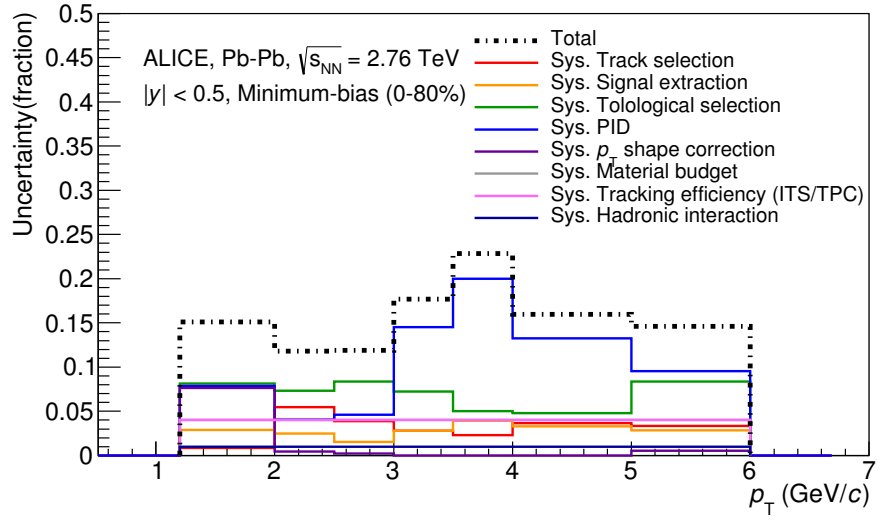


Figure 48: Summary of the contributions to the systematic uncertainty in minimum bias events in Pb–Pb collisions. The dashed black line is the sum in quadrature of all the contributions.

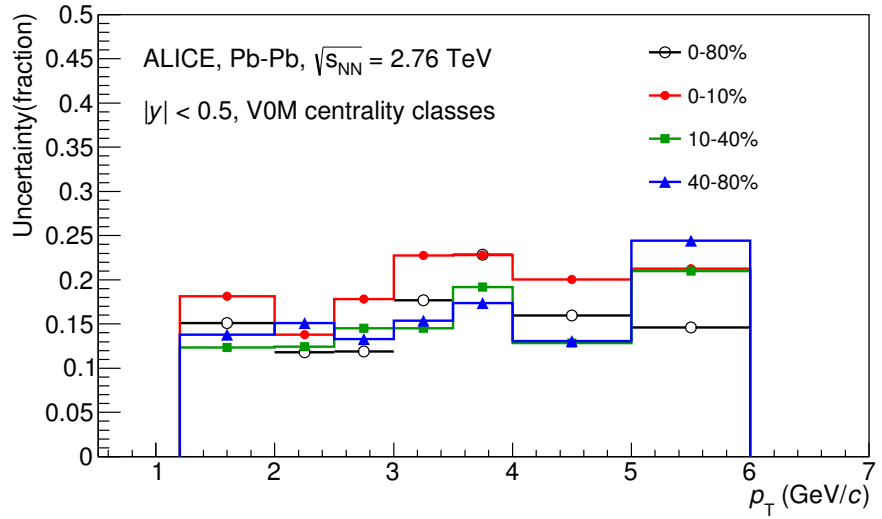


Figure 49: Systematic uncertainties for each multiplicity classes.

Source of uncertainty	p-Pb	Pb-Pb
<i>p</i> _T -dependent		
Tracking efficiency	3%	4%
Tracks selection	1-2%	1-5%
Topological selection	1-2%	5-8%
PID	3-7%	4-20%
Signal extraction	1-5%	1-4%
<i>p</i> _T shape correction	-	0-8%
Mass window (Ξ^\pm)	4%	-
Vertex selection	3%	-
<i>p</i> _T -independent		
Hadronic interaction	-	1%
Material budget	4%	4%
Branching ratio	0.3%	0.3%
Total	8-12%	9-25 %

Table 9: Summary of the systematic uncertainties on the differential yield, $d^2N/(dp_T dy)$. Minimum and maximum values in all p_T intervals and multiplicity classes in p–Pb, centrality classes in Pb–Pb are shown for each source.

1249 **5.5 $\Xi(1530)^0$ transverse momentum spectra**

1250 The raw yield shown in Figure 44 and 45 have been corrected for efficiency as described
 1251 in section 5.2. The measured spectra for $(\Xi(1530)^0 + \bar{\Xi}(1530)^0)/2$ are reported in Figure
 1252 50 for p–Pb collisions and Figure 51 for Pb–Pb collisions. The statistical and systematic
 1253 uncertainties are reported respectively as the error bars and the boxes on the plot. The
 1254 corrected yields for p–Pb collisions are measured with $0.8 < p_T < 8.0$ GeV/c while the
 1255 yields for Pb–Pb collisions are obtained with $1.2 < p_T < 6.0$ GeV/c due to difficulty of
 1256 signal extraction in low and high p_T region.

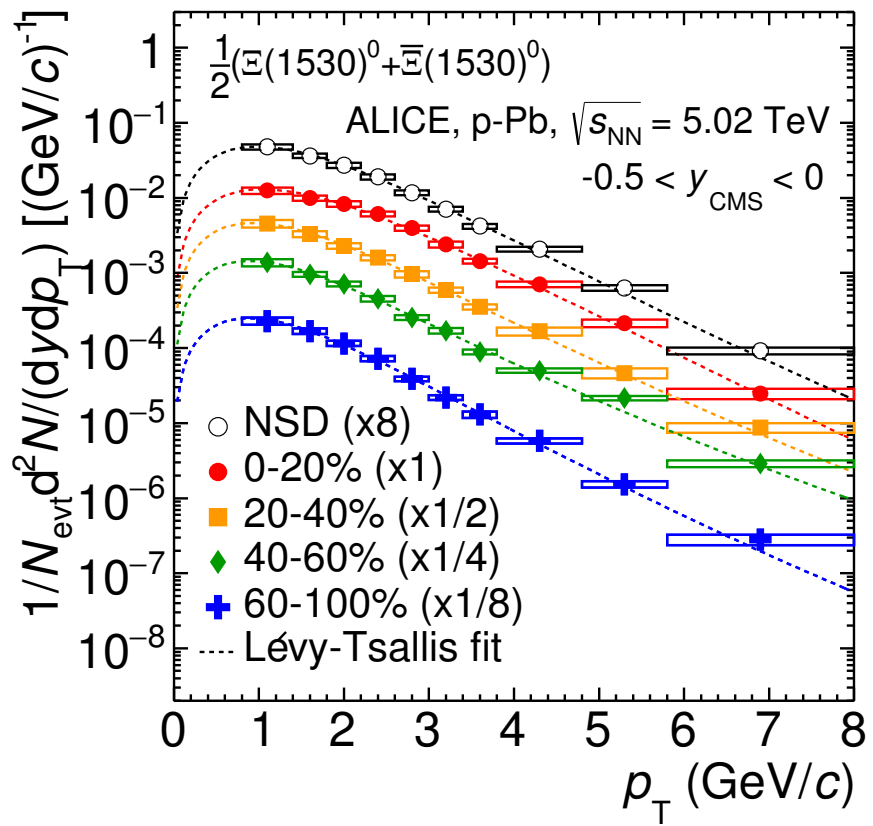


Figure 50: Corrected yields as function of p_T in NSD events and multiplicity dependent event classes in p-Pb collision system. Statistical uncertainties are presented as bar and systematical uncertainties are plotted as boxes.

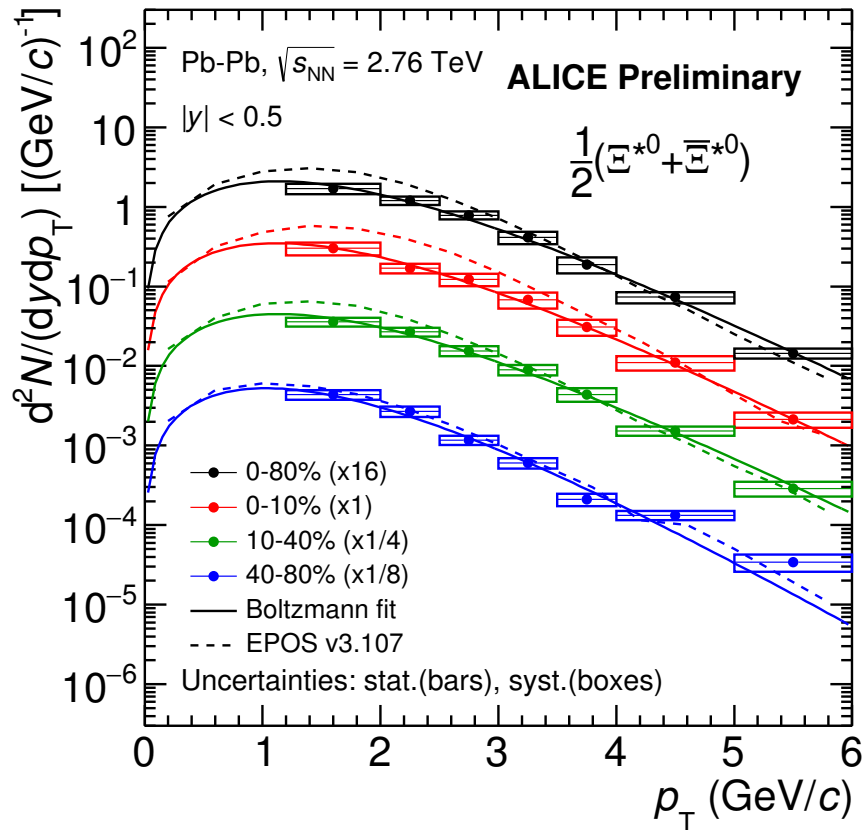


Figure 51: Corrected yields as function of p_T in different centrality classes in Pb–Pb collision system. Statistical uncertainties are presented as bar and systematical uncertainties are plotted as boxes.

1257 6 Further results and discussion

1258 The transverse momentum distributions of double-strange hyperon resonances, $\Xi(1530)^0$
1259 , produced in p–Pb collisions at $\sqrt{s_{\text{NN}}}= 5.02$ TeV and Pb–Pb collisions at $\sqrt{s_{\text{NN}}}= 2.76$
1260 TeV were measured in the mid-rapidity range and they have been already presented in
1261 Chapter 5. From the measurement, the $\langle p_{\text{T}} \rangle$ and integrated particle yield ratios with
1262 system size have been obtained. In the present Chapter these results are compared with
1263 model predictions and discussed in connection with the following topics:

- 1264 • Mean transverse momentum studies
- 1265 • Study of particle production mechanism in hadronic phase
- 1266 • Study of strangeness enhancement

1267 Most of the theoretical aspects related to these topics and, in particular, the description
1268 of the models already have been addressed in Chapter 2.

1269 6.1 Mean transverse momentum

1270 Figure 52 shows the mean transverse momentum $\langle p_{\text{T}} \rangle$ as a function of mean charged-
1271 particle multiplicity density $\langle dN_{\text{ch}}/d\eta_{\text{lab}} \rangle$ at midrapidity. The results for $\Xi(1530)^0$ are
1272 compared with those for other hyperons observed in p–Pb collisions at $\sqrt{s_{\text{NN}}}= 5.02$ TeV [4,
1273 6].

1274 Increasing trends from low to high multiplicities are observed for all hyperons. The
1275 mean transverse momenta increase by 20% as the mean charged-particle multiplicity in-
1276 creases from 7.1 to 35.6. This result is similar to the one obtained for the other hyperons.
1277 Furthermore, a similar increase has been observed also for K^{\pm} , K_S^0 , $K^*(892)^0$ and ϕ [5],
1278 whereas protons are subject to a larger ($\sim 33\%$) increase in the given multiplicity range,
1279 as discussed also in Ref. [4].

1280 In all multiplicity classes, the $\langle p_{\text{T}} \rangle$ follows an approximate mass ordering:

- 1281 • $\langle p_{\text{T}} \rangle_{\Lambda} < \langle p_{\text{T}} \rangle_{\Xi^-} \simeq \langle p_{\text{T}} \rangle_{\Sigma^{*\pm}} < \langle p_{\text{T}} \rangle_{\Xi^{*0}} < \langle p_{\text{T}} \rangle_{\Omega^-}$

1282 The $\langle p_{\text{T}} \rangle$ of $\Sigma^{*\pm}$ looks systematically lower than the $\langle p_{\text{T}} \rangle$ of Ξ^- , despite the larger mass
1283 of $\Sigma^{*\pm}$. The uncertainties, however, are too large to draw any conclusion on possible hints
1284 of violation of the mass hierarchy. This hierarchy of mass-ordering, also including D^0 and
1285 J/ψ in the comparison, is displayed in Figure 53. Note, however, that the D^0 and J/ψ
1286 were measured in different rapidity ranges: $|y_{\text{CMS}}| < 0.5$ [8] ($|y_{\text{CMS}}| < 0.9$ [9]) for D^0 (J/ψ)
1287 in pp and $-0.96 < y_{\text{CMS}} < 0.04$ [8] ($-1.37 < y_{\text{CMS}} < 0.43$ [10]) for D^0 (J/ψ) in p–Pb, and
1288 the results for D^0 and J/ψ in p–Pb collisions are for the 0–100% multiplicity class. This
1289 mass dependence is observed in both p–Pb and pp collisions. It was observed also by the
1290 STAR collaboration [50] in MB pp, MB d–Au and central Au–Au collisions.

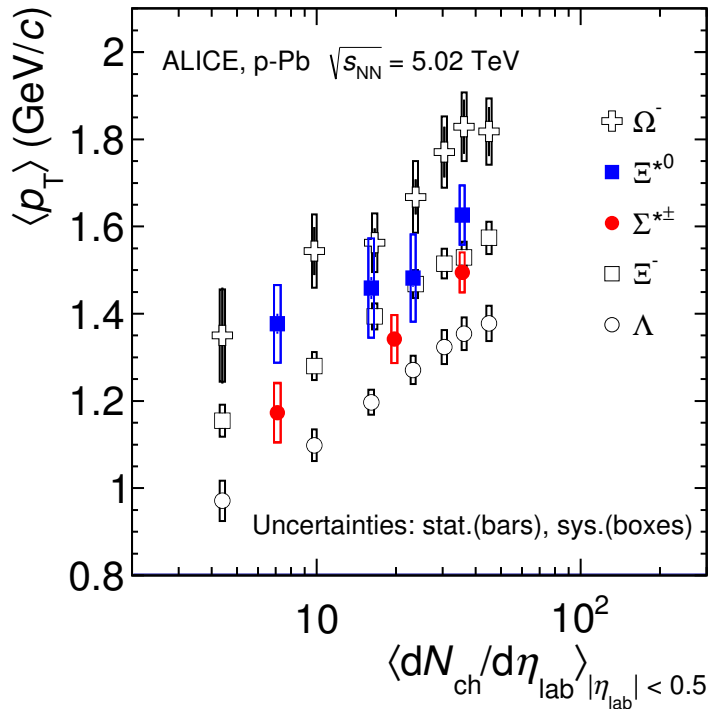


Figure 52: Mean transverse momenta $\langle p_T \rangle$ of Λ , Ξ^- , $\Sigma^{*\pm}$, Ξ^{*0} and Ω^- in p-Pb collisions at $\sqrt{s_{NN}} = 5.02$ TeV as a function of mean charged-particle multiplicity density $\langle dN_{ch}/d\eta_{lab} \rangle$, measured in the pseudorapidity range $|\eta_{lab}| < 0.5$. The results for Λ , Ξ^- and Ω^- are taken from [4, 5, 6]. Statistical and systematic uncertainties are represented as bars and boxes, respectively. The Ω^- and Ξ^- points in the 3rd and 4th lowest multiplicity bins are slightly displaced along the abscissa to avoid superposition with the $\Xi(1530)^0$ points.

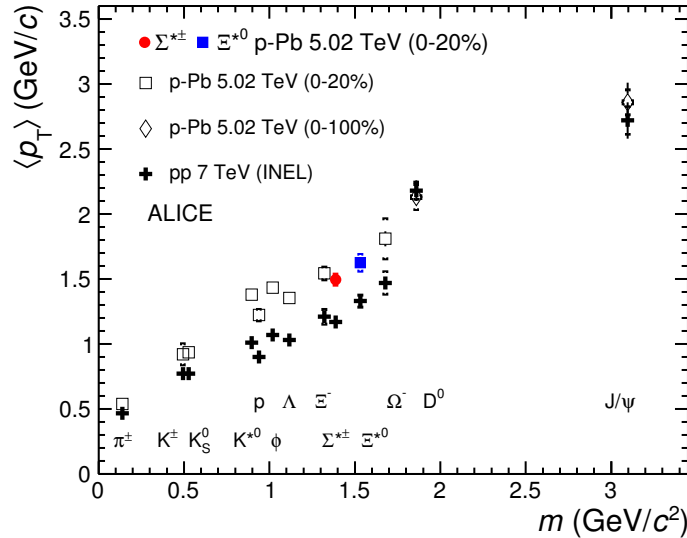


Figure 53: Mass dependence of the mean transverse momenta of identified particles for the 0 – 20% V0A multiplicity class and with $-0.5 < y_{\text{CMS}} < 0$ in p–Pb collisions at $\sqrt{s_{\text{NN}}}=5.02$ TeV [4, 6], and in minimum-bias pp collisions at $\sqrt{s}=7$ TeV [7] with $|y_{\text{CMS}}| < 0.5$. Additionally, D^0 and J/ψ results are plotted. The D^0 and J/ψ were measured in different rapidity ranges: $|y_{\text{CMS}}| < 0.5$ [8] ($|y_{\text{CMS}}| < 0.9$ [9]) for D^0 (J/ψ) in pp and $-0.96 < y_{\text{CMS}} < 0.04$ [8] ($-1.37 < y_{\text{CMS}} < 0.43$ [10]) for D^0 (J/ψ) in p–Pb. Note also that the results for D^0 and J/ψ in p–Pb collisions are for the 0–100% multiplicity class.

1291 Furthermore, for the light-flavour hadrons, the mean transverse momenta in p–Pb col-
1292 lisions are observed to be consistently higher than those in pp collisions at 7 TeV. The
1293 situation for the charm hadrons is different, where $\langle p_T \rangle$ appears compatible between both
1294 colliding systems. The discrepancy is likely due to different production mechanisms for
1295 heavy and light flavours and to a harder fragmentation of charm quarks. Specifically, the
1296 fact that $\langle p_T \rangle$ remains similar in pp and in p–Pb is consistent with an $R_{p\text{Pb}}$ ratio com-
1297 patible with unity at all p_T [8] for D^0 , and/or with the effects of shadowing in p–Pb which
1298 reduces the production at low p_T and thus increasing the overall $\langle p_T \rangle$ for J/ψ [10]; the
1299 small p_T hardening expected in pp when going from 5.02 to 7TeV is apparently not enough
1300 to counter-balance the situation.

1301 Because of small decrease of the $\langle p_T \rangle$ for proton and Λ relative to those for K^{*0} and
1302 ϕ , two different trends for mesons and baryons have been suggested [51]. Even including
1303 D^0 and J/ψ , as shown in Figure 53, a different trend for mesons and baryons cannot be
1304 convincingly established.

1305 **6.2 Particle yield ratios**

1306 **6.2.1 Integrated yield ratios of excited to ground-state hadrons**

1307 The integrated yield ratios of excited to ground-state hyperons [52, 4, 7, 6] with the same
1308 strangeness content, for different collision systems and energies, are shown in Figure 54
1309 as a function of system size. The ratio of $\Xi(1530)^0$ to Ξ is flat across the system and
1310 it complements the information derived from other resonance measurement for different
1311 lifetime which are shown in Figure 55.

1312 The short-lived resonances(ρ , K^* and Λ^*) which exhibit suppression from peripheral to
1313 central lead-lead collisions and with respect to thermal model in central lead-lead collisions.
1314 Currently favored explanation of is dominance of elastic re-scattering of decay daughters
1315 over regeneration in the hadronic phase.

1316 The constant behavior of the yield ratios of excited to ground-state hyperons with same
1317 strangeness content ($\Xi(1530)^0$ and Φ) indicates that neither regeneration nor re-scattering
1318 dominates with increasing collision system size because of its longer-lifetime.

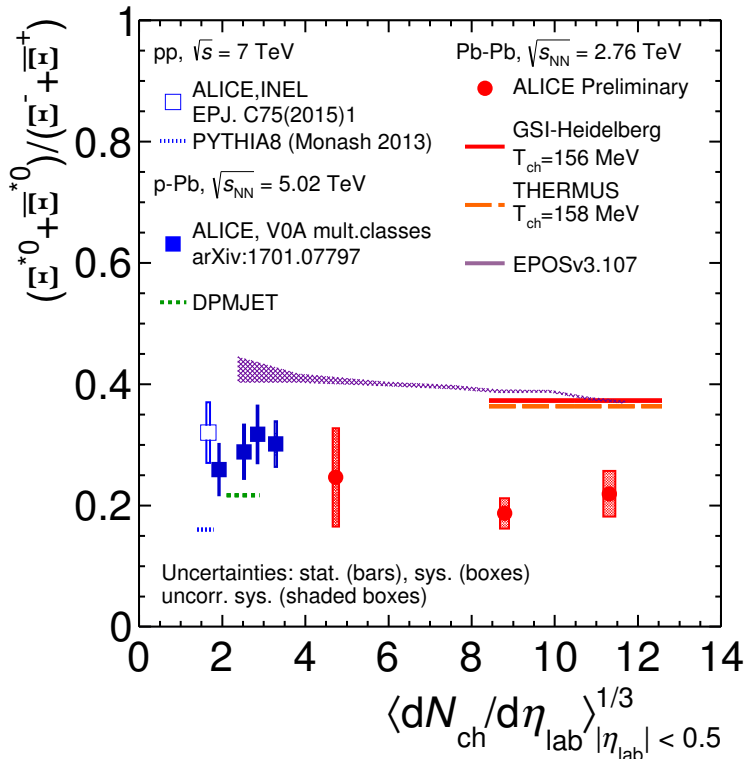


Figure 54: Ratio of $\Xi(1530)^0$ to Ξ^- measured in pp [7], p–Pb [4, 6] and Pb–Pb collisions as a function of $\langle dN_{ch}/d\eta_{lab} \rangle$ measured at midrapidity. Statistical uncertainties (bars) are shown as well as total systematic uncertainties (hollow boxes) and systematic uncertainties uncorrelated across multiplicity (shaded boxes). A few model predictions are also shown as lines at their appropriate abscissa.

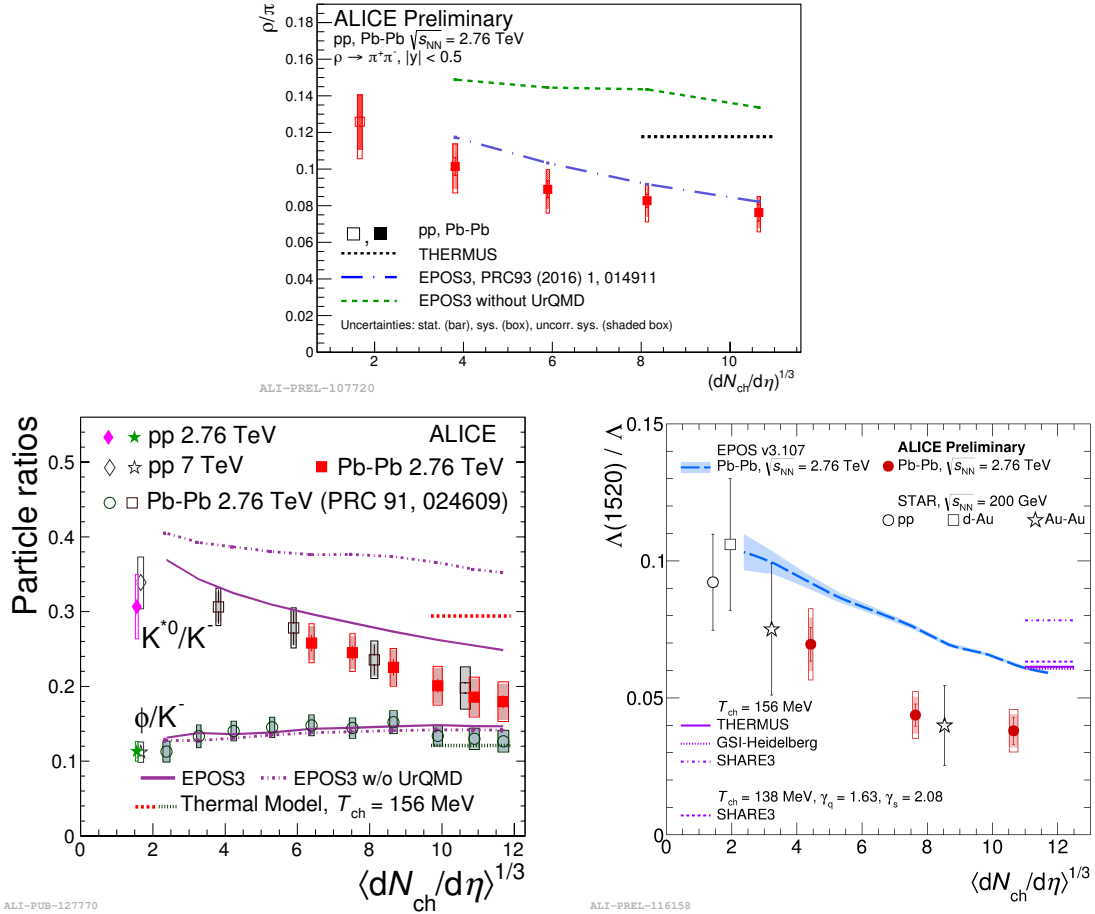


Figure 55: Ratio of ρ/π (Up), K^*/K , ϕ/K (Left bottom) and Λ^*/Λ with system size measured at mid-rapidity. Statistical uncertainties (bars) are shown as well as total systematic uncertainties (hollow boxes) and systematic uncertainties uncorrelated across multiplicity (shaded boxes). A few model predictions are also shown as lines at their appropriate abscissa.

1319 **6.3 Integrated yield ratios to pion**

1320 The integrated yield ratios of excited hyperons to pions are shown in Figure 56 to study
1321 the evolution of relative strangeness production yields with increasing collision system
1322 size. The ratio of $\Xi(1530)^0$ to Ξ is observed to be increase from pp to p–Pb collisions
1323 system and then, decrease from peripheral to central Pb–Pb collision. The QCD-inspired
1324 predictions like PYTHIA for pp [53] and DPMJET for p–Pb [46] clearly underestimate
1325 the observed yield ratios, while the statistical one seems to be comparable with results
1326 from high multiplicity in p–Pb but the ratio in Pb–Pb is below with respect to the model.
1327 The results in pp and p–Pb collisions are consistent with previous observation of ground-
1328 state hyperons to pion ratios. The Figure 57 presents particle yield ratios to pions of
1329 strange and multi-strange hadrons normalized to the values measured in pp collisions. As
1330 shown in the Figure 57, the $\Xi(1530)^0$ to pion ratios follow the trend of Ξ pi as function of
1331 $\langle dN_{ch}/d\eta_{lab} \rangle$ and indicate that the strangeness enhancement observed in p–Pb collisions
1332 depends predominantly on the strangeness content, rather than on the hyperon mass.

1333 The Figure 58 also shows the hyperon-to-pion ratios and compared with model predictions. The
1334

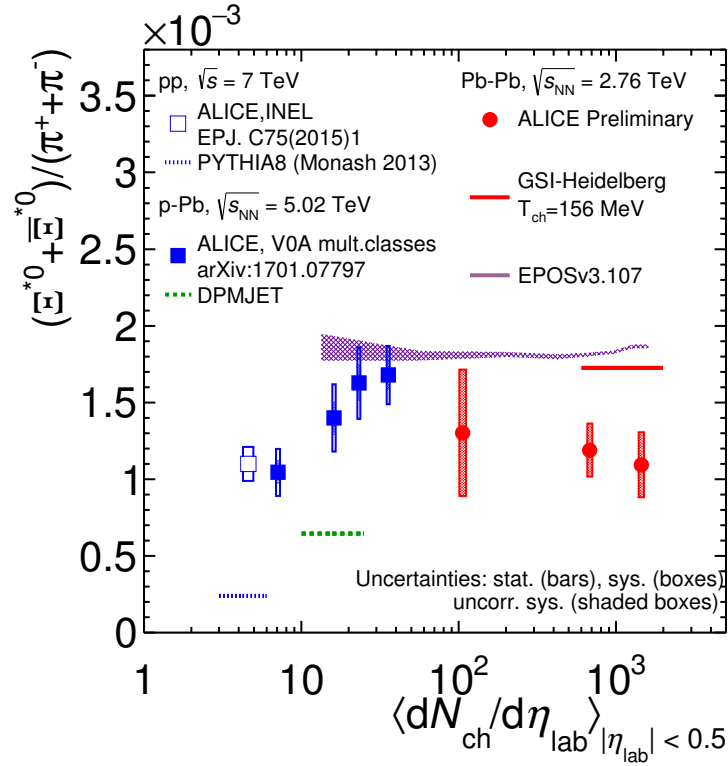


Figure 56: Ratio of $\Xi(1530)^0$ to π^\pm , measured in pp [11] and p–Pb [7] collisions, as a function of the average charged particle density ($\langle dN_{ch}/d\eta_{lab} \rangle$) measured at mid-rapidity. Statistical uncertainties (bars) are shown as well as total systematic uncertainties (hollow boxes) and systematic uncertainties uncorrelated across multiplicity (shaded boxes). A few model predictions are also shown as lines at their appropriate abscissa.

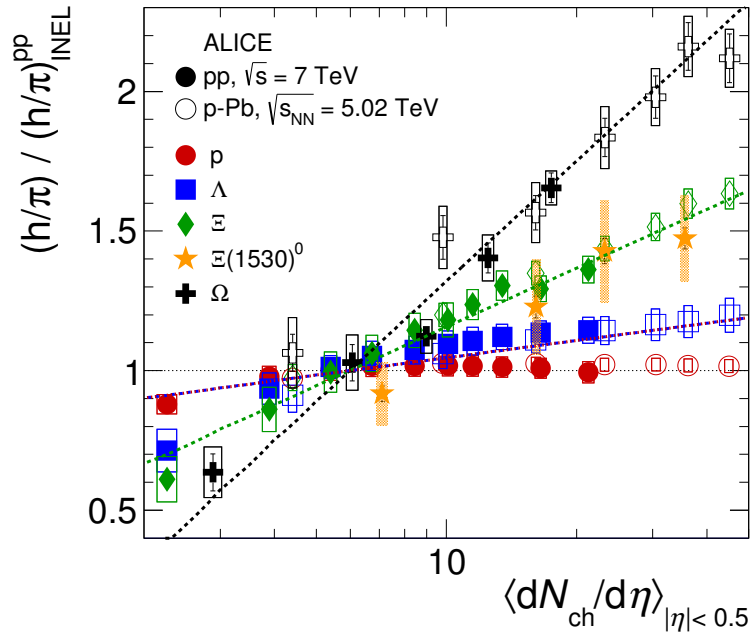


Figure 57: Particle yield ratios to pions of strange and multi-strange hadrons normalized to the values measured in pp collisions, both in pp and in p-Pb collisions. The common systematic uncertainties cancel in the double-ratio. The empty boxes represent the remaining uncorrelated uncertainties. The lines represent a simultaneous fit of the results with the empirical scaling formula in Equation ??.

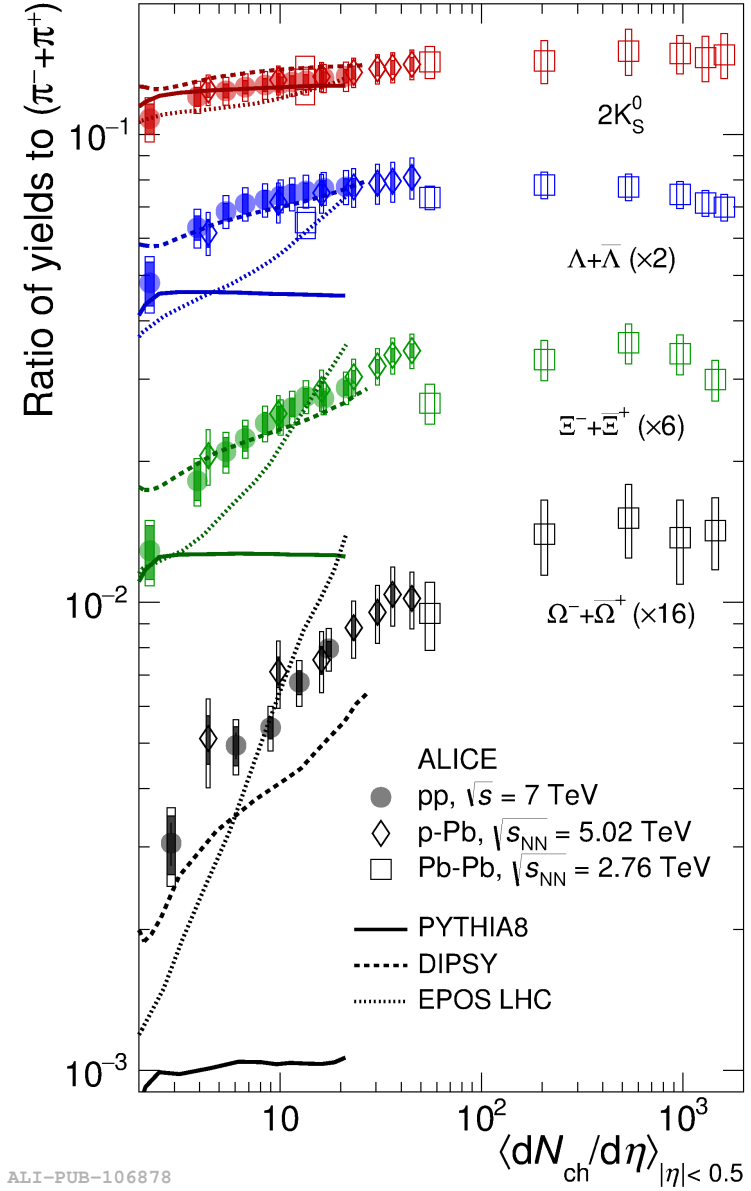


Figure 58: p_T -integrated yield ratios of strange and multi-strange hadrons to $(\pi^+ + \pi^-)$ as a function of $\langle dN_{ch}/d\eta_{lab} \rangle$ measured in the rapidity interval $|\eta| < 0.5$. The empty and dark-shaded boxes show the total systematic uncertainty and the contribution uncorrelated across multiplicity bins, respectively. The values are compared to calculations from MC models and to results obtained in Pb–Pb and p–Pb collisions at the LHC.

1335 References

- 1336 [1] **Particle Data Group** Collaboration, K. Olive *et al.*, “Review of Particle Physics,”
1337 *Chin. Phys. C* **38** (2014) 090001.
- 1338 [2]
- 1339 [3] **ALICE** Collaboration, K. e. a. Aamodt, “Alignment of the ALICE Inner Tracking
1340 System with cosmic-ray tracks,” *JINST* **5** (2010) P03003.
- 1341 [4] **ALICE** Collaboration, J. Adam *et al.*, “Multiplicity dependence of pion, kaon,
1342 proton and lambda production in p–Pb collisions at $\sqrt{s_{\text{NN}}}= 5.02 \text{ TeV}$,” *Phys. Lett.*
1343 **B728** (2014) 25–38, [arXiv:1307.6796 \[nucl-ex\]](https://arxiv.org/abs/1307.6796).
- 1344 [5] **ALICE** Collaboration, J. Adam *et al.*, “Production of $K^*(892)^0$ and $\phi(1020)$ in
1345 p–Pb collisions at $\sqrt{s_{\text{NN}}}= 5.02 \text{ TeV}$,” *Eur. Phys. J. C* **76** (2016) 245,
1346 [arXiv:1601.7868 \[nucl-ex\]](https://arxiv.org/abs/1601.7868).
- 1347 [6] **ALICE** Collaboration, J. Adam *et al.*, “Multi-strange baryon production in p–Pb
1348 collisions at $\sqrt{s_{\text{NN}}}= 5.02 \text{ TeV}$,” *Phys. Lett. B* **758** (2016) 389–401,
1349 [arXiv:1512.07227 \[nucl-ex\]](https://arxiv.org/abs/1512.07227).
- 1350 [7] **ALICE** Collaboration, B. Abelev *et al.*, “Production of $\Sigma(1385)^{\pm}$ and $\Xi(1530)^0$ in
1351 proton-proton collisions at $\sqrt{s}= 7 \text{ TeV}$,” *Eur. Phys. J. C* **75** (2015) 1,
1352 [arXiv:1406.3206 \[nucl-ex\]](https://arxiv.org/abs/1406.3206).
- 1353 [8] **ALICE** Collaboration, J. Adam *et al.*, “ D -meson production in p–Pb collisions at
1354 $\sqrt{s_{\text{NN}}}= 5.02 \text{ TeV}$ and in pp collisions at $\sqrt{s}= 7 \text{ TeV}$,” *Phys. Rev. C* **94** (2016)
1355 054908, [arXiv:1605.07569 \[nucl-ex\]](https://arxiv.org/abs/1605.07569).
- 1356 [9] **ALICE** Collaboration, B. Abelev *et al.*, “Inclusive J/ψ production in pp collisions
1357 at $\sqrt{s}= 2.76 \text{ TeV}$,” *Phys. Lett. B* **718** (2012) 295–306, [arXiv:1203.3641 \[hep-ex\]](https://arxiv.org/abs/1203.3641).
- 1358 [10] **ALICE** Collaboration, J. Adam *et al.*, “Rapidity and transverse-momentum
1359 dependence of the inclusive J/ψ nuclear modification factor in p–Pb collisions at
1360 $\sqrt{s_{\text{NN}}}= 5.02 \text{ TeV}$,” *JHEP* **06** (2015) 55, [arXiv:1503.07179 \[nucl-ex\]](https://arxiv.org/abs/1503.07179).
- 1361 [11] **ALICE** Collaboration, J. Adam *et al.*, “Measurement of pion, kaon and proton
1362 production in proton-proton collisions at $\sqrt{s}= 7 \text{ TeV}$,” *Eur. Phys. J. C* **75** (2015)
1363 226, [arXiv:1504.00024 \[nucl-ex\]](https://arxiv.org/abs/1504.00024).
- 1364 [12] F. Halzen and A. Martin.
- 1365 [13] S. Wheaton, J. Cleymans, and M. Hauer, “THERMUS: A Thermal model package
1366 for ROOT,” *Comput. Phys. Commun.* **180** (2009) 84–106, [hep-ph/0407174](https://arxiv.org/abs/hep-ph/0407174).

- 1367 [14] J. Cleymans, S. Kabana, I. Kraus, H. Oeschler, K. Redlich, and N. Sharma,
1368 “Antimatter production in proton-proton and heavy-ion collisions at ultrarelativistic
1369 energies,” *Phys. Rev.* **C84** (2011) 054916, [arXiv:1105.3719 \[hep-ph\]](https://arxiv.org/abs/1105.3719).
- 1370 [15] S. O. T. P. K. W. H.J. Drescher, M. Hladik.
- 1371 [16] T. P. M. B. K. M. K. Werner, Iu. Karpenko.
- 1372 [17] I. K. T. P. K. Werner, B. Guiot.
- 1373 [18] K. Werner.
- 1374 [19] S. B. et al.
- 1375 [20] M. B. et al.
- 1376 [21] M. Gell-Mann and Y. Ne’eman.
- 1377 [22] J. Rafelski and B. Mller.
- 1378 [23] **ALICE** Collaboration, B. Abelev *et al.*, “Multi-strange baryon production at
1379 mid-rapidity in Pb-Pb collisions at $\sqrt{s_{\text{NN}}}= 2.76$ TeV,” *Phys. Lett.* **B728** (2014)
1380 216–227, [arXiv:1307.5543 \[nucl-ex\]](https://arxiv.org/abs/1307.5543).
- 1381 [24] L. Evans and P. Bryant.
- 1382 [25]
- 1383 [26]
- 1384 [27]
- 1385 [28]
- 1386 [29]
- 1387 [30]
- 1388 [31] **ALICE** Collaboration, K. Aamodt *et al.*, “The ALICE experiment at the CERN
1389 LHC,” *JINST* **3** (2008) S08002.
- 1390 [32] **ALICE** Collaboration, L. B. et al, “Definition of the ALICE coordinate system and
1391 basic rules for sub-detector components numbering,” *In Internal Note*
1392 *ALICE-INT-2003-038* .
- 1393 [33] **ALICE** Collaboration, J. e. a. Alme, “The ALICE TPC, a large 3-dimensional
1394 tracking device with fast readout for ultra-high multiplicity events,” *In Nuclear
1395 Instruments and Method in Physics Research* **A622** (2010) 316–367.

- 1396 [34]
- 1397 [35] R. Glauber.
- 1398 [36] A. S. K.C. Chung, C.S. Whang and G. Pech.
- 1399 [37] **ALICE** Collaboration, J. Adam *et al.*, “Centrality dependence of particle
1400 production in p–Pb collisions at $\sqrt{s_{\text{NN}}}= 5.02$ TeV,” *Phys. Rev.* **C91** (2015) 064905,
1401 [arXiv:1412.6828](https://arxiv.org/abs/1412.6828) [nucl-ex].
- 1402 [38] **ALICE** Collaboration, B. Abelev *et al.*, “Centrality determination of Pb–Pb
1403 collisions at $\sqrt{s_{\text{NN}}}= 2.76$ TeV with ALICE,” *Phys. Rev.* **C88** (2013) ,
1404 [arXiv:1303.0737](https://arxiv.org/abs/1303.0737) [nucl-ex].
- 1405 [39]
- 1406 [40]
- 1407 [41] e. a. Bagnasco. S.
- 1408 [42] R. Brun and F. Rademakers.
- 1409 [43] **ALICE** Collaboration, B. Abelev *et al.*, “Performance of the ALICE Experiment at
1410 the CERN LHC,” *Int. J. Mod. Phys.* **A29** (2014) 1430044, [arXiv:1402.4476](https://arxiv.org/abs/1402.4476)
1411 [nucl-ex].
- 1412 [44] **ALICE** Collaboration, B. Abelev *et al.*, “Pseudorapidity Density of Charged
1413 Particles in p–Pb Collisions at $\sqrt{s_{\text{NN}}}= 5.02$ TeV,” *Phys. Rev. Lett.* **110** (2013)
1414 032301, [arXiv:1210.3615](https://arxiv.org/abs/1210.3615) [nucl-ex].
- 1415 [45] **ALICE** Collaboration, K. Aamodt *et al.*, “Strange particle production in
1416 proton-proton collisions at $\sqrt{s}= 0.9$ TeV with ALICE at the LHC,” *Eur. Phys. J.*
1417 **C71** (2011) 1594, [arXiv:1012.3257](https://arxiv.org/abs/1012.3257) [nucl-ex].
- 1418 [46] S. Roesler, R. Engel, , and J. Ranft, “The Monte Carlo Event Generator
1419 DPMJET-III, Advanced Monte Carlo for Radiation Physics, Particle Transport
1420 Simulation and Applications,” *Conference Proceedings, MC2000, Lisbon, Portugal,
1421 October 23-26* (2000) 1033–1038, [hep-ph/0012252](https://arxiv.org/abs/hep-ph/0012252).
- 1422 [47] R. Brun, F. Carminati, and S. Giani, “GEANT detector description and simulation
1423 tool,” *CERN-W5013* (1994) .
- 1424 [48] R. Barlow, “Systematic Errors: Facts and Fictions,” *Presented at Advanced
1425 Statistical Techniques in HEP, Durham, March 2002* (2002) 333p,
1426 [hep-ex/0207026v1](https://arxiv.org/abs/hep-ex/0207026v1).

- 1427 [49] **ALICE** Collaboration, B. Abelev *et al.*, “Centrality dependence of π , K and p
1428 production in Pb–Pb collisions at $\sqrt{s_{\text{NN}}}= 2.76$ TeV,” *Phys. Rev.* **C88** (2013) ,
1429 [arXiv:1301.4361](https://arxiv.org/abs/1301.4361) [nucl-ex].
- 1430 [50] **STAR** Collaboration, B. I. Abelev *et al.*, “Hadronic resonance production in d–Au
1431 collisions at $\sqrt{s_{\text{NN}}}= 200$ GeV measured at the BNL Relativistic Heavy-Ion Collider,”
1432 *Phys. Rev.* **C78** (2008) 044906, [arXiv:0801.0450](https://arxiv.org/abs/0801.0450) [nucl-ex].
- 1433 [51] A. Velásquez, “Mean p_{T} scaling with m/n_q at the LHC: Absence of (hydro) flow in
1434 small systems?,” *Nucl. Phys.* **A943** (2015) 9–17, [arXiv:1506.00584](https://arxiv.org/abs/1506.00584) [hep-ph].
- 1435 [52] **ALICE** Collaboration, B. Abelev *et al.*, “Multi-strange baryon production in pp
1436 collisions at $\sqrt{s}= 7$ TeV with ALICE,” *Phys. Lett.* **B712** (2012) 309,
1437 [arXiv:1204.0282](https://arxiv.org/abs/1204.0282) [nucl-ex].
- 1438 [53] T. Sjöstrand, S. Mrenna, and P. Skands, “A brief introduction to PYTHIA 8.1,”
1439 *Comput. Phys. Comm.* **178** (2008) 852–867, [arXiv:0710.3820](https://arxiv.org/abs/0710.3820) [hep-ph].

1440 **Acknowledgements**